

Study of Microscopic Structure via NMR Diffusive Scattering

by

Yuan Cheng

M.S. in Applied Physics, Tsinghua University, April, 1991
B.S. in Applied Physics, Tsinghua University, July 1988

Submitted to the Department of Nuclear Engineering
in partial fulfillment of the requirements for the degree of

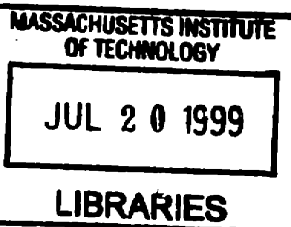
Doctor of Philosophy in Radiological Science

at the

MASSACHUSETTS INSTITUTE OF TECHNOLOGY

September 1998

ARCHIVES



© Massachusetts Institute of Technology 1998. All rights reserved.

Author
.....

Department of Nuclear Engineering
August 20, 1998

Certified by
.....

David G. Cory
Associate Professor
Thesis Supervisor

Read by
.....

Sow-Hsin Chen
Professor
Thesis Reader

Accepted by
.....

Lawrence Lidsky
Chairman, Department Committee on Graduate Students

Study of Microscopic Structure via NMR Diffusive Scattering

by

Yuan Cheng

M.S. in Applied Physics, Tsinghua University, April,1991

B.S. in Applied Physics, Tsinghua University, July 1988

**Submitted to the Department of Nuclear Engineering
on August 20, 1998, in partial fulfillment of the
requirements for the degree of
Doctor of Philosophy in Radiological Science**

Abstract

Scattering experiments can be carried out by gradient nuclear magnetic resonance(NMR) methods. Magnetic field gradient pulses are utilized to create linear phase ramps of the spin magnetization across the sample along arbitrary directions. The linear phase ramps are defined as dynamic spin magnetization gratings. The measurement of the grating after it undergoes dynamic processes characterized by the local structure leads to the measurement of the average phase changes over the whole sample, $\langle e^{-i\mathbf{q} \cdot \mathbf{r}(0)} \cdot e^{i\mathbf{q} \cdot \mathbf{r}(t)} \rangle$, a quantity denoted as intermediate scattering function. NMR scattering are measured in spatial and temporal window to sub-microns to tens of micros and milliseconds to a few seconds.

In a time scale when spin displacements are larger than the spatial scale of local structure, NMR experiments directly measure the elastic incoherent structure function(EISF), $\langle |S(\mathbf{q})|^2 \rangle_{powder}$.

The direct control of scattering vector \mathbf{q} in NMR scattering enables easy performance of multiple scattering experiments. The double scattering experiments, as examples of multiple scattering, lead to the measurement of structure factors $\langle |S(\mathbf{q})|^4 \rangle_{powder}$ and $\langle |S(\mathbf{q})|^2 |S(\mathbf{q}_\perp)|^2 \rangle_{powder}$. The latter correlates local structural characteristics along directions that are normal to each other. Anisotropic information in a glassy sample can be determined without the presumptive models which are required in one dimensional or traditional scattering techniques.

This thesis work includes detailed derivation of the theory of NMR double scattering, an experiment that can only be performed by NMR. The eccentricity information can be extracted by the differences of scattering curves from double scattering along one axis and along two orthogonal axes. The experiments are carried out for abnormally long yeast cells.

The experimental results show good agreement with calculations where the yeast

cell shape was approximated as prolate ellipsoids.

Thesis Supervisor: David G. Cory

Title: Associate Professor

Acknowledgments

First and foremost, I would like to express my sincere gratitude to my thesis advisor David G. Cory, who took me on as one of his first students upon my arrival at MIT. David has provided every encouragement and support all these years, not only has a big influence on my understanding of the physics of NMR, but also convinced me from early on that NMR is simple and fun. His broad knowledge of NMR, his sharp intuition, his uncommon common sense, his trenchant observations, together with his sense of decency and humility and his gentle concern of people around him showed him a fearless leader and a true friend.

In addition to David, I would like to thank Sow-Hsin Chen and Sidney Yip for the most supportive and pleasant discussions on my thesis work.

And Werner E. Maas, during the past years, kindly and generously took his time to share his idea with me. I remember his quick mind, optimism and gentle demeanor.

I am indebt to Cory Kostrub from the Genetics Laboratory at Harvard Medical School for his generosity in preparing and providing the yeast samples.

My sincere thanks go to Ching-Hua Tseng, for valuable discussions from the basics of the scattering experiments to Monte-Carlo schemes to suggesting the best sample for the double scattering experiments.

I fondly look back at my early days at MIT when Guowang Zhang, Yang Zhang, Sungmin Choi, Wurong Zhang, Chris Drew and I struggled together in the classroom on the second floor of building NW14 trying to understand the physics of NMR. I really enjoyed working with them, from moving the equipments around in the lab to debugging computer programs.

I have enjoyed the company of “Cory’s Troop” (quote from Irene, a former secretary). I remember many pleasant times at Cambridge Brewing Company. During the past two years I had a good fortunate to overlap with Mark Price, Dan Caputo, Paul Owen, Marco Pravia and, of course, Greg Boutis who is always happy to discuss “top secrets” and willing to try new linguistic adventures, I enjoyed pleasant interaction with them very much.

Special thanks go to my present and erstwhile officemates, Aaron Sodickson, Xiaowu Tang and Gabriela Leu for creating congenial atmosphere to discuss NMR and many other things. Especially, Xiaowu, who has been providing the most helpful hands to me in the lab.

To my beloved family back in China, my mother, father, sister Mai, niece Xiayu (Maomao). Words are not adequate to express my gratitude to them. I really miss them.

Lastly, to my wife Yan and our daughter Huihui. I wish it were possible to give a commensurate amount of thanks to Yan for all her love, support, patience, and the motivation to finish.

Dedications

A musician must make his music,
an artist must paint,
a poet must write
if he is to ultimately be
at peace with
himself.

-Abraham Maslow

To my wife, Yan Shao.

To my daughter, Rebecca Hui.

Contents

1	Introduction	17
1.1	Motivation	17
1.2	NMR Basics	20
1.2.1	Spin Ensembles	20
1.2.2	RF Pulses, FID, T_1 and T_2 , Bloch Equations	21
1.2.3	Spin magnetization grating	22
1.2.4	Spin Echo and the Stimulated Echo	29
1.3	Flow and Molecular Diffusion	31
1.3.1	The Measurement of Flow Rate	31
1.3.2	Isotropic free diffusion	32
1.3.3	Anisotropic diffusion	35
1.4	Summary	38
2	NMR Scattering	40
2.1	The Effects of Radio Frequency Pulses on a Magnetization Grating	41
2.2	Pulsed Gradient Spin Echo Experiments	42
2.3	Pulsed Gradient Stimulated Echo Experiment	45
2.4	Correlation Equations for 1-D PGSE/PGSTE Experiments	46
2.5	The Patterson Function	49
2.5.1	Definition of the Patterson Function	49
2.5.2	Correlation Functions of Simple Geometries	50
2.5.3	Obtaining Other Information from Patterson Function	52
2.6	The \mathbf{k} and \mathbf{q} Gratings and Spaces	54

2.6.1	The \mathbf{k} Gratings and Space	54
2.6.2	The \mathbf{q} Gratings	55
2.6.3	Mapping of k and q Space	58
2.7	Summary	60
3	Multiple Scattering Experiments	61
3.1	Introduction	61
3.2	Simple Double Scattering Experiments	63
3.3	Double Scattering on Homogeneous Free Diffusion	65
3.4	Double scattering on a bounded compartment	67
3.5	Interpretation of the Double Scattering Experiments	67
3.5.1	2-D Correlation Functions	67
3.5.2	Structure Factor $ S(\mathbf{q}) ^2$ and Power Expansion	71
3.6	Summary	73
4	Calculation and Simulation	74
4.1	Calculate by Convolution in Real Space	75
4.2	Simulation by Monte-Carlo in Q Space	79
4.3	Analytical Calculation in Q Space	80
4.4	Discussion	84
5	Experiments	86
5.1	Instrumentation	86
5.2	Sample Preparation	86
5.3	Results and Discussion	90
6	Diffusion in NMR Microscopy	95
6.1	Background	96
6.2	Molecular diffusion in a sample of finite extent	97
6.3	Calculations	97
6.4	Experiments and Discussion	99

A Choosing Only the Desired Signal for 2-D Scattering Experiments	103
A.1 Filtering of Single Scattering Events	103
A.2 Selection of k Pathways	105
B Computer Program Codes	119
B.1 C++ Code for Monte-Carlo Simulation for 2-D Scattering	119
B.2 MATLAB Code for Convolution Calculation for 2-D Scattering	125
B.3 Matlab Code for Calculation Analytically	126
B.3.1 2-D Scattering with Parallel Scattering Vectors	126
B.3.2 2-D Scattering with Perpendicular Scattering Vectors	127
Bibliography	128

List of Figures

1-1	The creation of a magnetization grating. A gradient pulse of amplitude G and duration δ is turned on after the $\frac{\pi}{2}$ pulse. The wave number of the created grating is $k = \gamma G \delta$	23
1-2	A transverse magnetization(M_x) grating along z-axis. The length of the period is determined by $\frac{2\pi}{k}$, where $k = \gamma g_z \delta$	24
1-3	Magnetization grating is created to shift the whole reciprocal space in order to measure certain components as NMR can only measure the zero component. In imaging the spin density in reciprocal space is shifted by the addition of a magnetization grating permitting a complete set of measurements at $k = 0$ to map out the images.	25
1-4	The evolution of spin magnetization grating under dynamics determined by certain structures.	26
1-5	Scattering from two parallel planes as an analogy to flow measurement in NMR. Shown flow measurement is a coherent scattering experiment.	28
1-6	Pulse sequence and signal of a spin echo experiment. The echo intensity decays as $e^{-2\tau/T_2}$	29
1-7	Pulse sequence and signal of a stimulated experiment. The intensity of the stimulated echo at $(2\tau + \Delta)$ decays as $e^{-2\tau/T_2} e^{-\Delta/T_1}$	30
1-8	$q^2 \Delta$ dependence of echo attenuation curves in 1-D, 2-D and 3-D diffusion calculated by Equations(1.44).	37
2-1	A π RF pulse does not change the wave number of the magnetization grating. However, it inverts the grating's direction.	43

2-2	Pulse sequence of a PGSE experiment. The first RF pulse tips the spin magnetization from its equilibrium position z to the transverse plane. The first gradient pulse will superimpose a magnetization grating into the sample. The wave number is determined by $k = \gamma G \delta$. The π RF pulse inverts the magnetization grating that has evolved during Δ . The second gradient pulse is identical to the first one. It refocuses the component with the same wave number k and the coherent of phases is re-established and measured at 2τ when an spin echo is observed.	44
2-3	Diffusion experiment using the stimulated echo and pulsed field gradients. The range of dynamic that can be measured is extended to longer times. The time window of a stimulated echo is on the order of seconds.	45
2-4	Simple spin density function, their auto-correlation and scattering curves, i.e. Fourier transforms of the correlation functions. Left: 1-D top-hat pore; Right: 2-D cylindrical pore. From top to bottom: spin density functions, correlation functions and scattering curves.	51
2-5	A pore and its “ghost”, displaced from it by x . Their convolution is the common shaded area.	52
2-6	A PGSE experiment on a sample with ensemble of bounded pores at different positions. (a) After the first gradient pulse, a k grating is created across the whole sample. (b) The grating inside each pore is smeared out due to long time molecular diffusion. However, the averaged phases of the pores still show features of the k grating. (c) After the second gradient pulse, the leftover k grating is totally refocused. Within each pore, there is a q grating with the wave number the same as the original k grating. The q gratings are identical in phase within the pores.	56
2-7	PGSE-MASSEY pulse sequence with q -gradient pulses and k gradient pulses. The read gradient enables the restoration of spatially dependent phase twist, i.e., the residual k -grating.	58

2-8	Expected space of k and q of NMR experiment. NMR imaging measures the line of $q = 0$, while a PGSE experiment measures the line of $k = 0$	59
2-9	Above: A scattering experiment that only measures $E(k, q)$ at $k = 0$; Below: An imaging experiment that only measures $E(k, q)$ at $q = 0$	59
3-1	A simple gradient pulse combination of an NMR multiple scattering experiment. The gradient pulses are G in amplitude and δ in duration. The wave vectors associated with the gradient pulses are $\mathbf{q}_1 = \gamma G \delta \hat{x}$, $\mathbf{q}_2 \gamma G \delta \hat{y}$ and $\mathbf{q}_3 = -\gamma G \delta \hat{x} - \gamma G \delta \hat{y}$, respectively. The total vectorial sum of the three are 0.	62
3-2	NMR multiple scattering experiments are essentially experiments of multiple stimulated echoes. There can be undesired paths that satisfy the condition for multiple scattering experiments, $\sum_i \mathbf{q}_i = 0$ or the ending point of the path is at 0. There are also single scattering events in the mix when the signal comes from the magnetization excited not by the very first but the later RF pulses. The signals from these magnetizations only go thought part of the desired pathway.	63
3-3	A simple double diffusive scattering pulse sequence with the angle between scattering vectors set to 0° . For complete bounded diffusion with long time limit, the measured signal as a function of the amplitude of wave vector q is the average product of the power of a center ray and itself in the three dimensional q space reciprocal to the spin density function of the bounded region—the pore.	64
3-4	Double diffusive scattering pulse sequence with the angle between scattering vectors set to 90° . For complete bounded diffusion with long time limit, the measured signal as a function of the amplitude of wave vector q is the average product of the power of a center ray and a perpendicular ray in the three dimensional q space reciprocal to the spin density function of the bounded region—the pore.	65

3-5	The comparison between (a)correlation of profiles along two orthogonal directions within a single pore and (b)no correlations for two individual 1-D experiments along two orthogonal directions on a system of randomly oriented pores which yields the same displacement profile.	68
3-6	A 2-D diffusive scattering performed on an arbitrarily oriented pore. for a system of randomly oriented pores, the result is the sum of the correlations.	69
3-7	Plots of simulated 2-D correlation profiles verses convolutions of 1-D profiles on samples with randomly oriented prolate pores with compress ratio 1/5 and 1/10. The full width of the 2-D determines the average correlated microscopic length scales along two perpendicular directions. The full width of the convolution of 1-D profiles obtained separately determines the largest length scales of the randomly oriented pores. The full width can only be obtained at very low signal intensities. . .	70
4-1	Ellipse with long axis $\overline{OA} = \overline{OB} = b$ and short axis $\overline{OC} = \overline{OD} = a$, focus F_1 and F_2 , the eccentricity $e = \sqrt{1 - \frac{a^2}{b^2}}$	76
4-2	Figure shows ellipsoids with varies eccentricities. From prolate, upper-left, to oblate, lower right.	77
4-3	Simulation curves for different eccentricities obtained by correlation/convolution method. The volume of the ellipsoids are the same $V = 8\mu m^3$. The solid lines are results of $2D_{xy}$ and the dashed lines are results of $2D_{xx}$. The full widths are very difficult to see in the plots.	78
4-4	Figure shows phase differences of a spin due to displacement between four points, measured by double scattering experiments with parallel or perpendicular scattering vectors.	79
4-5	The geometric drawing on how to obtain a vector q_y perpendicular to vector q_x . Due to symmetry, only the angle θ_1 , which is the angle between q_y and z , is needed. The relations can be denoted by equation $\cos \theta_1 = \sin \theta \cos \psi$	81

4-6 Double scattering curves calculated for different eccentricities. Upper curves: $\tilde{E}_{\parallel}(q)$; Lower curves: $\tilde{E}_{\perp}(q)$	82
5-1 Quiver plot of calculate of the $x = 0$ plane of the magnetic field gradient inside the gradient set. High uniformed gradient can be seen within 2 millimeters from the center.	87
5-2 semi-logarithm verses second power of gradient pulse amplitudes of diffusion measurement on free water. The straight line extended to very high gradient strength indicates high uniformity of gradient field and high linearity of the system.	88
5-3 Transmitted microscopic pictures of regular(left), medium long(middle) and extra long yeast cells. All three pictures are taken under same amplification. In the lower-left corner, the two tick marks are image of a standard microscopic scale taken under the same condition. The distance between the two ticks is $0.01mm$. From the picture, the average diameter of the normal yeast cells is around $4\mu m$, the average short semi-major diameters of the two groups of long yeast cells are $4\mu m$, the average long diameters are $15\mu m$ and over $20\mu m$.	89
5-4 One dimensional scattering curves of regular round yeast cells. Both curves taken by pulsed gradient stimulated echo. The maximum gradient strength is 1271 Gauss/cm. Gradient pulse time is 1.5 ms. For open circles, mixing time $\Delta = 27ms$, for squares, mixing time $\Delta = 17ms$. The strong oscillation feature of the curves indicates that the cells are round and with narrow size distribution.	90
5-5 2-D scattering curves from medium long yeast cells. The open circles and squares correspond to scattering of parallel and perpendicular scattering vectors. The solid lines are fitted curves by power expansion up to 6th power. For both data sets: maximum gradient strength is 600 Gauss/cm, gradient pulse length is 1.0 ms. Mixing times are 27 ms. The time interval between two scattering events is 40 ms.	92

5-6 2-D scattering curves from extra long yeast cells. The open circles and squares correspond to scattering of parallel and perpendicular scattering vectors. The solid lines are fitted curves by power expansion up to 6th power. For both data sets: maximum gradient strength is 600 Gauss/cm, gradient pulse length is 1.0 ms. Mixing times are 27 ms. The time interval between two scattering events is 40 ms.	93
6-1 Comparison of two simulation methods. Dashed lines represent free diffusion approach using Bloch-Torry equations. Solid lines represent calculation using conditional probability density function. (a) $\delta = 1ms$, (b) $\delta = 5ms$, (c) $\delta = 20ms$, (d) $\delta = 100ms$, (e) $\delta = 500ms$, (f) $\delta = 2000ms$	99
6-2 A gradient echo of a sample of a top-hat cell calculated using free diffusion approximation (top) and conditional probability density function. $\delta = 0.02ms$	100
6-3 The 1-D images of double top-hat cells calculated assuming free diffusion (dashed lines) and using conditional probability density function. Upper left: $\delta = 0.1ms$; Upper right: $\delta = 1ms$; Lower left: $\delta = 4ms$; Lower right: $\delta = 108ms$;	101
6-4 Amplitude of CTI signal of a 100 micron I.D. capillary tube. The amplitudes of the open circles ($tp=4ms$) didn't fall below the squares ($tm=0.5ms$), even at the fourth and the fifth lobes, indicating no significant diffusion loss.	102
A-1 Because a $\frac{\pi}{2}$ RF pulse will cause the mixing of $+k$ and $-k$ paths, there are additional pathways that can contribute to the final stimulated echo. 105	
A-2 The middle non-zero k path can be killed by setting the two pairs of the gradient pulses opposite to each other. The unwanted path is erased by the mismatch of the first and the second pair of gradient pulses due to background gradient.	118

List of Tables

2.1 Table shows effects of different RF pulses on spin magnetization grating within transverse plane and along \hat{z} axes.	42
A.1 Phase Cycle for 2-D Scattering. All signals from single scattering events are filtered out. For $2D_{xx}$ and $2D_{yy}$ experiments, three k pathway is allowed. CYCLOP can be implemented on top of this phase cycling.	104
A.2 Improved phase Cycle for 2-D Scattering. For all experiments, $2D_{xy}$, $2D_{xz}$ and $2D_{yy}$, only one k pathway is selected. CYCLOP can be implemented on top of this phase cycling.	106

Chapter 1

Introduction

1.1 Motivation

A wide range of spatial information is measurable by nuclear magnetic resonance(NMR)[1, 2], extending from dipolar resolved distance measurements between distinct spins at angstrom scale to large scale imaging (up to 100 m size samples of permafrost domes). For the well known imaging measurements and scattering measurements to be discussed here, the spatial scale is determined by a grating of spin magnetization that is imposed on the sample through differential spin precession rates in a magnetic field gradient.

In both imaging and scattering cases the spin magnetization grating is wound up by the differential precession rates over a time and thus the phase of the transverse spin magnetization picks up a linear spatial dependence and is best described as a linear phase ramp across the sample. The slope of the ramp is proportional to the gradient strength multiplied by the evolution time, and is normally described in terms of a wave-number, k . The vectors of the spin magnetization describe a spatial helix with a periodicity represented by the wave-number k .

In magnetic resonance imaging(MRI) this spatially periodic phase modulation of the spin magnetization permits the direct measurement of a specific Fourier component of the sample's spin density. Therefore, a Fourier transform of the measured signal will generate a spatial mapping of the spin density.

In NMR scattering, the measurement is of the average changes of this spatially periodic phase modulation under the influence of various molecular dynamic processes such as flow and diffusion. Here, the wave-number is linked to local displacement other than absolute position. The Fourier transform of the measured signal is the displacement profile of the spin system.

The measurement of the NMR signal under the influences of the molecular displacement provides a powerful tool to study the dynamics and the structures of barrier to diffusion. Some of the key development took place in the early stage of NMR, Hahn's discovery of the spin echo[3], extensions by Carr and Purcell[4] to a trains of echoes and the use of these to quantify the diffusion constant formalized by Torrey[5]. In the mid 60's, Stejskal and Tanner published a series of papers [6, 7, 8] introducing pulsed field gradient methods which could separate the influences of T_2 relaxation and molecular diffusion. The pulsed gradient spin echo(PGSE) and pulsed gradient stimulated echo(PGSTE) are a powerful tool to probe the dynamics and structure of molecular displacements in free and restricted environments. From an NMR point of view, PGSE or PGSTE experiments measure the signal changes caused by molecular motion, as a function of gradient amplitude and/or flow/diffusion time.

Although there have been attempts in the past to extend the gradient NMR to diffraction of scattering experiments [9, 10] and to draw analogies between NMR and X-ray diffraction, the most commonly used techniques in modern crystallography, NMR hasn't been regarded as a legitimate technique to perform scattering experiments until the late 80's. Cory and Garroway introduced an optical analogy that the echo signal amplitude of a PGSE experiment as a function of applied gradient is directly proportional to the power diffraction pattern of a single slit whose transmission is described by its shape function [11]. By this method, the echo amplitude is directly linked to the average molecular translational displacement probability. Obviously the asymptotic approximation of this probability is simply the shape function of the restrictive geometry. Fatkullin [12] and Callaghan [13] also separately made an explicit comparison of pulsed field gradient spin echo experiments to intermediate neutron scattering function. Although the method sometimes is referred to

as “q-space imaging” [14], it has essential distinctions from an imaging experiment. Imaging experiments measures the signal intensity and phase while PGSE experiment, like scattering, only measures the intensity; therefore, they provide different aspects of the system. First, an imaging experiment gives spin density as a function of absolute spatial locations while a PGSE experiment measures average correlations of local structures as a function induced by relative displacements. In other words, imaging is static and PGSE is dynamic. Secondly, an image is a direct mapping of the spin density, an echo amplitude function measured by PGSE is the power spectrum of the *local* shape function. Since the phase is irrevocably lost, there is no means by which the original spin density can be reconstructed. However, the echo signal collected in a PGSE experiment comes from all the restrictive compartments; therefore, the sensitivity of this “q-space imaging” is greatly enhanced over “k-space imaging”.

The PGSE experiment measures the intermediate scattering function, $|S(\mathbf{q})|^2$. This discovery leads to the use of scattering formulisms to explain some NMR results [15]. Although the inverse problem can not be solved in general, there are solutions when specific models are assumed based on prior knowledge of the system.

One of the examples is the separation of the size distribution from the shape orientation. One important example is the determination of the eccentricities of pores inside a glassy sample. For extreme eccentricities such as surface or linear cases, experimental data can be fit to pre-calculated curves since for different restricting characteristics, the echo amplitude shows different curvatures. Callaghan used this method to successfully measure 1-D and 2-D samples in grains[16, 17]. In general, the 2-D information can also be obtained by the so called “size distribution function” which is the second derivative of the Patterson function by implementation of the model which assumes that the apparent size differences are due to orientation variations. The above methods are all based on single scattering events which corresponds to one dimensional experiments. Any 2-D information are extracted based on some degree of knowledge of the system and applying models. In a porous glass sample of randomly oriented ellipsoids, the local anisotropy can not be measured by varying the bulk orientation of the scattering vector.

A unique feature of NMR scattering is the easy control over the scattering vector \mathbf{q} . This thesis work shows how to take advantage of this to solve problems that conventional scattering methods can not. NMR multiple diffusive scattering methods are developed and tested. The methods measure correlations of compartment shape functions along two orthogonal directions of each individual compartment, averaged over all the possible orientations. By measuring and comparing two double scattering curves $\langle |S(\mathbf{q})|^2 |S(\mathbf{q})|^2 \rangle_{powder}$ and $\langle |S(\mathbf{q}\mathbf{q})|^2 |S(\mathbf{q}_\perp)|^2 \rangle_{powder}$, the average pore size and eccentricity can be obtained without the requirement of the proper alignment of the pores and/or presumption models of the sample system.

1.2 NMR Basics

The NMR scattering methods described in this thesis are classical phenomena, and are therefore easily understood with a simple picture of spin dynamics. Below are outline of the necessary basics is provided. The general references on principles of NMR are books by Abragam[18] and Slichter [19].

1.2.1 Spin Ensembles

Many nuclear isotopes have non-zero spin angular momentum $I\hbar$, where \hbar is the Plank's constant. According to the basic theory of quantum mechanics of angular momentum, I can take on only the values of $\frac{1}{2}, 1, \frac{3}{2}, 2, \frac{5}{2}$, etc. Associated with this quantum number I is the magnetic dipole moment μ ,

$$\mu = \gamma \hbar \mathbf{I}, \quad (1.1)$$

where γ is the gyro-magnetic ratio which is a property of the nucleus. In an external magnetic field $\mathbf{B} = B_0 \hat{z}$, the magnetic moment can take one of the $2I + 1$ allowed orientations, or in a quantum mechanical term, eigenstates. The Hamiltonian of the

spin system is,

$$\hat{H} = -\mu \cdot \mathbf{B} \quad (1.2)$$

$$= -\gamma \hbar B_0 I_z \quad (1.3)$$

In an ensemble of nuclear spins I , the $2I + 1$ allowed energy levels are populated in thermal equilibrium in accordance with the Boltzmann distribution. For $I = \frac{1}{2}$, the ratio of the number of spins per unit volume in the higher energy state to that in the lower state is given by,

$$\frac{N_{up}}{N_{down}} = \exp\left(-\frac{\gamma \hbar B_0}{k_B T}\right), \quad (1.4)$$

where T is the Kelvin temperature of the lattice, and k_B is the Boltzmann constant. After the external magnetic field is “switched on”, the spin system requires time to attain the state of thermal equilibrium by a first-order process known as spin-lattice or longitudinal relaxation by a single time constant T_1 , a characterized measure of energy exchange rate between the spins and the lattice,

$$M_z(t) = M_0(1 - e^{-t/T_1}), \quad (1.5)$$

where M_z is the longitudinal magnetization, and,

$$M_0 = \frac{N \gamma^2 \hbar^2 B_0}{4k_B T}, \quad (1.6)$$

is the magnetization at equilibrium. N is the number of spins per unit volume. At equilibrium, the spin magnetization is aligned along the external applied magnetic field.

1.2.2 RF Pulses, FID, T_1 and T_2 , Bloch Equations

A radio frequency(RF) magnetic field transmitted through an RF coil lying in a plane transverse to the external magnetic field \mathbf{B} causes rotation of magnetization

about this RF field. The amplitude and length of the RF pulse determines the tip angle of the magnetization. An on resonance $\frac{\pi}{2}$ pulse along the x axis will tip the z magnetization down to the transverse plane in the y direction. An on resonance π pulse will inverse the magnetization. The transverse RF field has no effect on the magnetization components along the RF axis.

The Free induction decay(FID) is a decayed sinusoid signal, which is caused by the precessing transverse spin magnetization, picked up by the RF coil following an RF pulse. During a free induction decay, no RF field is present.

The longitudinal or T_1 relaxation is the process by which the spin system exchanges energy with the surrounding environment and back to the thermal equilibrium. The transverse or T_2 relaxation is a measure of the phase coherence lifetime. The two relaxations can each be expressed by a single time constant, T_1 and T_2 .

The Bloch equations[20] provide a very simple way of formulating the two different relaxation phenomena,

$$\frac{dM_z}{dt} = \frac{M_0 - M_z}{T_1} + \gamma(\mathbf{M} \times \mathbf{B})_z \quad (1.7)$$

$$\frac{dM_x}{dt} = -\frac{M_x}{T_2} + \gamma(\mathbf{M} \times \mathbf{B})_x \quad (1.8)$$

$$\frac{dM_y}{dt} = -\frac{M_y}{T_2} + \gamma(\mathbf{M} \times \mathbf{B})_y. \quad (1.9)$$

1.2.3 Spin magnetization grating

Spatial information is available in NMR on a wide range of length scales. The most direct measurement is a Fourier picture that based upon spin magnetization gratings.

The spin magnetization grating is created by applying a magnetic field gradient across the sample. When a transverse magnetization is placed in a uniform external magnetic field $B_0\hat{z}$, it will precess in the transverse plane with a rate proportional to B_0 ,

$$\omega = -\gamma B_0, \quad (1.10)$$

ω is called the Lamor frequency. The effect of a magnetic field gradient, or a linear spatial variant magnetic field is to cause the spin magnetization precess at different angular velocities proportional to position and this will create a linear phase ramp of the spin magnetization. If a magnetic field gradient $\frac{\partial B_z}{\partial z} \hat{z}$ is added to $B_0 \hat{z}$, the Lamor frequency depends on z ,

$$\omega(z) = -\gamma B_0 - \gamma \frac{\partial B_z}{\partial z} z. \quad (1.11)$$

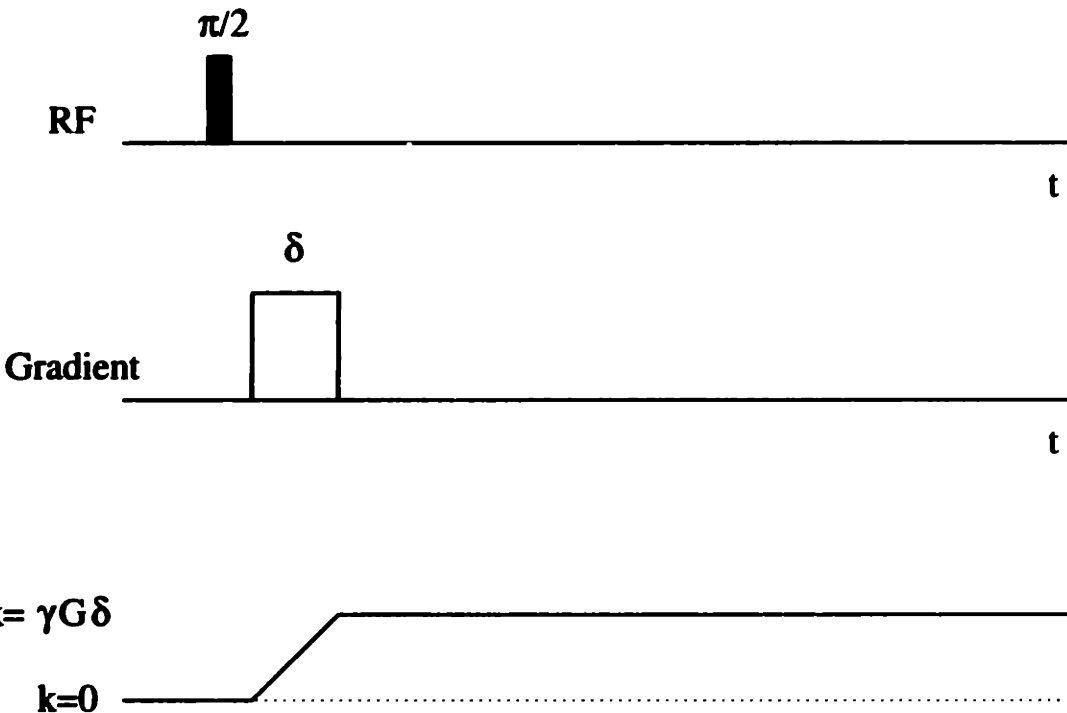


Figure 1-1: The creation of a magnetization grating. A gradient pulse of amplitude G and duration δ is turned on after the $\frac{\pi}{2}$ pulse. The wave number of the created grating is $k = \gamma G \delta$.

If the gradient field is turned on for a time δ , as seen in Figure (1-1) the phase or the directions of the spins in the transverse plane will depend on the positions of the spins and a periodic modulation, along the z axis of the spin magnetization, is created,

$$\text{Grating} = e^{-i \int_0^\delta \gamma \frac{\partial B_z}{\partial z} z dt}. \quad (1.12)$$

The integration of the gradient over time determines the period of the grating. If the gradient is independent of time when it is on, the grating is written as,

$$\text{Grating} = e^{-i\gamma\tau_z \delta z} \quad (1.13)$$

where $g_z = \frac{\partial B_z}{\partial z}$ and a constant phase factor of $e^{-i\gamma B_0 \delta}$ has been thrown away since it has no effect on the dynamic process *vide infra*. The wave number of the grating, from the above equation, is,

$$k_z = \gamma g_z \delta. \quad (1.14)$$

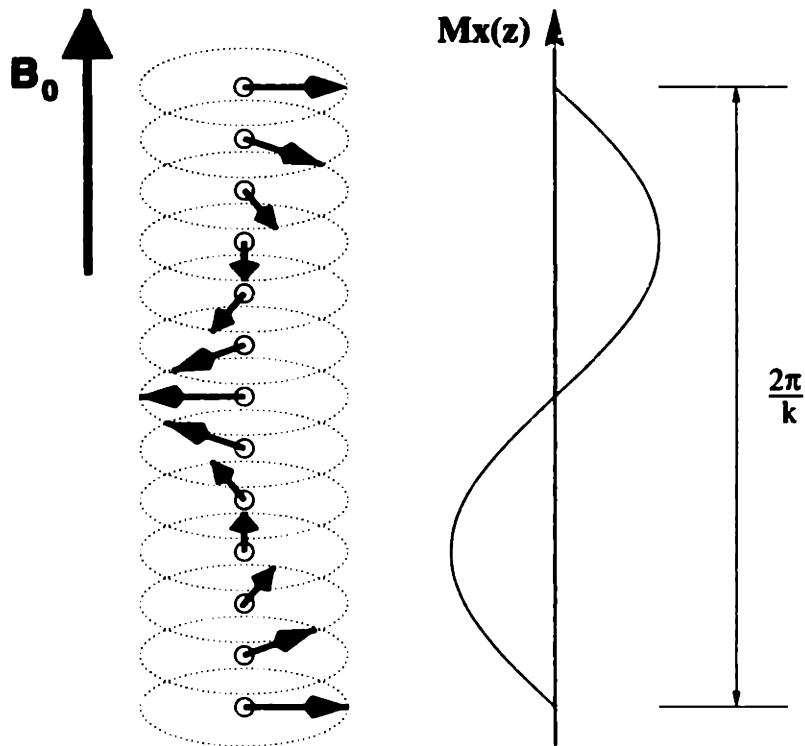


Figure 1-2: A transverse magnetization(M_x) grating along z-axis. The length of the period is determined by $\frac{2\pi}{k}$, where $k = \gamma g_z \delta$.

Figure (1-2) shows a graphical picture of a uniform M_x grating along z-axis. It can be seen that the magnetization comes from the connection between magnetic field gradient and space. One of the application of the grating is Magnetic Resonance Imaging(MRI) in which magnetization gratings are created across the sample with

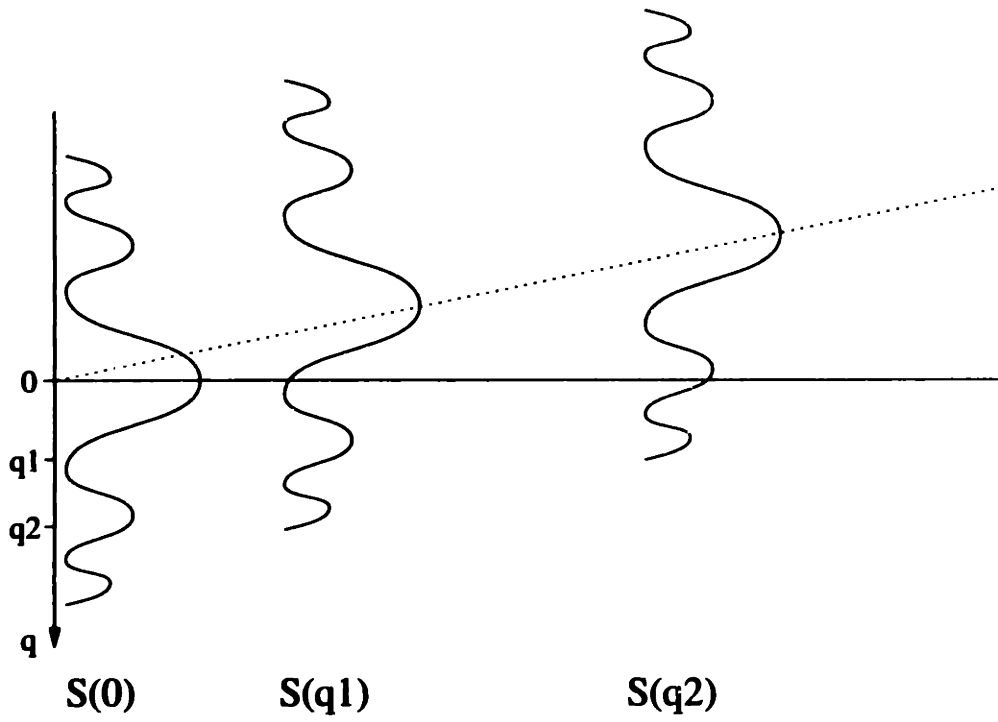


Figure 1-3: Magnetization grating is created to shift the whole reciprocal space in order to measure certain components as NMR can only measure the zero component. In imaging the spin density in reciprocal space is shifted by the addition of a magnetization grating permitting a complete set of measurements at $k = 0$ to map out the images.

spin density $\rho(x)$,

$$\begin{aligned}
 \rho(z, \delta) &= \rho(z, 0)e^{-i\gamma g_z \delta z} \\
 &= \rho(z, 0)e^{-ik_z z} \\
 &= \rho(z) \otimes \delta(k - k_z).
 \end{aligned}$$

The result of this grating across the sample is to shift the whole k -space of the sample so that a particular k component can be measured, as seen in Figure(1-3).

The NMR scattering experiments is based on the evolution of the spin magnetization grating due to molecular dynamics as shown in Figure(1-4). Examples of these are coherent flow, free diffusion and bounded diffusion. The NMR scattering is measured by applying an identical but inverse magnetic field gradient pulse to the

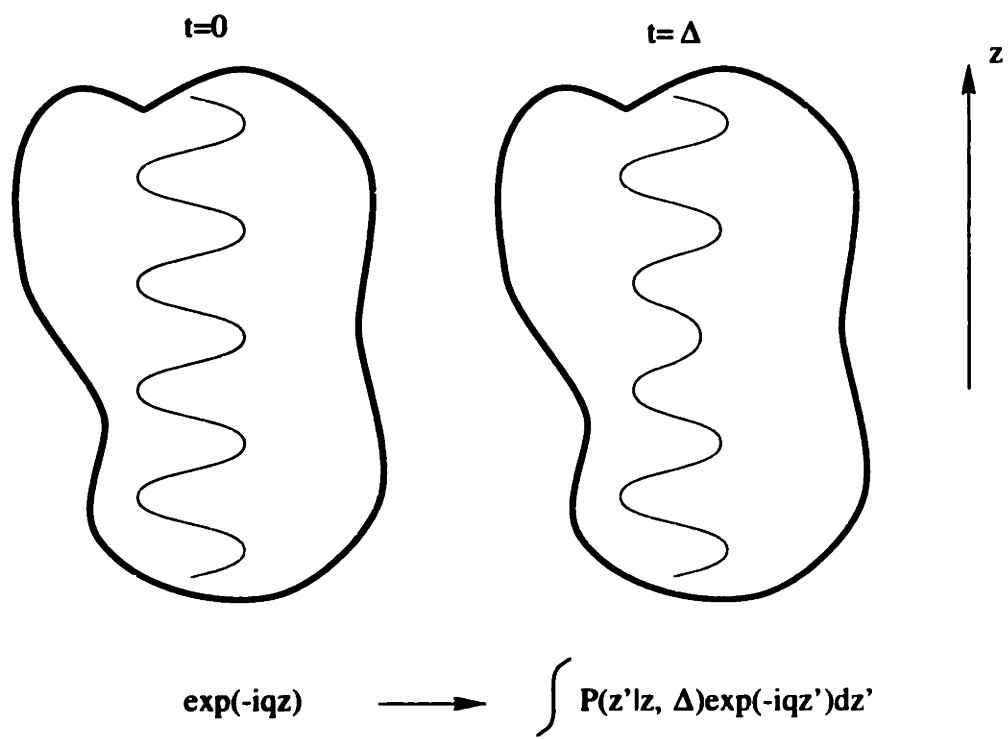


Figure 1-4: The evolution of spin magnetization grating under dynamics determined by certain structures.

magnetization grating so that the spins that do not move are “refocused” (end up in-phase) and those that did move pick up a phase modulation proportional to their offset along the gradient direction. Since this gradient pulse causes an inverse phase change of the spin at a new position, the quantity measured is actually the average phase changes of a spin under the two field gradient pulses,

$$E(q) = \langle e^{-i\mathbf{q} \cdot \mathbf{r}(0)} e^{i\mathbf{q} \cdot \mathbf{r}(t)} \rangle \quad (1.15)$$

For uniform flow along the grating direction, the grating is shifted by a spatial offset vt , where v is the flow rate and t is the time between the creating and the detection of the grating. To measure this displacement it is sufficient to record the pure phase shift in a calibrated magnetic field gradient. This can be described by analogy to the interference of two waves scattered by two surfaces separated by a distance of vt , as shown graphically in Figure(1-5). Flow measurement in NMR is an example of coherent scattering.

Similarly, random processes such as diffusion can be measured as scattered waves from centers but the distribution of phase offsets result in an observed amplitude change for the ensemble.

The dynamic process of the molecules can be universally specified by the van Hove correlation function[21], expressed as $P(\mathbf{r}|\mathbf{r}', t)$ in this thesis. The average phase change is then,

$$\langle e^{-i\mathbf{q} \cdot \mathbf{r}(0)} e^{i\mathbf{q} \cdot \mathbf{r}(t)} \rangle = \int d^3\mathbf{r} P(\mathbf{r}) e^{-i\mathbf{q} \cdot \mathbf{r}} \int d^3\mathbf{r}' P(\mathbf{r}|\mathbf{r}', t) e^{i\mathbf{q} \cdot \mathbf{r}'} \quad (1.16)$$

The focus of this thesis is to explore the process that is behind the evolution of the magnetization grating due to molecular dynamic mechanisms. As the grating develops under various dynamic mechanisms over time, spatial temporal information of the dynamics can be detected.

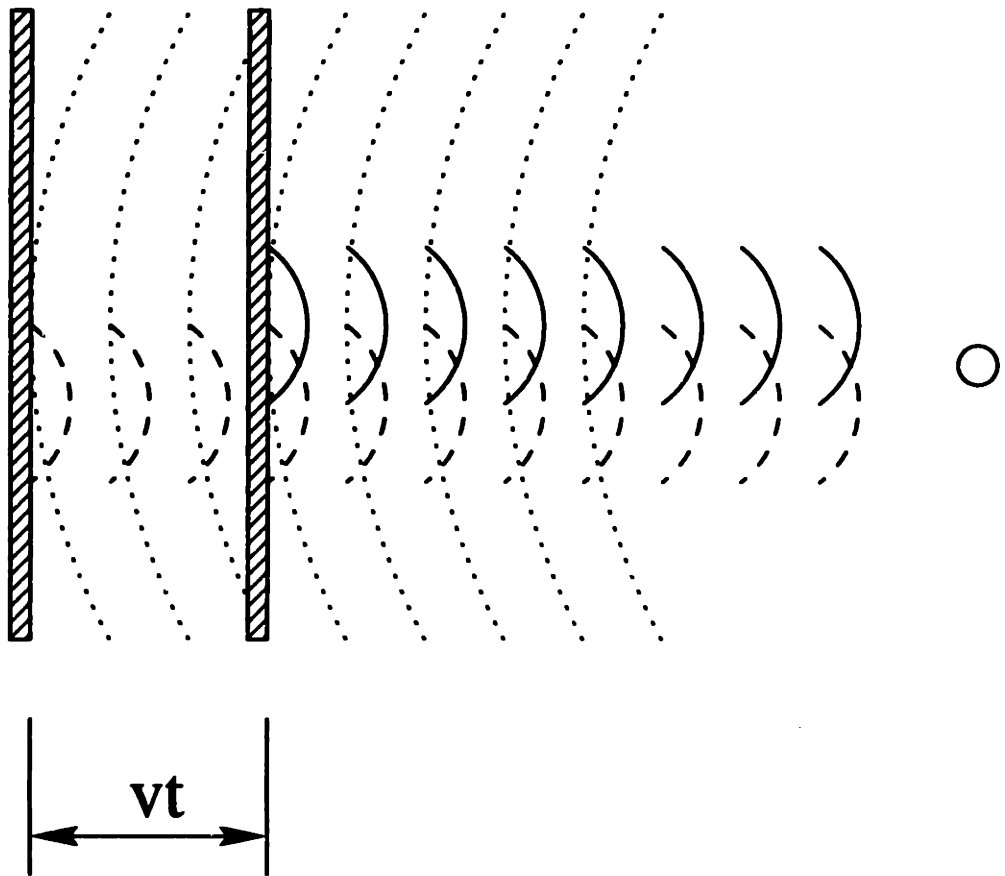


Figure 1-5: Scattering from two parallel planes as an analogy to flow measurement in NMR. Shown flow measurement is a coherent scattering experiment.

1.2.4 Spin Echo and the Stimulated Echo

A spin echo experiment contains two RF pulses spaced by a time interval τ , as seen in Figure(1-6). The first RF pulse tips the magnetization from its equilibrium direction to the transverse plane. The magnetization then precesses about the z axis at the Lamor frequency. As the magnetic field inhomogeneity results in a field spread ΔB_0 across the sample, transverse magnetization phase coherence lasts only for a time in the order of $(\gamma\Delta B_0)^{-1}$. Hahn discovered that this phase coherence loss can be refocused by applying a π RF pulse after a time delay τ . The phase loss due to Hamiltonians that are proportional to I_z during τ will be totally refocused at 2τ and the resulting phase coincidence at 2τ is known as spin echo. The signal intensity at 2τ decays at the intrinsic transverse relaxation time constant T_2 .

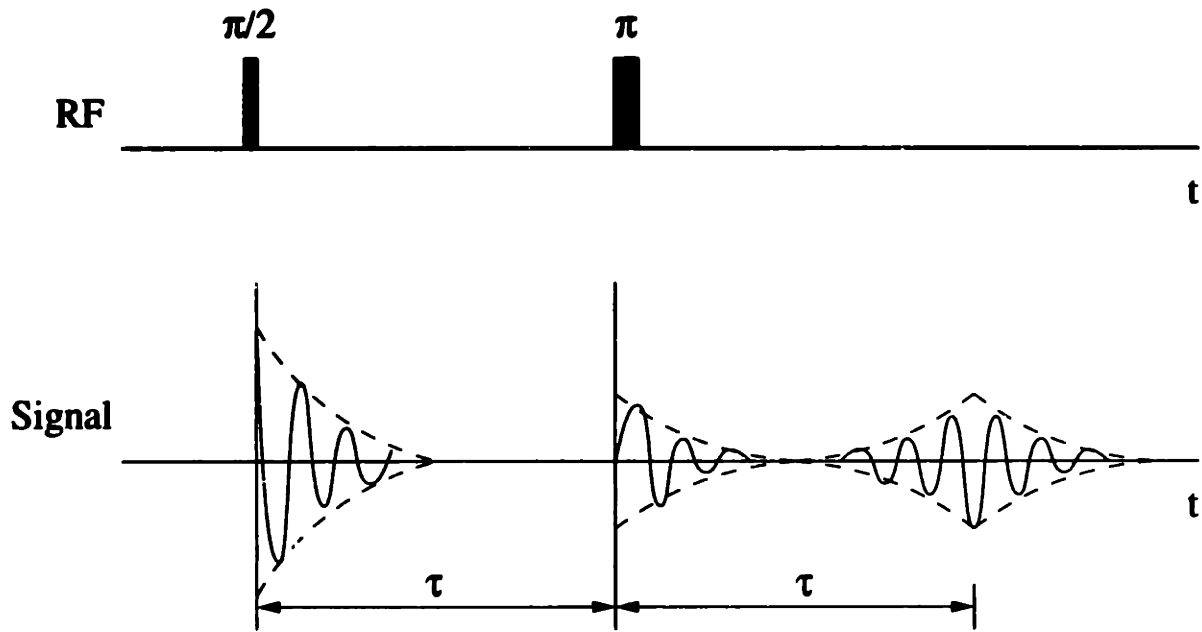


Figure 1-6: Pulse sequence and signal of a spin echo experiment. The echo intensity decays as $e^{-2\tau/T_2}$.

$$M(2\tau) = M_0 e^{-2\tau/T_2}. \quad (1.17)$$

It can be seen that the time window allowed in a spin echo experiment is limited

by the relaxation time T_2 , typically less than several hundreds microseconds.

A stimulated echo experiment is made of three $\frac{\pi}{2}$ pulses, as seen in Figure(1-7) with the time between the first two τ and the time between the last two Δ , where Δ is usually chosen greater than τ . There are three free induction decays and five echoes in a stimulated echo experiment. The amplitudes of the four echoes originated from the first FID are,

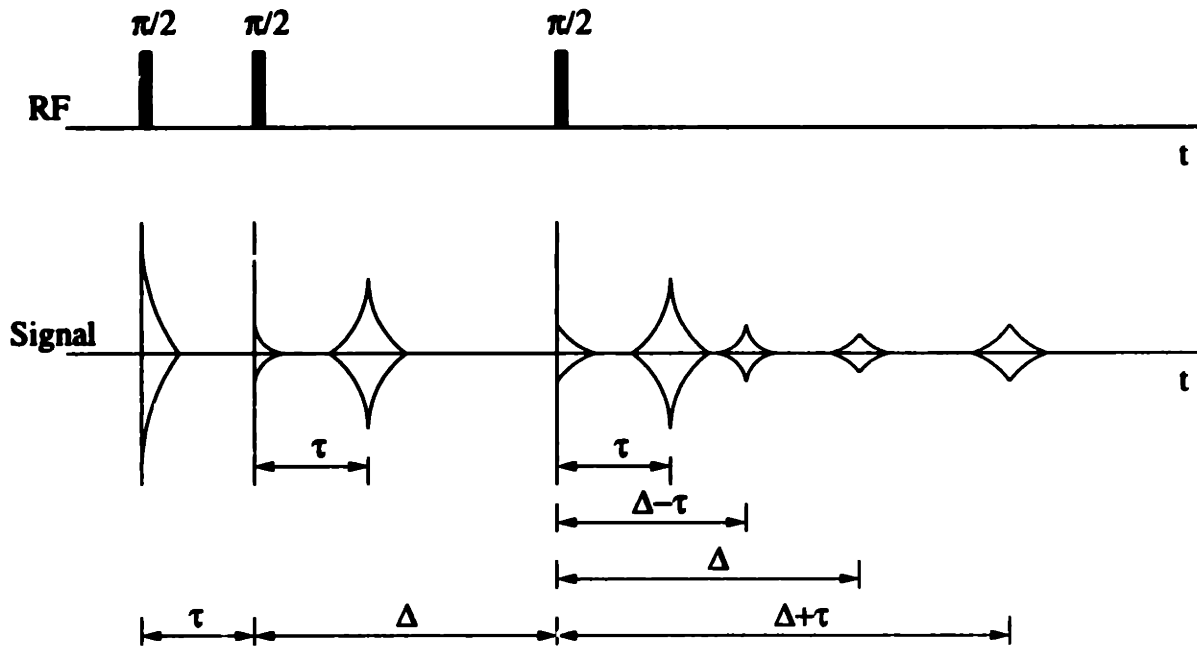


Figure 1-7: Pulse sequence and signal of a stimulated experiment. The intensity of the stimulated echo at $(2\tau + \Delta)$ decays as $e^{-2\tau/T_2}e^{-\Delta/T_1}$.

$$M(2\tau) = \frac{1}{2} M_0 e^{-2\tau/T_2} \quad (1.18)$$

$$M(2\tau + \Delta) = \frac{1}{2} M_0 e^{-2\tau/T_2} e^{-\Delta/T_1} \quad (1.19)$$

$$M(2\Delta) = \frac{1}{2} M_0 e^{-2\Delta/T_2} \quad (1.20)$$

$$M(2\tau + 2\Delta) = \frac{1}{2} M_0 e^{-2(\tau+\Delta)/T_2} \quad (1.21)$$

It can be seen that the echo at $t = 2\tau + \Delta$ decays with the time constant T_1 during

Δ . This can tremendously lengthen the time window as longitudinal relaxation time constant T_1 offers is much longer than T_2 . The spins of interest are stand along the longitudinal axis by the second $\frac{\pi}{2}$ RF pulse and preserved until a measurement needs to be done. There are subtle differences in k space trajectories between a $\frac{\pi}{2} - \pi$ echo and a $\frac{\pi}{2} - \frac{\pi}{2}$ or stimulated echo that will affect the diffusion measurement when more than three gradient pulses are applied. The discussion on this matter will be in the next chapter and in Appendix A.

1.3 Flow and Molecular Diffusion

After a magnetization grating is created in a sample, the measured signal after a time will contain information about the dynamics happened during that period. The two simplest examples are of uniform flow and molecular diffusion.

1.3.1 The Measurement of Flow Rate

If the sample is moving with a uniform flow rate v_z , after a time Δ every spin will have simply moved a distance of $v\Delta$ from their original positions towards z direction and the probability density is,

$$P(z|z', t) = \delta(z - z' + vt). \quad (1.22)$$

Usually, the flow is measured in an uniform tube, therefore $\rho(z) = \text{constant}$, the signal is then,

$$\begin{aligned} E(\Delta) &= \int \delta(z - z' + vt) e^{-ik_z(z-z')} \\ &= e^{-ik_z v \Delta}, \end{aligned} \quad (1.23)$$

where $k_z = \gamma g_z \delta$ and δ is the gradient pulse duration.

It can be seen that this reflects a simple change in the phase factor from which

the flow rate v can be determined. Since the phase is cyclic, aliasing will be present if the phase change is greater than a period. As discussed in the previous section, the flow measurement is a perfect and simple example of NMR coherent scattering experiment and can be described as an analogy to the scattering from two parallel planes separated by the distance the fluid flew.

1.3.2 Isotropic free diffusion

The random motion of molecules will cause a magnetization grating in a sample of infinite extent to gradually lose its coherence. In other words, the phase of the grating at each position is averaged over the local region in which the molecules diffuse. The molecular displacement probability function is obtained by solving the diffusion equation under Fick's Second Law,

$$P(|\Delta \mathbf{r}|, t) = (4\pi Dt)^{-\frac{3}{2}} \exp\left[-\frac{\Delta \mathbf{r}^2}{4Dt}\right] \quad (1.24)$$

The measured scattering signals is,

$$\begin{aligned} E(k) &= \int \frac{1}{(4\pi Dt)^{\frac{3}{2}}} \exp\left[-\frac{(\mathbf{r} - \mathbf{r}')^2}{4Dt}\right] e^{-iqz \cdot (\mathbf{r} - \mathbf{r}')} d^3 \mathbf{r} d^3 \mathbf{r}' \\ &= e^{-\gamma^2 k^2 \delta^2 D \Delta}. \end{aligned} \quad (1.25)$$

This is the most useful equation to determine the self diffusion coefficient in an homogeneous media.

Samples are not infinitely large and are necessarily non-uniform. They have a spatial varying spin density $\rho(z)$. Therefore, after the grating burning gradient, the spin system has the form of a magnetization grating superimposed onto the local spin density function, and can be expressed as,

$$\rho(z, \delta) = \rho(z) e^{-i\gamma g_z \delta z} \quad (1.26)$$

The measurement of the magnetization of this grating as a function of the wave vector k is the Fourier transformation of the spin density. This measurement in magnetic resonance imaging is referred as a constant time imaging(CTI). Each measurement records one component in Fourier space.

$$S(g_z) = \int \rho(z) e^{-i\gamma\delta g_z z} dz \quad (1.27)$$

If there is a delay time Δ between the creation of the grating and the measurement, any evolution of the magnetization grating via molecular motions under a conditional probability density function $P(z|z', \Delta)$, which is also called the van Hove correlation function, will influence the measurement. In most cases, $P(z|z', \Delta)$ is independent of the experiment and only a function of the sample itself. Under this probability density function, the system becomes,

$$\rho(z, \Delta) = \int P(z'|z, \Delta) e^{-i\gamma\delta g_z z'} dz'. \quad (1.28)$$

Again, a measurement is equivalent to taking the integration of the magnetization over the whole sample region,

$$S(g_z, \Delta) = \int P(z'|z, \Delta) e^{-i\gamma\delta g_z z'} dz' dz. \quad (1.29)$$

With the spin density taking into account, the initial positions of the spin are weighted by $\rho(z')$, the final measured signal is,

$$S(g_z, \Delta) = \int \rho(z') P(z'|z, \Delta) e^{-i\gamma\delta g_z z'} dz' dz. \quad (1.30)$$

It can be seen that this is a distortion of the spin density image. Usually in an imaging experiment, most of the molecules are not allowed to diffuse far enough to see the boundaries of the geometric feature; therefore, P is considered only a function of the relative position of the spins ($z - z'$) and independent of their original positions, in other words, it can be written as

$$P(z|z', \Delta) = P(z' - z, \Delta). \quad (1.31)$$

It can be immediately seen that the convolution of P with the original object ρ makes P the point spread function(PSF) due to molecular motions. It's present causes the image to blur. In some cases, it will limit the resolution of the image. The effects of molecular diffusion on magnetic resonance imaging will be discussed in detail in Chapter 6.

If a refocusing gradient pulse is applied before the measurement, the signal is,

$$S = \int \rho(z) P(z'|z, \Delta) e^{-i\gamma\delta g_z(z' - z)} dz dz' \quad (1.32)$$

The attenuation of a spin echo as a function of gradient pulse amplitude g_z , duration δ and the mean square displacement of the spins $\overline{\Delta z^2}$ is determined by

$$E(g_z) = \exp\left(-\frac{1}{2}\gamma^2\delta^2 g_z^2 \overline{\Delta z^2}\right) \quad (1.33)$$

Here, the gradient pulses are assumed to be so short that any movements during the pulse is neglegable. The mean square displacement $\overline{\Delta z^2}$ can be calculated by applying Equation (1.24),

$$\begin{aligned} \overline{\Delta z^2} &= \overline{(z - \bar{z})^2} \\ &= \overline{z^2} - \bar{z}^2. \end{aligned}$$

From Eq. (1.34) and (1.24), $\overline{\Delta z^2}$ can be easily calculated as,

$$\overline{\Delta z^2} = 2Dt. \quad (1.34)$$

Therefore, the echo attenuation due to free diffusion is

$$E(g_z, t) = \exp(-\gamma^2\delta^2 g_z^2 Dt) \quad (1.35)$$

By defining $k_z = \gamma g_z \delta$, Equation(1.35) can be further written as,

$$E(k_z) = \exp(-k_z^2 D t). \quad (1.36)$$

This is the Fourier transform of Equation(1.24). For any given diffusion time t , the echo attenuation is a Gaussian function in terms of the wave vector k_z and hence gradient amplitude g_z or gradient duration δ . For any given wave vector k_z , the echo attenuation function is an exponential decay in terms of diffusion time t .

1.3.3 Anisotropic diffusion

For anisotropic diffusion, the diffusion constant D is replaced by a tensor. If the measurements are made only in the principle axis system(PAS) and therefore only the diagonal elements of the diffusion constant tensor is non-zero and different, i.e. $D_{xx} \neq D_{yy} \neq D_{zz}$, indicating different diffusion properties along PAS axis. The solution to the diffusion equation with such a tensor is,

$$P(\Delta r, t) = (4\pi t)^{-\frac{3}{2}} \frac{1}{\sqrt{D_{xx} D_{yy} D_{zz}}} \exp \left[- \left(\frac{\Delta x^2}{4D_{xx}t} + \frac{\Delta y^2}{4D_{yy}t} + \frac{\Delta z^2}{4D_{zz}t} \right) \right]. \quad (1.37)$$

And the mean square of the displacement is,

$$\overline{\Delta r^2} = \overline{\Delta x^2} \sin^2 \theta \cos^2 \phi + \overline{\Delta y^2} \sin^2 \theta \sin^2 \phi + \overline{\Delta z^2} \cos^2 \theta. \quad (1.38)$$

For a system with bulk order, i.e, all the geometric units are aligned in the same way, the echo attenuation is,

$$E(g_r) = \exp[-\gamma^2 \delta^2 g_r^2 D_e t], \quad (1.39)$$

where D_e is the effective diffusion coefficient measured along the gradient direction r ,

$$D_e = D_{xx} \sin \theta \cos \phi + D_{yy} \sin \theta \sin \phi + D_{zz} \cos \theta. \quad (1.40)$$

It can be seen that Equation(1.39) and Equation(1.35) have no qualitative differences. Only the diffusion coefficient is different.

Many systems have no bulk orders, in other words, the local geometric units are with anisotropic properties while the system as a whole is uniform. This means that an integration must be taken over all the orientation angles in Equation(1.38).

The problem can be divided into three cases:

Homogeneous or 3-D

The Echo attenuation function for a 3-D homogeneous sample is Gaussian and expressed by Equation(1.35).

Planar or 2-D

For 2-D case, where diffusion is restricted to being within a plane, if the in-plane diffusion constant is uniform, i.e., $D_{||} = D_{zz} \ll D_{\perp} = D_{xx} = D_{yy}$, the echo attenuation is,

$$E_{2D}(g_r) = \exp [-\gamma^2 \delta^2 g_r^2 D_{\perp} t] \int_0^1 \exp [\gamma^2 \delta^2 g_r^2 D_{\perp} x^2] dx. \quad (1.41)$$

Linear or 1-D

For the 1-D case, where diffusion is restricted to being along a line, i.e., $D_{||} \gg D_{\perp}$, the echo attenuation is,

$$E_{1D}(g_r) = \int_0^1 \exp [-\gamma^2 \delta^2 g_r^2 D_{||} x^2] dx. \quad (1.42)$$

In summary,

$$\begin{aligned} E_{3D}(g_r) &= \exp (-\gamma^2 \delta^2 g_r^2 D t) \\ E_{2D}(g_r) &= \exp [-\gamma^2 \delta^2 g_r^2 D_{\perp} t] \int_0^1 \exp [\gamma^2 \delta^2 g_r^2 D_{\perp} x^2] dx \end{aligned} \quad (1.43)$$

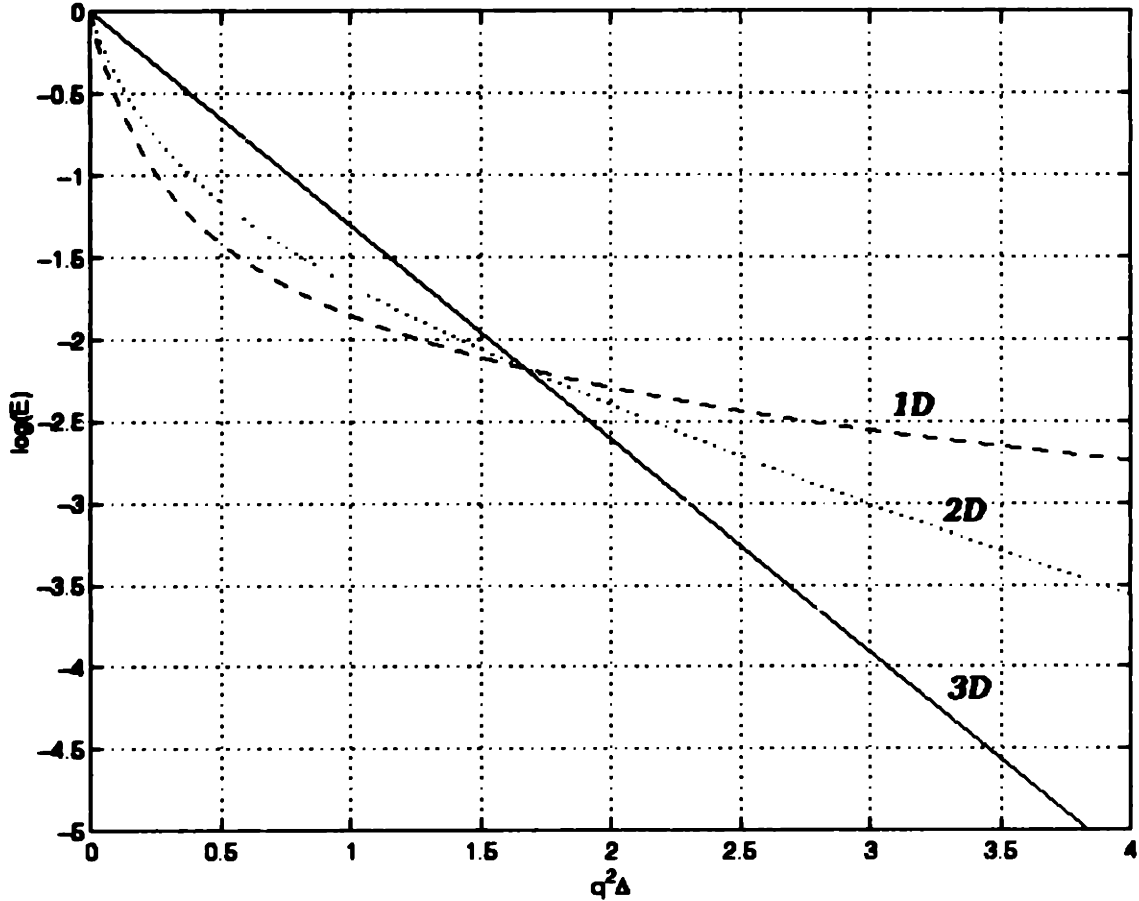


Figure 1-8: $q^2\Delta$ dependence of echo attenuation curves in 1-D, 2-D and 3-D diffusion calculated by Equations(1.44).

$$E_{1D}(g_r) = \int_0^1 \exp [-\gamma^2 \delta^2 g_r^2 D_{||} x^2] dx$$

As it can be seen in Figure(1-8), the dependence of E_{1D} , E_{2D} and E_{3D} on $\gamma^2 \delta^2 g_r^2 t$ shows different curvatures in the $\log E(q_r)$ versus $\gamma^2 \delta^2 g_r^2 t$ plot. By comparing the curvature of measured echo attenuation with the three curves, we are able to characterize the dimensionality of the spin system. This method determines the over all dimensionality by virtue of the diffusive behavior parallel to surfaces, i.e., along the direction that is least restricted; therefore, it does not provide the scale of the restrictive compartment. Nevertheless, its appearance in the laboratory frame reflects a characteristic spatial dimentionality. In addition, changing of curvature of echo at-

tenuation function can be caused by many other reasons, e.g., multiple-diffusion constants and size/shape distributions. There are certain ambiguities in interpretation of the results. Certain assumptions must be made in order to avoid the ambiguities in structure or behavior.

The translational motion of molecules in a sample with heterogeneous structures will be influenced by boundaries. These restrictions mean that the distribution of displacements described by the conditional probability function $P(r|r', \Delta)$ may not be Gaussian anymore and will have a temporal dependence characteristic of the length scales and the local molecular self-diffusion constant. In his early papers on pulsed gradient spin echo measuring molecular diffusion, Stejskal pointed out that it can be used as a potential useful tool of probing the micro structure and introduced the concept of diffusion data analysis in the Fourier space. Since the late 1980's, the PGSE experiments have been looked upon with new prospectives, e.g., q -space imaging and scattering. There have been successful simulations and experiments on phantom samples since then.

1.4 Summary

Although gradient NMR experiments have been around for more than 35 years, only recently have people started to look at the experimental results in terms of a dynamic structure factor. NMR specialists are tempted to take the advantage of the full-fledged scattering formulism developed over the span of this century. However, the exploration of relationship of NMR experiments to scattering methods is still in the early stage. In this thesis NMR as a scattering experiment is introduced by the behavior of the magnetization grating—the “wave” in NMR scattering, under varies dynamical process. In Chapter 3, the scattering in NMR is expanded to a field where NMR is unique to other scattering methods, the multiple scattering experiment. It is demonstrated in theory and experiments that double scattering experiments correlates the Van Hove correlation functions along orthogonal directions in the principle axis system of the microscopic compartments. Microscopic diffusion anisotropy can be

measured in a glassy sample with no bulk alignments. In Chapter 4 and Chapter 5, the discussion moved on to a particular example of NMR double scattering experiment performed on yeast cells with different eccentricities. Chapter 6 discusses the influence of the magnetization grating in restrictive geometries on NMR microscopy. The details in k pathway selection and filtering of single scattering events via RF and ADC phase cycling are listed in Appendix A.

Chapter 2

NMR Scattering

To explore molecular displacements in condensed phase, the most useful experimental methods identify dynamic processes with respect to their spatial and temporal behaviors. A given type of motion defines a certain dynamic structure in space. Every scattering experiment leads to a dynamic structure factor $S(\mathbf{q}, \omega)$ or its four dimensional, i. e., spatial and temporal, Fourier transform, also known as the van Hove correlation function[21] $G(\mathbf{r}, t)$. $G(\mathbf{r}, t)$ denotes the probability of finding a particle at time t at position \mathbf{r} if at an earlier time $t = 0$ some other or the same particle had been at $\mathbf{r} = 0$. In NMR scattering, this quantity is denoted as, in a more general form, $P(\mathbf{r}|\mathbf{r}', t)$ where the initial position is at \mathbf{r}' and the probability is of the same particle displacement.

By incoherent neutron scattering[30], the Van Hove auto-correlation function at spatial regime of $0.1 \rightarrow 10\text{\AA}$ and temporal regime of $< 10^{-8}\text{s}$ is obtained. Although there has been a lot of effort to extend the temporal window toward longer times, i.e. higher energy resolution, processes slower than 10^{-8}s remain difficult to access with neutron scattering. Other scattering techniques such as Mössbauer- Rayleigh scattering can sample beyond this limit but still doesn't provide sufficient intensity for practical applications.

A different approach to extend the dynamic range toward processes slower than 10^{-8}s without losing the information about the microscopic geometry of the process is NMR which measures temporal regime of $10^{-3}\text{s} - 10^1\text{s}$ and spatial regime of

$10^{-6} - 10^2 m$. Because of recent interest in NMR imaging and NMR microscopy, there have been a number of interpretations of NMR dynamics in terms of a dynamic structure factor. In this chapter, the behavior of magnetization grating created in NMR experiments is studied by looking at the evolutions of such grating under different physical processes. To establish a generalized NMR scattering formulism, some comparisons are made to the traditional scattering methods which we hope avoid drawing any forced or farfetched analogies.

2.1 The Effects of Radio Frequency Pulses on a Magnetization Grating

An on resonance($\omega_{RF} = -\gamma B_0$) radio frequency(RF) pulse applied in an external longitudinal field is equivalent to a magnetic field transient(effective magnetic field) in the transverse plane in the frame that is rotating around z axis with the same RF frequency[19]. The effect of the RF field is to rotate the magnetization vector around the direction of the RF at a frequency of,

$$\omega_1 = -\gamma B_1, \quad (2.1)$$

where B_1 is the amplitude of the RF field. The duration of the RF pulse determines the tip angle. Since the spin's motion is the result of a magnetic torque, the RF pulse does not change the magnetization component along the same direction as the RF field. The influences of RF pulses with various durations($\frac{\pi}{2}$ and π) and phases(x' and y') on each magnetization component(I_x , I_y and I_z) are summarized in Table(2.1).

As homogeneous RF pulses change the phase of all the perpendicular magnetizations by the same amount, they will not change the wave number of the grating, but can change the phases of the spin magnetization and hence change the appearance of the grating. For example, a π pulse along the x' axis in the rotating frame applied to a sample with a magnetization grating Me^{-ikx} rotates the magnetization components along the y' axis, $-M \sin kx$, into $-y'$ axis, while leaving the components along the

RF		$e^{\pm iku}$	$\sin ku\hat{z}$	$\cos ku\hat{z}$
$\frac{\pi}{2}$	x'	$+ \frac{1}{2} (e^{iku} + e^{-iku}) \mp \sin ku\hat{z}$	$+ \frac{1}{2} (e^{iku} - e^{-iku})$	$+ \frac{i}{2} (e^{iku} + e^{-iku})$
	y'	$\pm \frac{1}{2} (e^{iku} + e^{-iku}) + \cos ku\hat{z}$	$+ \frac{i}{2} (e^{iku} - e^{-iku})$	$- \frac{1}{2} (e^{iku} + e^{-iku})$
π	x'	$+ e^{\mp iku}$	$- \sin ku\hat{z}$	$- \cos ku\hat{z}$
	y'	$- e^{\mp iku}$	$- \sin ku\hat{z}$	$- \cos ku\hat{z}$

Table 2.1: Table shows effects of different RF pulses on spin magnetization grating within transverse plane and along \hat{z} axes.

x' axis, $M \cos kx$, unchanged. As a result, the wave-vector grating changes sign and the grating becomes Me^{ikx} , as shown in Figure(2-1).

For a $\frac{\pi}{2}$ pulse applied along the x' axis, the magnetization components along the y axis are tipped to the longitudinal direction -not measurable, and only the components along the x axis, $M \cos kx$, are left in the transverse plane. The resulting grating in the transverse plane is $M \cos kx$, or equivalently $\frac{1}{2}(e^{ikx} + e^{-ikx})$. A complete description of RF pulses on magnetization grating can be found in Sodickson's thesis[31].

2.2 Pulsed Gradient Spin Echo Experiments

All NMR scattering experiment, including the simplest pulsed gradient spin echo (PGSE) experiment, contains three stages of NMR scattering process: creation, evolution and detection of the magnetization gratings. The three processes can be treated as analogies to incoming wave, scattering under a potential and outgoing wave detected.

Figure(2-2) shows the pulse sequence of a PGSE experiment. The magnetization grating with wave number $k = \gamma G \delta$ is created by applying a magnetic field gradient pulse with amplitude G for a duration of δ after the first $\frac{\pi}{2}$ RF pulse. During the diffusion or mixing time Δ , the grating is allowed to evolve under certain dynamic processes such as bounded diffusion. At the grating detection stage, the measurement of the k' component of the grating can be accomplished by measuring the total magnetization after a gradient pulse corresponding to a k' grating is applied. For

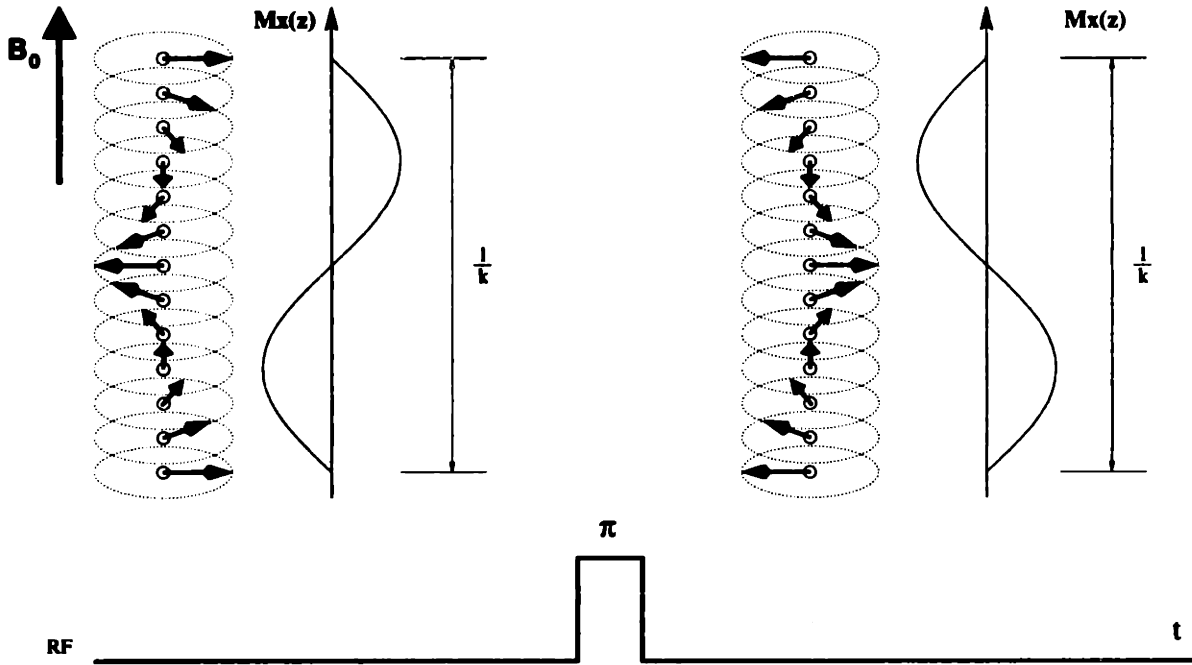


Figure 2-1: A π RF pulse does not change the wave number of the magnetization grating. However, it inverts the grating's direction.

unbounded diffusion in an infinite extent, the grating will only see a attenuation in amplitude - the wave number is kept the same. Therefore, in a normal PGSE experiment, only an identical gradient pulse is applied in the detection stage because only the components of the same wave number as the initial grating is measured. In general NMR scattering measurements, the detecting gradient pulse is not neccesarily the same as the creation pulse.

In some cases, the restrictive behavior of molecular movement can be approximated by a restraining potential function as suggested by Stejskal[7]. For most of the cases, however, the restrictive process is treated as under influences of reflecting walls and often solved by analogy to heat transfer equations under identical boundary conditions.

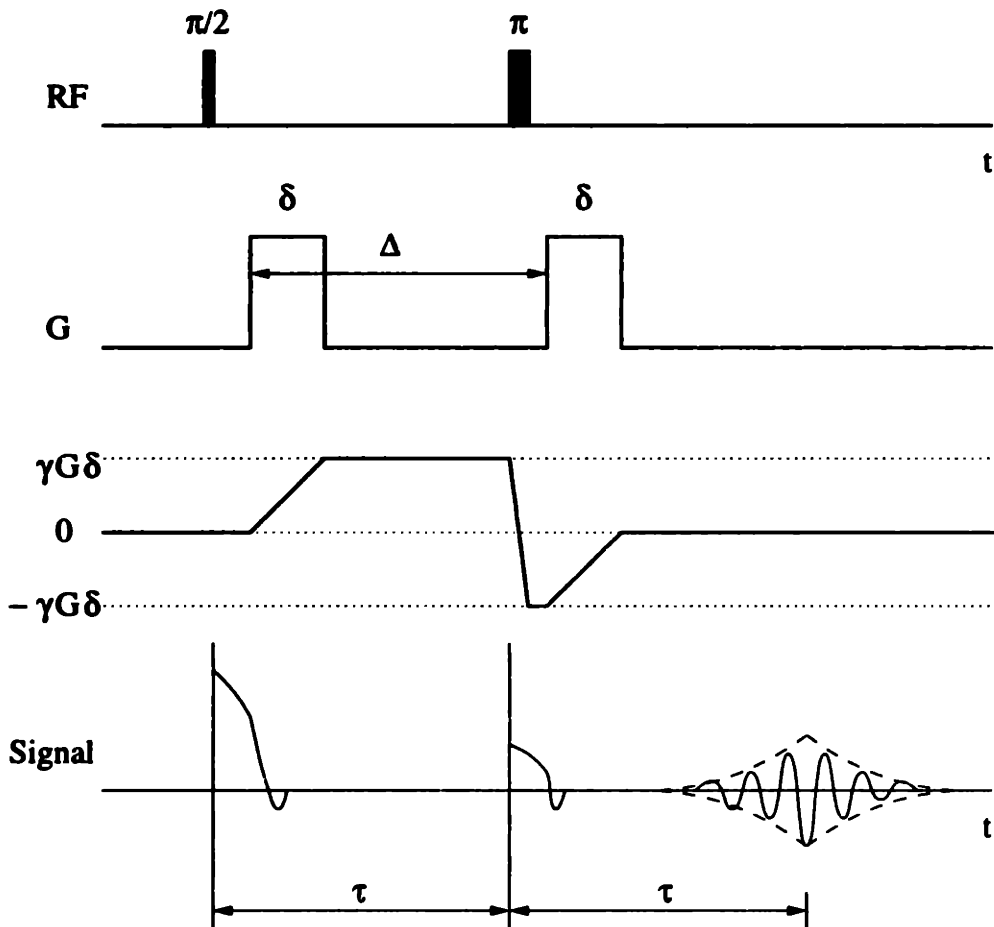


Figure 2-2: Pulse sequence of a PGSE experiment. The first RF pulse tips the spin magnetization from its equilibrium position z to the transverse plane. The first gradient pulse will superimpose a magnetization grating into the sample. The wave number is determined by $k = \gamma G \delta$. The π RF pulse inverts the magnetization grating that has evolved during Δ . The second gradient pulse is identical to the first one. It refocuses the component with the same wave number k and the coherent of phases is re-established and measured at 2τ when an spin echo is observed.

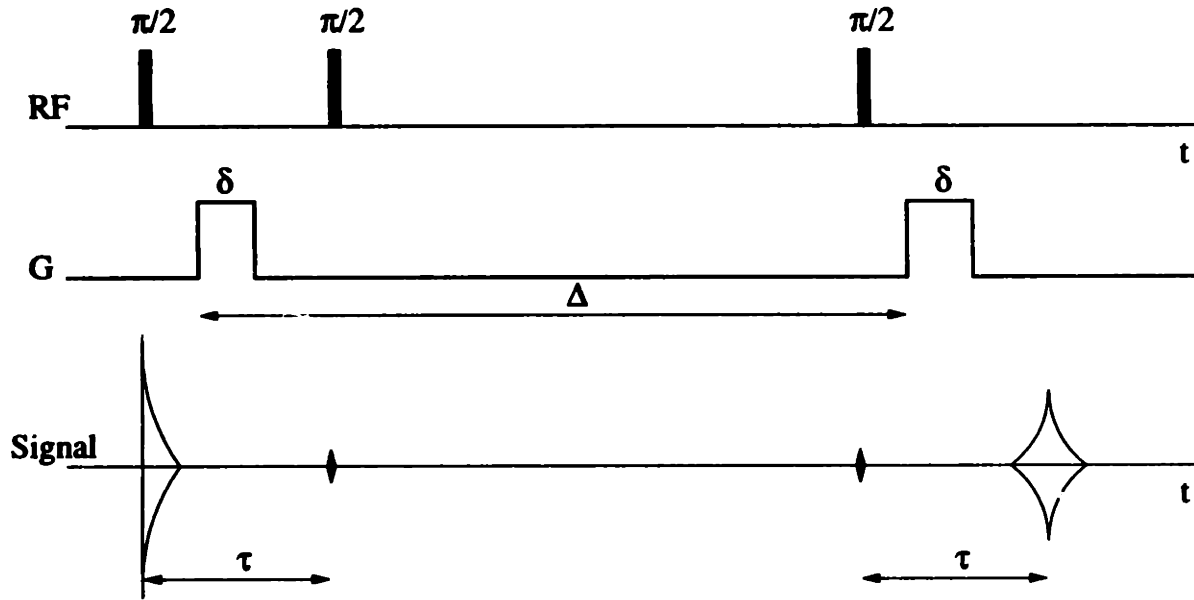


Figure 2-3: Diffusion experiment using the stimulated echo and pulsed field gradients. The range of dynamic that can be measured is extended to longer times. The time window of a stimulated echo is on the order of seconds.

2.3 Pulsed Gradient Stimulated Echo Experiment

The stimulated echo of a three pulse experiment is shown to be useful in extending the range of measurement of diffusion coefficients to more viscous matter where the diffusive correlation time is longer than the transverse relaxation time T_2 . The use of a stimulated echo experiment can significantly widen the time window of the dynamic processes to be measured because during the storage time, the magnetization coherence is along the z axis and only decays at a rate of the longitudinal relaxation time. As the RF pulse in the transverse plane has no effects on the magnetization components that are in the direction of the applied RF pulse, only half of the magnetization coherence will be tipped back to the longitudinal direction and preserved. The half that is left in the transverse plane decays as T_2 relaxation time or is intentionally destroyed by a crusher gradient pulse. Figure(2-3) shows the pulse sequence of a pulsed gradient stimulated echo experiment. The spin magnetization evolves as following, if no molecular displacement is considered,

$$I_z \xrightarrow{\frac{\pi}{2}z} I_y \xrightarrow{G} I_y \cos kx + I_x \sin kx \xrightarrow{\frac{\pi}{2}z} -I_z \cos kx + I_x \sin kx \quad (2.2)$$

$$\xrightarrow{\text{Crush}} -I_z \cos kx \xrightarrow{\frac{\pi}{2}z} -I_y \cos kx \xrightarrow{G} -I_y \cos^2 kx - I_x \sin kx \cos kx \quad (2.3)$$

It can be seen that in a PGSTE experiment, the evolving magnetization grating is cosine modulated. It can be decomposed as two parts with opposite k wave vectors,

$$\cos kx = \frac{1}{2}(e^{-ikx} + e^{ikx}). \quad (2.4)$$

The measurement of a cosine modulated grating by applying a gradient pulse identical to the one that created the grating will unwrap one term of the grating and more tightly wrap the other grating component. Since only the integrated magnetization over the whole sample contributes to the signal, the signal from the tightly wrapped grating components will be average to zero. However, if more gradient pulses are applied, this magnetization component may contribute to a future echo intensity. This is a concern in the multiple scattering experiments and is discussed in the next chapter and in Appendix A.

2.4 Correlation Equations for 1-D PGSE/PGSTE Experiments

The sample has a spatial varying spin density $\rho(\mathbf{r})$. Therefore, after the grating burning gradient, the spin system has the form of a magnetization grating superimposed onto the local spin density function, and can be expressed as,

$$\rho_s(\mathbf{r}) = \rho(\mathbf{r})e^{-i\gamma\delta g\hat{x}\cdot\mathbf{r}} \quad (2.5)$$

Now the spin system will evolve by molecular motions under a conditional probability density function $P(\mathbf{r}'|\mathbf{r}, t)$. After the system has evolved for a time Δ the spin

system becomes,

$$\rho_s(\mathbf{r}, \Delta) = \int P(\mathbf{r}'|\mathbf{r}, \Delta) e^{-i\gamma g \hat{x} \cdot \mathbf{r}'} d^3 \mathbf{r}' \quad (2.6)$$

For many cases such as free diffusion, $P(z'|z, \Delta)$ can be written as function of the relative displacement of the molecules ($\mathbf{r} - \mathbf{r}'$) regardless of the initial positions,

$$P(\mathbf{r}|\mathbf{r}', \Delta) = P(\mathbf{r} - \mathbf{r}', \Delta). \quad (2.7)$$

After the second gradient pulse intended to unwrap the phase twist to measure the coherent magnetization, the signal as a function of $q = \gamma g \delta$ is,

$$E(q) = \int \rho(\mathbf{r}) P(\mathbf{r}'|\mathbf{r}, \Delta) e^{-iq \hat{x} \cdot (\mathbf{r}' - \mathbf{r})} d^3 \mathbf{r} d^3 \mathbf{r}' \quad (2.8)$$

In his original paper on pulsed gradient echo in restricted diffusion study, Stejskal pointed out that the analysis of the data could be more informative in the Fourier reciprocal space. He used a method very close to a scattering approach of interpreting $P(\mathbf{r}'|\mathbf{r}, t)$ as a solution of a wave function with an attractive potential. In the field of neutron scattering, the elastic incoherent structure function(EISF) is calculated as,

$$|S(\mathbf{q})|^2 = \left| \int e^{\frac{V(\mathbf{r})}{k_B T}} e^{-i\mathbf{q} \cdot \mathbf{r}} d^3 \mathbf{r} \right|^2 \quad (2.9)$$

Obviously, for dynamic mechanisms, such as free diffusion or flow, the probability of a particular displacement is independent of the initial position and the probability function can be obtained by an inverse Fourier transform. However, this is only true for short time diffusion limits in which the root mean square of the displacement is far smaller than the spatial scale of the local geometric features, and where $\rho(\mathbf{r})$ can be treated as constant.

However, in the long time limit, i.e. the root mean square(r.m.s.) of the spin displacement during Δ is larger than the features in the sample so that the spin can be bounced back and forth within the boundaries and hence lose any “memory” of

its original position, Equation(2.8) can then be written as,

$$\begin{aligned} E(q) &= \int \rho(\mathbf{r})\rho(\mathbf{r}')e^{-iq\hat{x}\cdot(\mathbf{r}'-\mathbf{r})}d^3\mathbf{r}d^3\mathbf{r}' \\ &= \int \rho(\mathbf{r})e^{iq\hat{x}\cdot\mathbf{r}}d^3\mathbf{r} \int \rho(\mathbf{r}')e^{-iq\hat{x}\cdot\mathbf{r}'}d^3\mathbf{r}'. \end{aligned} \quad (2.10)$$

It can be easily seen that the equation is the product of the Fourier transform of the spin density $\rho(\mathbf{r})$ and its complex conjugate,

$$E(q) = |S(q)|^2, \quad (2.11)$$

where,

$$S(q) = \int \rho(\mathbf{r})e^{iq\hat{x}\cdot\mathbf{r}}d^3\mathbf{r} \quad (2.12)$$

The inverse Fourier transformation of $E(q)$ is the auto-correlation of the spin density function, also known as the generalized Patterson function[32],

$$\begin{aligned} I(x) &= \int \rho(\mathbf{r})\rho(\mathbf{r} + x\hat{x})d^3\mathbf{r} \\ &= \rho(x) \odot \rho(x), \end{aligned} \quad (2.13)$$

where,

$$\rho(x) = \int \rho(\mathbf{r})dydz. \quad (2.14)$$

The Patterson function is widely used in scattering and diffraction to interpret experimental data especially in crystallography where the samples possess lattice structures, the Patterson function shows strong coherence peaks. However, for the incoherent scattering experiments, the main peak at $q = 0$ is dominant and almost includes all the information. This is the main reason that analysis often consists of fitting the main peak with models to extract the structural information.

2.5 The Patterson Function

2.5.1 Definition of the Patterson Function

The solution to the correlation function involves assigning phases to the measured power spectrum $|S(\mathbf{q})|$, since a direct Fourier transformation of $|S|$ will yield the spin density map or imaging. While no completely automatic technique exists for obtaining these phases, there are some approaches that are always possible and may yield useful information. One of these approaches is known as *Patterson synthesis* after A. L. Patterson who initiated this technique in 1934. Patterson sought to obtain information directly from measured $|S|^2$'s by considering their Fourier Transform.

It has been well known in magnetic resonance imaging that the direct mapping in reciprocal space of a sample of spin density $\rho(\mathbf{r})$ is given by:

$$S(\mathbf{q}) = \int_V e^{-i\mathbf{q} \cdot \mathbf{r}} dV, \quad (2.15)$$

so the corresponding intensity is

$$S(\mathbf{q})S^*(\mathbf{q}) = \int_V \rho(\mathbf{r})e^{-i\mathbf{q} \cdot \mathbf{r}} dV \int_{V'} \rho(\mathbf{r}')e^{i\mathbf{q} \cdot \mathbf{r}'} dV'. \quad (2.16)$$

Substituting $\mathbf{r} - \mathbf{r}' = \mathbf{u}$, and rearranging

$$S(\mathbf{q})S^*(\mathbf{q}) = \int_{V_u} \left\{ \int_{V'} \rho(\mathbf{u} + \mathbf{r}')\rho(\mathbf{r}')dV' \right\} e^{-i\mathbf{q} \cdot \mathbf{u}} dV \quad (2.17)$$

$$= \mathfrak{F}\{I(\mathbf{u})\} \quad (2.18)$$

where,

$$I(\mathbf{u}) = \int_{V'} \rho(\mathbf{u} + \mathbf{r}')\rho(\mathbf{r}')dV', \quad (2.19)$$

which is known as the *Patterson function*. Thus we see that if we take the inverse transform of the measured intensity $S(\mathbf{q})S^*(\mathbf{q})$, we obtain the Patterson function:

$$\mathfrak{F}^{-1}\{S(\mathbf{q})S^*(\mathbf{q})\} = \int_{V_q} |S(\mathbf{q})|^2 e^{i\mathbf{q} \cdot \mathbf{r}} dV \quad (2.20)$$

$$= I(\mathbf{r}), \quad (2.21)$$

From the definition in Eq.(2.19), it can be seen that the *Patterson function* will have large values only when $\rho(\mathbf{r})$ and $\rho(\mathbf{u}+\mathbf{r})$ are both large, i.e., for \mathbf{u} equal to inter-porous vectors. That is, it is a function which shows peaks for all inter-porous vectors in the structure, provided that these pores are connected by narrow paths. These peaks will be broader than the individual pores, since $I(\mathbf{u})$ will still have finite values when either $\rho(\mathbf{r})$ and $\rho(\mathbf{u} + \mathbf{r})$ (but not both) is small. Thus a vector joining pores of diameters d_A and d_B will have a Patterson peak of diameter $(d_A + d_B)$. Further more, the areas of the peaks are the products of the spin densities at the two ends of the vector involved.

A one-dimensional example is illustrative. Consider the system consists of three interlinked pores located at x_1, x_2, x_3 . The Patterson function for $\rho(x)$ is

$$I(x) = \int \rho(x+u)\rho(u)du \quad (2.22)$$

To obtain this result for a fixed x , we must take ρ at each point u and multiply it by ρ evaluated at $x+u$, then sum these values up for all u . Peaks will occur at values of x equal to $x_2 - x_1, x_1 - x_2, x_3 - x_1, x_1 - x_3, x_2 - x_3$ and $x_3 - x_2$, as shown in Fig. The peak at the origin of $I(x)$ is due to all inter-porous vectors $x = 0$, i.e., the sum of all terms of the type $\rho^2(u)$ for each pore. For n pores or cells in the system, there are n such peaks at $x = 0$ and they are all summed up as a unique major peak. For a system of isolated pores, only this peak will be detected. For simple interconnected pore system like this, the structure can be easily inferred from the Patterson function.

2.5.2 Correlation Functions of Simple Geometries

There are certain simple geometries in one and two dimensional cases, such as a top hat function and cylinder. The correlations or Patterson functions can be easily obtained and are shown in Figure(2-4). For an ensemble of isolated pores, even if they are aligned in a lattice structure, there are no NMR detectable coherence peaks

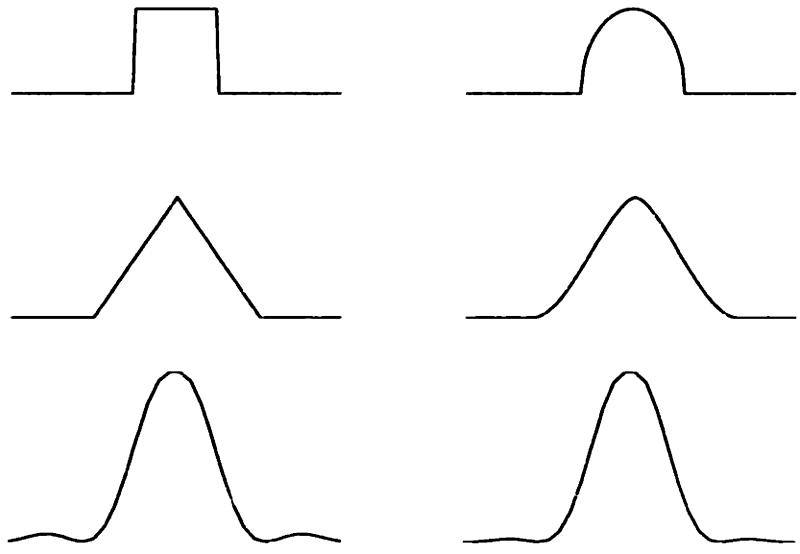


Figure 2-4: Simple spin density function, their auto-correlation and scattering curves, i.e. Fourier transforms of the correlation functions. Left: 1-D top-hat pore; Right: 2-D cylindrical pore. From top to bottom: spin density functions, correlation functions and scattering curves.

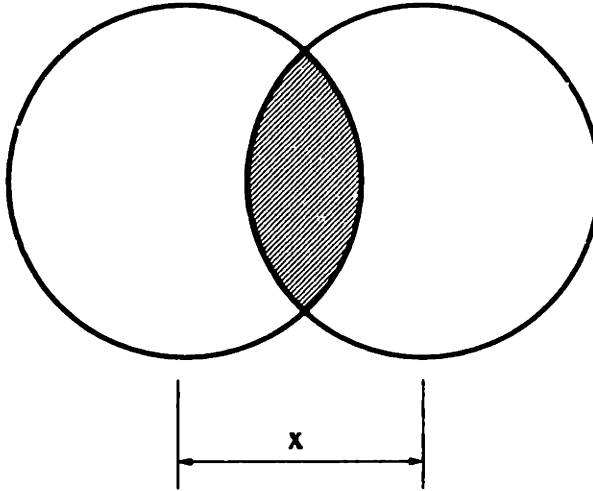


Figure 2-5: A pore and its “ghost”, displaced from it by x . Their convolution is the common shaded area.

corresponded to the alignment, as the movement of molecules is bounded within each pores. However, if the pores are interlinked by thin channels whose contribution of spin density function can be ignored, there will be coherence peaks in the scattering curve that are linked to the flux between the pores. Nevertheless, the flux between pores is so small compared to the probability that the molecules will stay in the same pore, the coherence peaks are hardly discernible. The bright side is that these coherence peaks appear at the low q region of the curve as the spatial length scale of the inter-porous distance is much larger compare with the size of the actual porod region. Studies on this can be found in paper by Kuchel *et al*[33].

2.5.3 Obtaining Other Information from Patterson Function

The most common pore geometry is well approximated by a sphere with radius a . The Patterson function $I(x)$ of such a geometry with spin density zero outside and unity inside is the common volume between the spherical pore and it's “ghost” displaced by x , as in Figure(2-5).

The Fourier transform of a sphere is,

$$FT\{I(r)\} = \frac{4}{3}\pi a^3 \left\{ \frac{3[\sin qa - qa \cos qa]}{(qa)^3} \right\} \quad (2.23)$$

The scattering signal $E(q)$ is proportional to the square of this

$$E(q) \propto \left[\frac{1}{q^6} + \frac{2a^2}{q^4} + \left(\frac{2a^2}{q^4} - \frac{1}{q^6} \right) \cos 2qa - \frac{4a}{q^5} \sin 2qa \right] \quad (2.24)$$

For large q , the terms with q 's higher than powers of four can be ignored and the equation is rewritten as,

$$E(q) \propto \frac{S}{q^4} (1 + \cos 2qa). \quad (2.25)$$

Here, S is the total surface area within the sample. The oscillations arise due to the trigonometric term and will be present only if the size distribution is narrow. For a sample with a relatively broader size distribution, the trigonometric term will cancel due to contributions from the various size distribution of a . Dividing the signal by the signal at $q = 0$, all the constants are gone and surface to volume ratio can be obtained by fitting the curve:

$$\frac{S(q)}{S(0)} = 2\pi \frac{S/V}{q^4} \quad (2.26)$$

As we are measuring a surface to volume ratio, the inverse of this is related to an average dimension called the Porod radius, R_p . This is related to a moment of the distribution $\langle R^3 \rangle / \langle R^2 \rangle$.

From the Patterson function, it is possible to obtain not only moments of any size distribution like R_p , but also information on the size distribution itself. Consider the one dimensional Patterson function $I(x)$ and take the average $\langle I(x) \rangle$, for all possible directions of x . We define the “characteristic function”, $\gamma(x)$ as $\langle I(x) \rangle / V$, and $P(x)dV = 4\pi\Delta\rho^2V\gamma(x)dV$. Now the Fourier transform of $I(x)$ is the measured signal,

$$E(q) = \int I(x)e^{-iqx}dx \quad (2.27)$$

With all possible orientations, the exponential term is averaged over the angles and,

$$E(q) = \int P(r) \frac{\sin qr}{qr} dV \quad (2.28)$$

Therefore, the sine transform of $qS(q)$ gives $P(r)r$ or $\gamma(r)$. With $G(l)$ the distribution

of chord lengths through a pore,

$$\gamma(r) = \frac{1}{\bar{l}} \int_0^D (l - r) G(l) dl \quad (2.29)$$

Where D is the maximum length and $\bar{l} = \int_0^D l G(l) dl$. Therefore:

$$\frac{d^2\gamma(r)}{dr^2} = \frac{1}{\bar{l}} G(l) \quad (2.30)$$

Thus, the second derivative of the characteristic function gives the chord length distribution.

2.6 The k and q Gratings and Spaces

In the last chapter, the evolutions of magnetization due to dynamics and structures of a pore system were introduced. This section further discusses the differences between the gratings that correspond to the static structures and coherent motions (which are defined as k gratings), and the gratings that correspond to incoherent motions (which are defined as q gratings).

2.6.1 The k Gratings and Space

By the Fourier theorem, any information concerning structures in a certain domain, e.g., position and time, can be represented by either the coordinates in that domain or the coordinates in its reciprocal domain, wave vector and frequency respectively for the example, through Fourier transformation. Consider a spatial structure described by a spin density $\rho(x)$ in space, an MRI image is taken by mapping the reciprocal space and reconstructed by a Fourier transformation. The measured NMR signal is the sum of the total magnetization with magnitude and phase, of the sample, The measured signal always corresponds to the DC term or the $k = 0$ reciprocal component of the sample,

$$\text{Signal} \equiv \tilde{\rho}(k)|_{k=0}. \quad (2.31)$$

In order to obtain non-zero reciprocal components of the spin density function, the whole reciprocal space is shifted by the creation of magnetization gratings across the sample,

$$\tilde{\rho}(k - k_i)|_{k=k_i} = \tilde{\rho}(k) \otimes \delta(k - k_i)|_{k=k_i} \quad (2.32)$$

$$= \int \rho(x) e^{-ikx} dx|_{k=k_i}. \quad (2.33)$$

The \mathbf{k} grating is created to shift the \mathbf{k} space to measure \mathbf{k} components of the object. Therefore, \mathbf{k} space is the Fourier reciprocal space of the absolute spin density function.

2.6.2 The \mathbf{q} Gratings

To define the \mathbf{q} gratings, let's look at a simple PGSE experiment on a spin system, as shown in Figure(2-6), made of pores centered at x_1, x_2 etc, with identical local spin density functions $\rho(x)$,

$$\rho_t(x) = \sum_i \rho(x - x_i). \quad (2.34)$$

The first RF pulse tips all the spin magnetization to the transverse plane, the first gradient pulse will create a magnetization grating into the sample,

$$\rho_t(x) = \sum_i \rho(x - x_i) e^{-ikx}. \quad (2.35)$$

The molecular diffusive motion of the spins will average the gratings inside each pore. After a time that allows the molecules carrying the spin magnetization to travel longer distance than the size of the pore, the gratings inside each pore will be disappeared while a grating at larger scales still exists because the averaged magnetization inside each pore will reflect the pore's overall location. The spin system is expressed as,

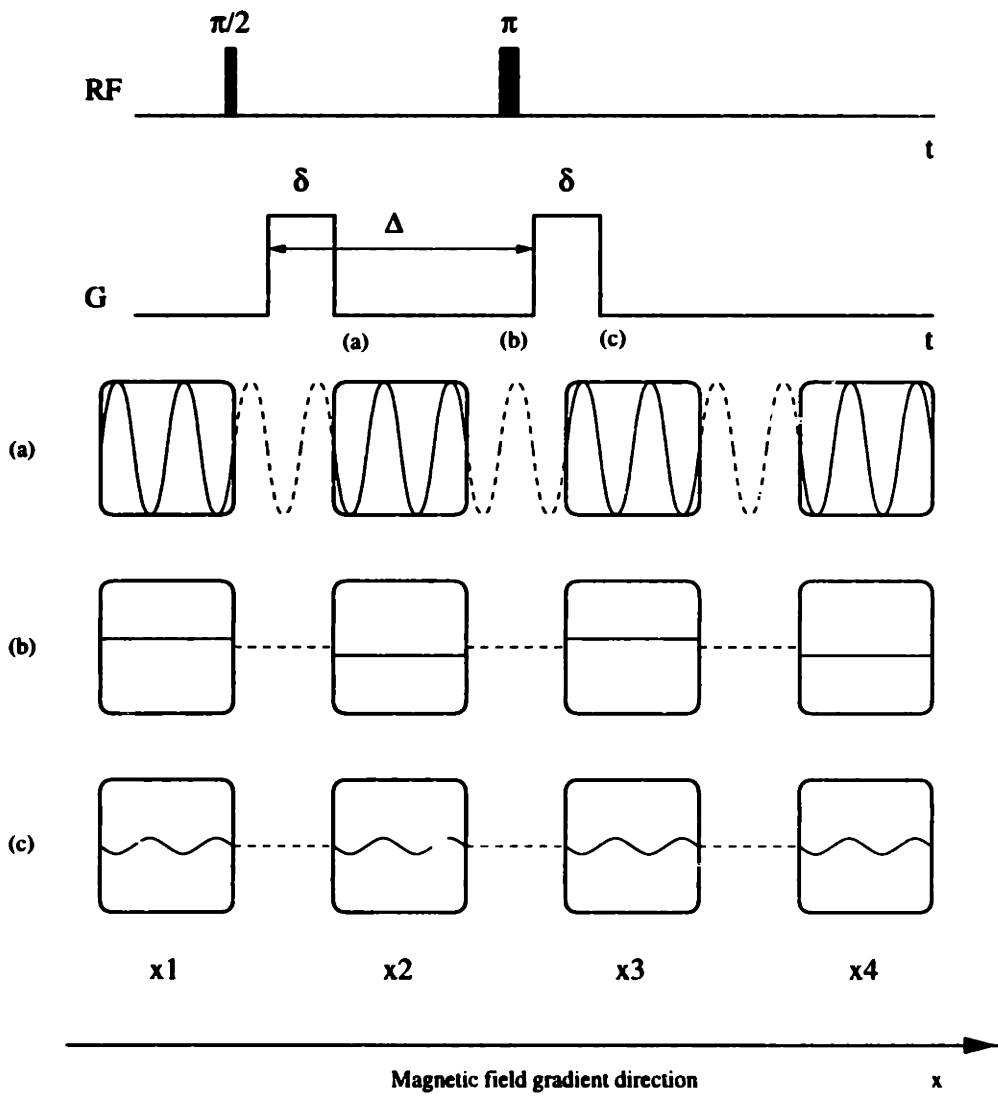


Figure 2-6: A PGSE experiment on a sample with ensemble of bounded pores at different positions. (a) After the first gradient pulse, a k grating is created across the whole sample. (b) The grating inside each pore is smeared out due to long time molecular diffusion. However, the averaged phases of the pores still show features of the k grating. (c) After the second gradient pulse, the leftover k grating is totally refocused. Within each pore, there is a q grating with the wave number the same as the original k grating. The q gratings are identical in phase within the pores.

$$\rho_t(x) = \sum_i \rho(x - x_i) e^{-ikx_i} \int_{\text{pore}} \rho(x') e^{-ikx'} dx'. \quad (2.36)$$

In the equation, the integration is taken over the local pore region which represents the k 'th component in the Fourier space of the pore density function (same for all the pores, as the pores are identical). The phase factor in front of the integral is from the k grating. The k grating doesn't fade away because the pores are at different locations and the spins are not allowed to migrate from one pore to another.

When the second gradient is applied with identical strength and length as the first one after the π pulse which inverts the k of the existing magnetization grating, the spin system is,

$$\rho_t(x) = \sum_i e^{ikx_i} \int_{\text{pore}} \rho(x') e^{ikx'} dx' \rho(x - x_i) e^{-ikx} \quad (2.37)$$

The signal measured is the integration of magnetizations over the whole sample,

$$E(k) = \sum_i e^{ikx_i} \int_{\text{pore}} \rho(x') e^{ikx'} dx' e^{-ikx_i} \int_{\text{pore}} \rho(x) e^{-ikx} dx \quad (2.38)$$

$$= \sum_i \int_{\text{pore}} \rho(x') e^{ikx'} dx' \int_{\text{pore}} \rho(x) e^{-ikx} dx \quad (2.39)$$

The equation shows that the signal is independent of the positions of the pores. The gratings e^{-ikx} only exists within the pores. They are the same regardless of the location of the pores. These gratings can no longer represent the reciprocal space of the whole. Replace k with q , the equation becomes,

$$E(q) = \sum_i \int_{\text{pore}} \rho(x') e^{iqx'} dx' \rho(x) e^{-iqx} dx \quad (2.40)$$

It can be seen that due to the motion average of the grating inside the pores, after the refocusing gradient pulse, the NMR signal is measured with new grating within but no gratings outside the pores. The measurement of this grating clearly corresponded to the size and shape of the pores. The q grating is defined as *gratings that present*

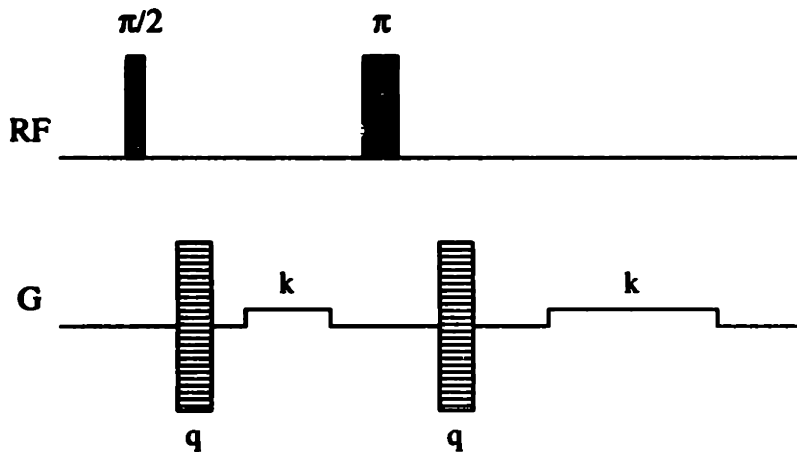


Figure 2-7: PGSE-MASSEY pulse sequence with \mathbf{q} -gradient pulses and \mathbf{k} gradient pulses. The read gradient enables the restoration of spatially dependent phase twist, i.e., the residual \mathbf{k} -grating.

only within the local regions while the overall grating is refocused elsewhere.

2.6.3 Mapping of k and q Space

Pulsed gradient NMR experiments include two main branches, imaging and diffusion measurements. The images are measured in k space. The diffusion are measured in q space, at $k = 0$. The modulus addition using spatially separated echo spectroscopy(MASSEY) technique, see Figure(2-7), by Callaghan[34] is the first work that realizes the existing of two reciprocal spaces. However, MASSEY is introduced only as a technique to avoid artifacts of residual k space components due to gradient pulse mismatch or sample movements. The mapping of the entire reciprocal space of \mathbf{k} and \mathbf{q} can be achieved by deliberately creating a mismatch between the gradient pulses and the measurement at the projected spin echo time is,

$$E(q, k) = \int P(X) e^{ikX} \int_{local} \rho_i(x') e^{iqx'} dx' \int_{local} \rho(x) e^{-iqx} dx dX, \quad (2.41)$$

where $k = \gamma(g_1 - g_2)\delta$ and $q = \gamma g_2 \delta$, with g_1 and g_2 the amplitude of the first and second gradient pulses. The expected $E(q,k)$ is sketched in Figures(2-8) and (2-9).

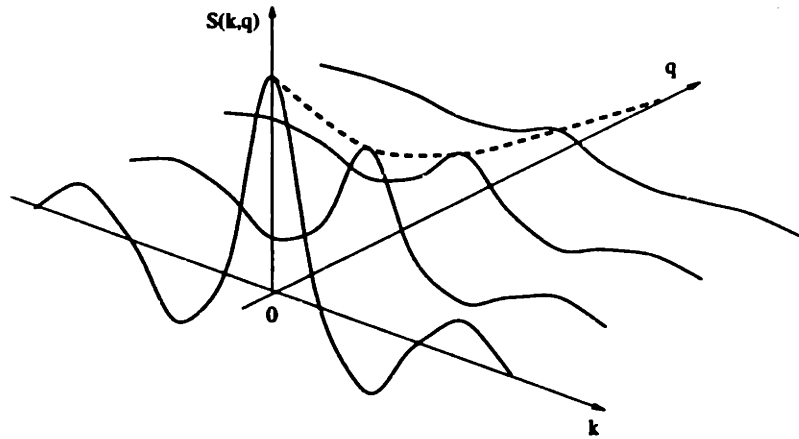


Figure 2-8: Expected space of k and q of NMR experiment. NMR imaging measures the line of $q = 0$, while a PGSE experiment measures the line of $k = 0$.

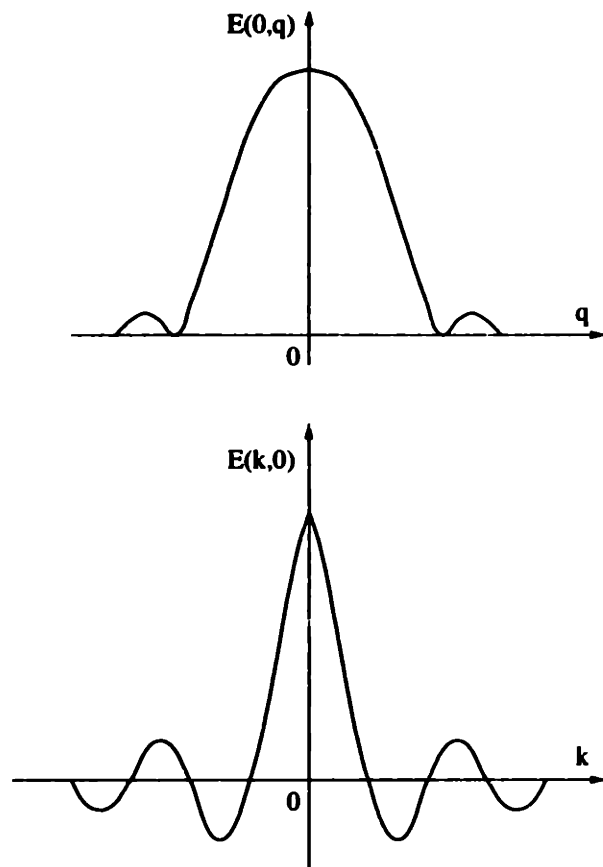


Figure 2-9: Above: A scattering experiment that only measures $E(k, q)$ at $k = 0$; Below: An imaging experiment that only measures $E(k, q)$ at $q = 0$.

2.7 Summary

Spatial NMR measurements are sensitive to the spin density $\rho(\mathbf{r})$ and local displacements specified by $P(\mathbf{r}|\mathbf{r}', t)$ as measured by imaging and scattering experiments, respectively. In truths there is a continuon between these studies sinc both rely on an imposed magnetization grating and are carried out in Fourier space. Scattering measurements ideally will average over the volume of spins and imaging experiments ideally will occur faster than the spins can move. These considerations impose a lower bound on the imaging resolution of about $5\mu\text{m}$ and an upper bound on the scattering measurements of about $100\mu\text{m}$ for water at room temperature.

In NMR scattering, as will be discussed in the next chapter, multiple scattering can be performed very easy. The correlation and convolution relations in double NMR scattering experiments provide us with dynamic information that a single scattering experiment can not. Scattering formulism has come to NMR and provide new ways of interpreting the physics and the results, in return, NMR enhanced the scattering world by contribution of the multiple scattering experiments.

Chapter 3

Multiple Scattering Experiments

3.1 Introduction

A very significant difference between NMR scattering technique and other, say, thermal neutron scattering, experiments is that multiple scattering experiments are easy to perform by NMR. Due to experimental limitations, conventional scattering measurements such as X-ray and neutron scattering, are mostly limited to single scattering events while in the case of NMR scattering, a multiple scattering measurement is not much more difficult than a single scattering as in NMR, the scattering vector \mathbf{q} is easily controlled by the direction, amplitude and duration of the field gradient pulses and the lifetime of the spin magnetization is long. The general idea is to have more than two gradient pulses with the total vectorial sum of the wave vectors associated with the gradient pulses to be zero,

$$\sum_i \mathbf{q}_i = 0. \quad (3.1)$$

For example, a gradient pulse combination is shown in Figure(3-1). Since a π radio frequency(RF) pulse inverts the direction of the wave vectors, they can be added to the experiments to generate a spin echo. In practice, each gradient pulse is sandwiched tightly by two $\frac{\pi}{2}$ RF pulses to minimize the time the magnetization stayed in the transverse plane and to take full advantage of the stimulated echo

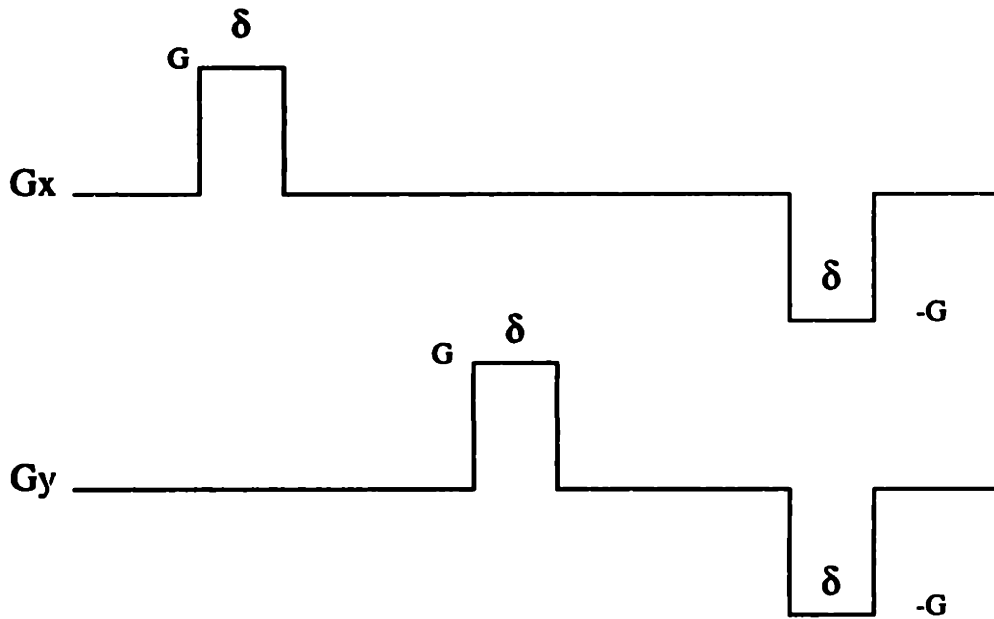


Figure 3-1: A simple gradient pulse combination of an NMR multiple scattering experiment. The gradient pulses are G in amplitude and δ in duration. The wave vectors associated with the gradient pulses are $\mathbf{q}_1 = \gamma G \delta \hat{x}$, $\mathbf{q}_2 = \gamma G \delta \hat{y}$ and $\mathbf{q}_3 = -\gamma G \delta \hat{x} - \gamma G \delta \hat{y}$, respectively. The total vectorial sum of the three are 0.

technique. However, as shown in Figure(3-2), stimulated echo experiments evolve along multiple paths in the reciprocal space. For a single scattering experiment, only one path satisfies the conditions specified in Equation(3.1). For multiple scattering using stimulated echo technique, more than one paths may satisfy Equation(3.1). Thus, the measured signal may be a combination of the signals from different paths of which all but one are undesired. Besides, the final measured signal are not necessarily all due to the excitation of the very first RF pulse. It includes not only signal from the desired multiple scattering event but also all the previous lower order scattering events as each excitation will contribute to the intensity in the the final signal. Proper selection of pathways and a low order scattering filter is needed to remove these artifacts. The use of RF phase cycling and gradient crusher pulses are two simple but effective choices. Please refer to Appendix A for a complete description.

The ability to performing multiple scattering experiments introduces the idea of correlation of length scales in different directions. Since each contribution of such correlation comes from one excitation, the integrated signal are the sum of the corre-

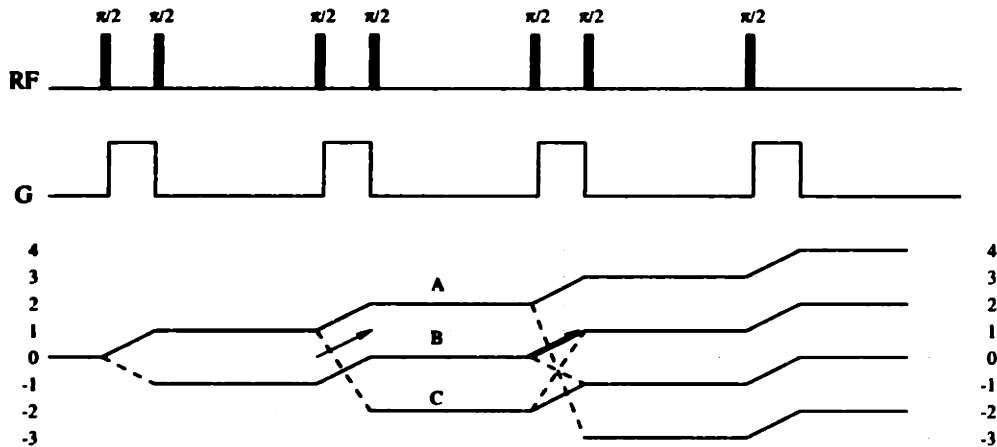


Figure 3-2: NMR multiple scattering experiments are essentially experiments of multiple stimulated echoes. There can be undesired paths that satisfy the condition for multiple scattering experiments, $\sum_i \mathbf{q}_i = 0$ or the ending point of the path is at 0. There are also single scattering events in the mix when the signal comes from the magnetization excited not by the very first but the later RF pulses. The signals from these magnetizations only go thought part of the desired pathway.

lations other than a combination of two separated one dimensional sums. As a first potential application of multiple scattering experiment, measurements of local microscopic anisotropy of glassy samples can be achieved without any need for models.

3.2 Simple Double Scattering Experiments

Although the direction and amplitude of the scattering vectors can be controlled at will in NMR scattering, the most important angles between the two scattering vectors are 0° and 90° . Figure(3-3) shows the pulse sequence of a $2D_{xx}$ experiment which implements two wave vectors along same direction in q space. The two sets of gradient pulses have the same direction, amplitude and duration. If a single spin's dynamics are followed, the positions of the spin are \mathbf{r} , \mathbf{r}' , \mathbf{r}'' and \mathbf{r}''' , respective to the moment when the first, second, third and fourth gradient pulses are applied. The probability densities that connect the four positions are, $P(\mathbf{r}|\mathbf{r}', \Delta)$, $P(\mathbf{r}'|\mathbf{r}'', \Delta'')$ and $P(\mathbf{r}''|\mathbf{r}''', \Delta''')$.

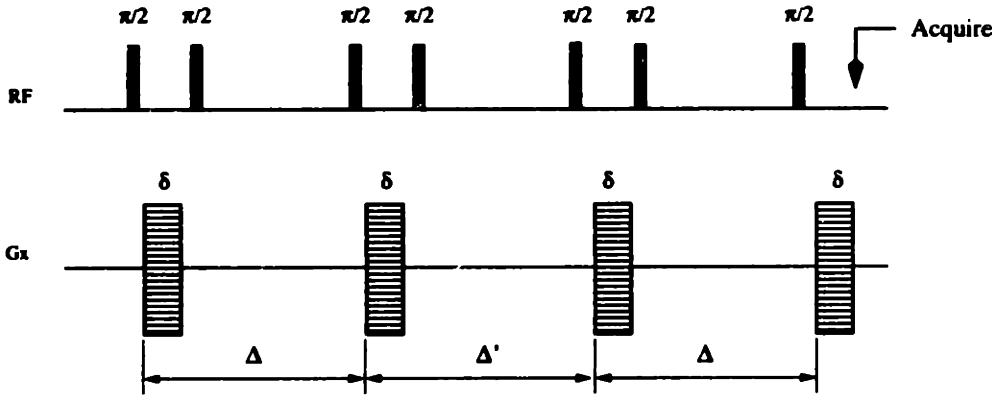


Figure 3-3: A simple double diffusive scattering pulse sequence with the angle between scattering vectors set to 0° . For complete bounded diffusion with long time limit, the measured signal as a function of the amplitude of wave vector q is the average product of the power of a center ray and itself in the three dimensional q space reciprocal to the spin density function of the bounded region—the pore.

The integrate the signals from all such spins, the overall measured signal is,

$$E(q\hat{x}, q\hat{x}) = \int \rho(\mathbf{r}) P(\mathbf{r}|\mathbf{r}', \Delta) P(\mathbf{r}'|\mathbf{r}'', \Delta') P(\mathbf{r}'|\mathbf{r}''', \Delta'') e^{-iq\hat{x}\cdot\mathbf{r}} e^{iq\hat{x}\cdot\mathbf{r}'} e^{-iq\hat{x}\cdot\mathbf{r}''} e^{iq\hat{x}\cdot\mathbf{r}'''} d^3\mathbf{r} d^3\mathbf{r}' d^3\mathbf{r}'' d^3\mathbf{r}''' . \quad (3.2)$$

Figure(3-4) shows the pulse sequence of a $2D_{xy}$ experiment which implements two wave vectors with perpendicular directions in q space. The two sets of gradient pulses have perpendicular directions but the same amplitude and duration. A similar analysis to the above $2D_{xx}$ experiment can be applied. The measured signal for $2D_{xy}$ is,

$$E(q\hat{x}, q\hat{y}) = \int \rho(\mathbf{r}) P(\mathbf{r}|\mathbf{r}', \Delta) P(\mathbf{r}'|\mathbf{r}'', \Delta') P(\mathbf{r}'|\mathbf{r}''', \Delta'') e^{-iq\hat{x}\cdot\mathbf{r}} e^{iq\hat{x}\cdot\mathbf{r}'} e^{-iq\hat{y}\cdot\mathbf{r}''} e^{iq\hat{y}\cdot\mathbf{r}'''} d^3\mathbf{r} d^3\mathbf{r}' d^3\mathbf{r}'' d^3\mathbf{r}''' . \quad (3.3)$$

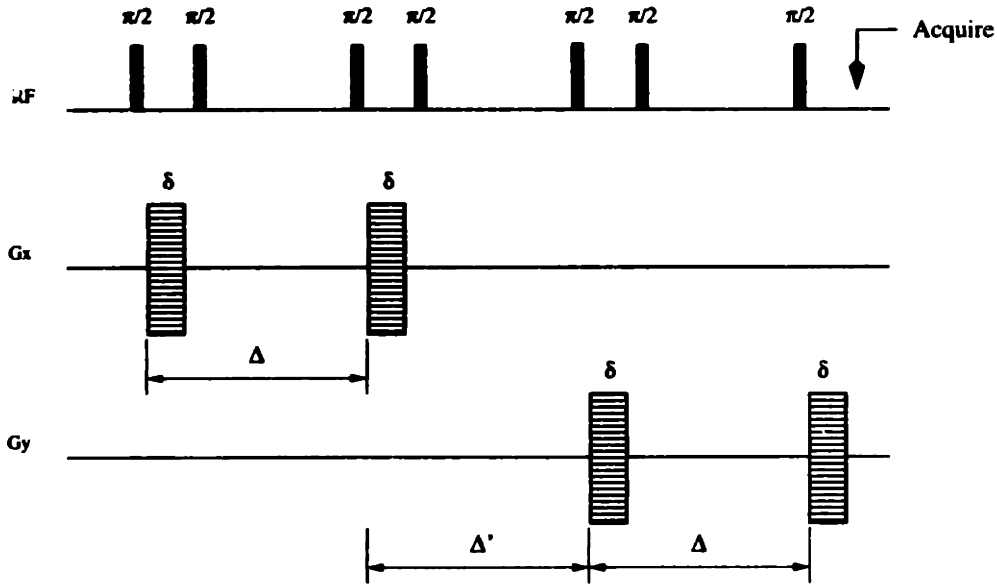


Figure 3-4: Double diffusive scattering pulse sequence with the angle between scattering vectors set to 90° . For complete bounded diffusion with long time limit, the measured signal as a function of the amplitude of wave vector q is the average product of the power of a center ray and a perpendicular ray in the three dimensional q space reciprocal to the spin density function of the bounded region—the pore.

3.3 Double Scattering on Homogeneous Free Diffusion

For homogeneous free diffusion, the probability density is a Gaussian centered at the initial position \mathbf{r} ,

$$P(\mathbf{r}|\mathbf{r}', \Delta) = \frac{1}{(4\pi D\Delta)^{\frac{3}{2}}} e^{-(\mathbf{r}-\mathbf{r}')^2/4D\Delta}, \quad (3.4)$$

where D is the homogeneous self diffusion constant.

For a double scattering on one direction, plugging in the Gaussian for the probability density functions, the signal is,

$$\begin{aligned} E(q\hat{x}, q\hat{x}) &= \int \rho(\mathbf{r}) P(\mathbf{r}|\mathbf{r}', \Delta) e^{iq\hat{x}\cdot(\mathbf{r}'-\mathbf{r})} d^3\mathbf{r} d^3\mathbf{r}' \\ &\times \int P(\mathbf{r}'|\mathbf{r}'', \Delta') P(\mathbf{r}''|\mathbf{r}'', \Delta'') e^{iq\hat{x}\cdot(\mathbf{r}'''-\mathbf{r}'')} d^3\mathbf{r}'' d^3\mathbf{r}''' \\ &= \left[\int \rho(\mathbf{r}) P(\mathbf{r}|\mathbf{r}', \Delta) e^{iq\hat{x}\cdot(\mathbf{r}'-\mathbf{r})} d^3\mathbf{r} d^3\mathbf{r}' \right] e^{-q^2 D \Delta''} \end{aligned}$$

$$= e^{-q^2 D \Delta} e^{-q^2 D \Delta''}.$$

The initial spin density $\rho(\mathbf{r})$ is taken as uniform and normalized over the whole sample region. It can be seen that the signal is independent of the middle mixing time Δ' because during Δ' no magnetization gratings are present and thus the measurement is not sensitive to the displacement of the spins.

For double scattering with two perpendicular directions, the signal is,

$$\begin{aligned} E(q\hat{x}, q\hat{y}) &= \int \rho(\mathbf{r}) P(\mathbf{r}|\mathbf{r}', \Delta) e^{iq\hat{x}\cdot(\mathbf{r}'-\mathbf{r})} d^3\mathbf{r} d^3\mathbf{r}' \\ &\times \int P(\mathbf{r}'|\mathbf{r}'', \Delta') P(\mathbf{r}'|\mathbf{r}'', \Delta'') e^{iq\hat{y}\cdot(\mathbf{r}''-\mathbf{r}'')} d^3\mathbf{r}'' d^3\mathbf{r}''' \\ &= \left[\int \rho(\mathbf{r}) P(\mathbf{r}|\mathbf{r}', \Delta) e^{iq\hat{x}\cdot(\mathbf{r}'-\mathbf{r})} d^3\mathbf{r} d^3\mathbf{r}' \right] e^{-q^2 D \Delta''} \\ &= e^{-q^2 D \Delta} e^{-q^2 D \Delta''}. \end{aligned}$$

If the mixing times are chosen to be the same, i.e., $\Delta'' = \Delta$, both signals may be further simplified to,

$$E(q\hat{x}, q\hat{x}) = e^{-2q^2 D \Delta} \quad (3.5)$$

$$E(q\hat{x}, q\hat{y}) = e^{-2q^2 D \Delta} \quad (3.6)$$

This makes perfect physical sense because even though the measurements correlates the diffusion length scales either along same direction or the perpendicular directions, for homogeneous free diffusion in a sample of infinite spatial extent, the diffusion lengths are the same for all the directions and hence the signals for the two experiments must be the same. It is also worth noting that the results are independent of the middle mixing time Δ' . This is because there is no magnetization grating during Δ' time; therefore, no molecular movements can be detected.

3.4 Double scattering on a bounded compartment

For a pore with spin density function $\rho(\mathbf{r})$, perfect restricting walls, and all the Δ 's satisfying condition $l \lesssim \sqrt{2D\Delta}$, the spin diffusing inside the pore will travel over the whole length of the pore and lose the “memory” of its initial position. The probability densities are only functions of the spin's final positions,

$$\begin{aligned} P(\mathbf{r}|\mathbf{r}', \infty) &= \rho(\mathbf{r}') \\ P(\mathbf{r}'|\mathbf{r}'', \infty) &= \rho(\mathbf{r}'') \\ P(\mathbf{r}''|\mathbf{r}''', \infty) &= \rho(\mathbf{r}'''). \end{aligned}$$

The double scattering signals are then,

$$\begin{aligned} E(q\hat{x}, q\hat{x}) &= \int d^3\mathbf{r}\rho(\mathbf{r})e^{-iq\hat{x}\cdot\mathbf{r}} \int d^3\mathbf{r}'\rho(\mathbf{r}')e^{iq\hat{x}\cdot\mathbf{r}'} \\ &\times \int d^3\mathbf{r}''\rho(\mathbf{r}'')e^{-iq\hat{x}\cdot\mathbf{r}''} \int d^3\mathbf{r}'''\rho(\mathbf{r'''})e^{iq\hat{x}\cdot\mathbf{r'''}} \end{aligned} \quad (3.7)$$

$$\begin{aligned} E(q\hat{x}, q\hat{y}) &= \int d^3\mathbf{r}\rho(\mathbf{r})e^{-iq\hat{x}\cdot\mathbf{r}} \int d^3\mathbf{r}'\rho(\mathbf{r}')e^{iq\hat{x}\cdot\mathbf{r}'} \\ &\times \int d^3\mathbf{r}''\rho(\mathbf{r}'')e^{-iq\hat{y}\cdot\mathbf{r}''} \int d^3\mathbf{r}'''\rho(\mathbf{r'''})e^{iq\hat{y}\cdot\mathbf{r'''}} \end{aligned} \quad (3.8)$$

3.5 Interpretation of the Double Scattering Experiments

There are two ways to interpret the double scattering experiments of restrictive structures, the 2-D correlation functions in real space, and the multiplication of powers of center rays in \mathbf{q} space. The former provides more physical picture while the latter is more easily connected to the measured signal.

3.5.1 2-D Correlation Functions

It can be seen from Equation(3.8) that the q components are zero in the directions that are perpendicular to the applied q vector. The integration along these directions

can be taken separately and yield the projections of the spin density functions along the q vector directions.

$$\rho(x) = \int \rho(x, y, z) dy dz,$$

$$\rho(y) = \int \rho(x, y, z) dx dz.$$

The measured signal is then,

$$E_{xx}(q) = \int dx dx' \rho(x) \rho(x') e^{-iq(x-x')} \int dx'' dx''' \rho(x'') \rho(x''') e^{-iq(x''-x''')} \quad (3.9)$$

$$E_{xy}(q) = \int dx dx' \rho(x) \rho(x') e^{-iq(x-x')} \int dy'' dy''' \rho(y'') \rho(y''') e^{-iq(y''-y''')} \quad (3.10)$$

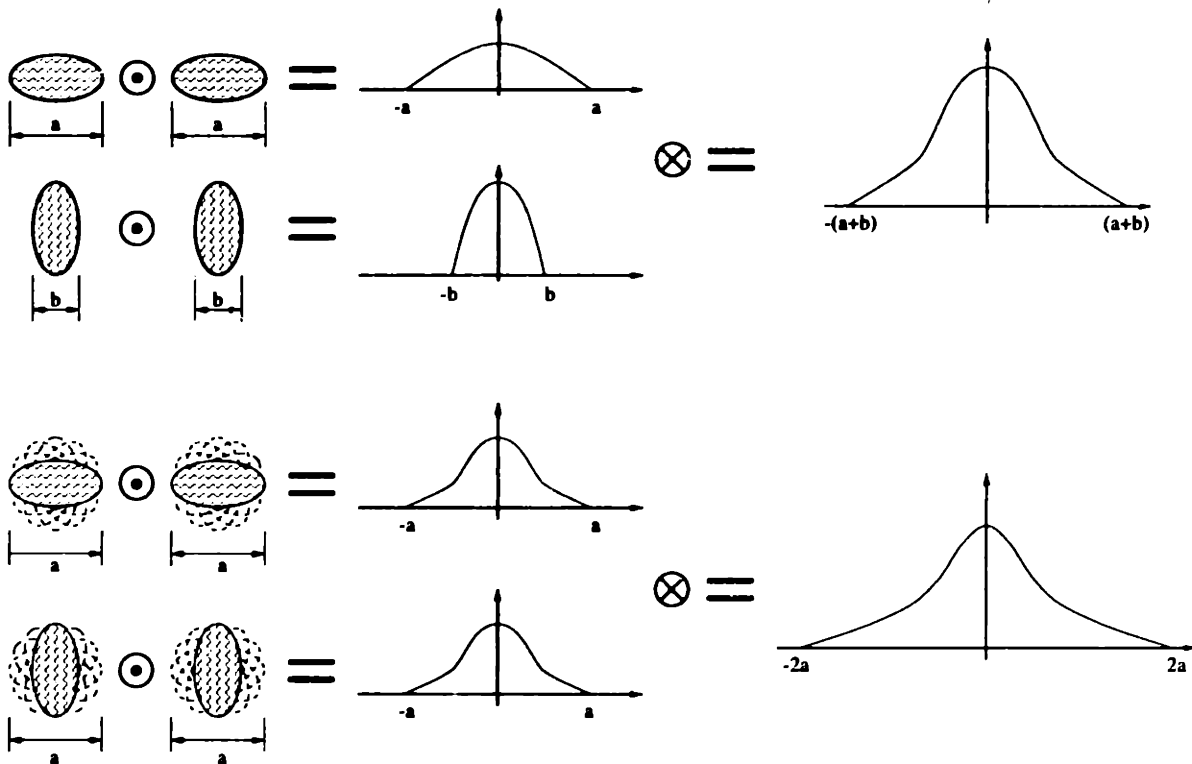


Figure 3-5: The comparison between (a)correlation of profiles along two orthogonal directions within a single pore and (b)no correlations for two individual 1-D experiments along two orthogonal directions on a system of randomly oriented pores which yields the same displacement profile.

To consider all the orientations of the pore, Equations(3.10) must be averaged over all angles, and the total signals are,

$$\overline{S_{xx}(q)} = \frac{1}{4\pi} \int S_{xx}(q) \sin \theta d\theta d\phi, \quad (3.11)$$

$$\overline{S_{xy}(q)} = \frac{1}{4\pi} \int S_{xy}(q) \sin \theta d\theta d\phi. \quad (3.12)$$

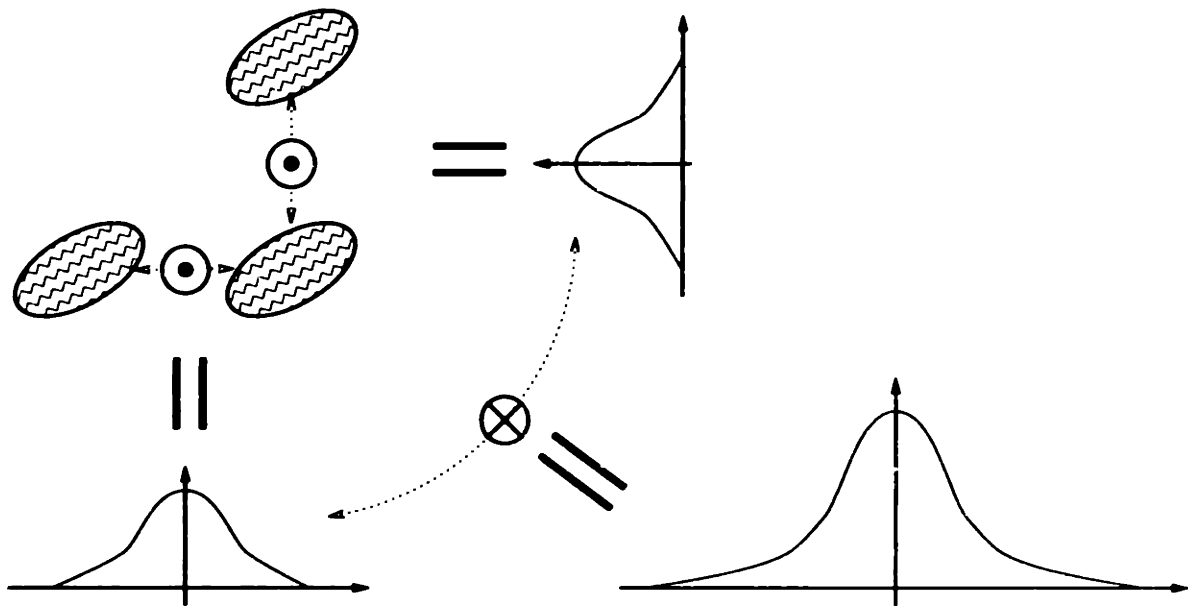


Figure 3-6: A 2-D diffusive scattering performed on an arbitrarily oriented pore. for a system of randomly oriented pores, the result is the sum of the correlations.

The feature of this simple two dimensional correlation function approach is to express a two dimensional problem in a one dimensional formular. Suppose the sample containss randomly oriented ellipsoidal pores with long semi-major radius b and short semi-major radius a . A one dimensional experiment on the system will result in a displacement profile with full width of $2b$. The convolution of the profile with itself will extended the plot to be twice as wide, i.e., a full width of $4b$. But the two dimensional experiment described above will yield a displacement profile with a smaller full width, as within each pore, the movement of a spin along two perpendicular directions are correlated. The profiles obtained by two experiments are compared and information of

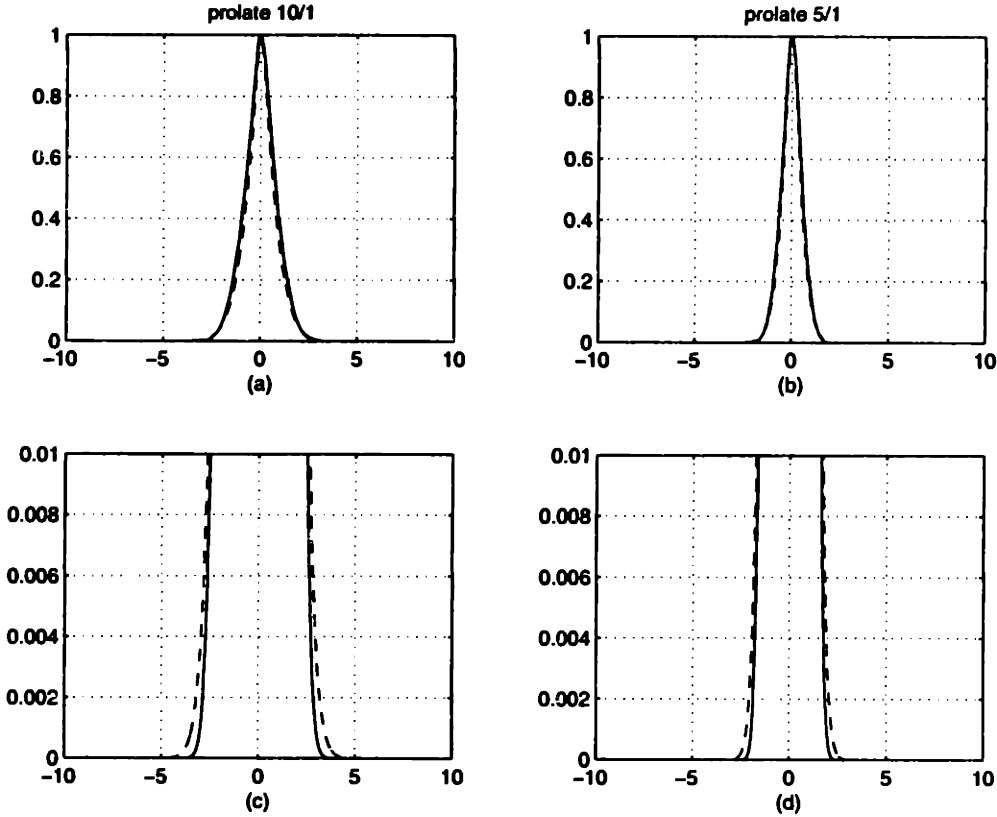


Figure 3-7: Plots of simulated 2-D correlation profiles versus convolutions of 1-D profiles on samples with randomly oriented prolate pores with compress ratio 1/5 and 1/10. The full width of the 2-D determines the average correlated microscopic length scales along two perpendicular directions. The full width of the convolution of 1-D profiles obtained separately determines the largest length scales of the randomly oriented pores. The full width can only be obtained at very low signal intensities.

the pore eccentricity is obtained. The difficulty of this approach is that the accurate determination of the full width of the profile demands high q components, where noise usually dominants the signal, to be measured. Figure(3-7) shows a numerical simulation of a 2-D experiment versus convolution of 1-D experiment of 5/1 and 10/1 prolate samples. It can be seen that the convolution of 1-D data has a full width of 4-fold of the original maximum width as predicted while the 2-D profile has smaller width. It can be suggested that the ratio of the two reveal the eccentricity of the geometry. It is noticed that the difference between the two profiles can not be seen clearly until down to very small scales, typically three or four orders down. The

overall impression of the two profiles are the same. However, as the two dimensional correlation function and its Fourier transform contain the same information, it can be analyzed in the Fourier domain as well.

3.5.2 Structure Factor $|S(\mathbf{q})|^2$ and Power Expansion

For a normalized pore ($V = 1$) with the shape of a rotating ellipse, the 3-D Fourier transform can be given analytically,

$$\S(\mathbf{q}) = \int_V e^{i\mathbf{q} \cdot \mathbf{r}} d^3 \mathbf{r} \quad (3.13)$$

$$= \frac{3 \sin tq - tq \cos tq}{t^3 q^3}, \quad (3.14)$$

with

$$t = \sqrt{a^2 \sin^2 \theta + b^2 \cos^2 \theta}, \quad (3.15)$$

where a and b are the two semi-major radii of the ellipse rotating around the axis where b is lying.

The signal from a double scattering with scattering vectors along same direction is then,

$$E_{xx}(q) = \frac{1}{4\pi} \int |S(\mathbf{q})|^4 \sin \theta d\theta d\phi \quad (3.16)$$

The signal from a double scattering with perpendicular vectors is,

$$E_{xy}(q) = \frac{1}{4\pi} \int |S(\mathbf{q})|^2 |S(\mathbf{q}_\perp)|^2 \sin \theta d\theta d\phi, \quad (3.17)$$

where ϕ is the angle in the plane perpendicular to the first q vector, as seen in Figure(?) and,

$$E(\mathbf{q}_\perp) = \int_V e^{i\mathbf{q}_\perp \cdot \mathbf{r}} d^3 \mathbf{r} \quad (3.18)$$

$$= \frac{3 \sin t_1 q - t_1 q \cos t_1 q}{t_1^3 q^3}, \quad (3.19)$$

with

$$t_1 = \sqrt{a^2 \cos^2 \theta + b^2 \sin^2 \theta \cos^2 \phi}. \quad (3.20)$$

Though the integrations can no be solved analytically, they can be approximated, given small q 's, by expanding $S(\mathbf{q})$ and $S(\mathbf{q}_\perp)$ into Taylor series around $q = 0$, the integrations can then be carried out for each terms analytically. In this way, the scattering signals for $2D_{xx}$ and $2D_{xy}$ are,

$$E_{xx}(q) = 1 + c_2 q^2 + c_4 q^4 + O(q^6) \quad (3.21)$$

$$E_{xy}(q) = 1 + d_2 q^2 + d_4 q^4 + O(q^6), \quad (3.22)$$

where

$$c_2 = d_2 = -\frac{2}{5} \left(\frac{2}{3} a^2 + \frac{1}{3} b^2 \right) \quad (3.23)$$

$$c_4 = \frac{13}{175} \left(\frac{8}{15} a^4 + \frac{4}{15} a^2 b^2 + \frac{1}{5} b^4 \right) \quad (3.24)$$

$$d_4 = \frac{6}{175} \left(\frac{8}{15} a^4 + \frac{4}{15} a^2 b^2 + \frac{1}{5} b^4 \right) + \frac{1}{25} \left(\frac{2}{5} a^4 + \frac{8}{15} a^2 b^2 + \frac{1}{15} b^4 \right). \quad (3.25)$$

It can be seen that the scattering signals for $2D_{xx}$ and $2D_{xy}$ are identical up to the q^2 term. This is because the zeroth order term corresponds to the volume of the ellipsoid and the second order term corresponds to the mean square of the radius of gyration of the ellipsoid. They contains no anisotropic information.

Beginning from the q^4 , the two equations differ. It can be seen that E_{xx} is always larger than E_{xy} which makes sense since $\sum_i A_i^2 \geq \sum_{i \neq j} A_i A_j$, where,

$$A_i = |S_i(q)|^2. \quad (3.26)$$

The difference of the coefficients for the q^4 term in the ellipsoid model is a function of the difference between a^2 and b^2 ,

$$c_4 - d_4 = \frac{2}{375} (a^2 - b^2)^2. \quad (3.27)$$

Therefore, this can be used as an indication of the anisotropic length scales in microscopic structures.

It can be seen that for each curve to the power of q^4 , a and b can be solved uniquely and without the reference to the other curve. This goes back to the original issue of modeling. The calculated values of a and b reflect the averaging over a normally heterogeneous sample. Only in the case of a glass of identical pores may they be directly related to a simple geometry. Without proper presumptions, a and b can not be solved by only one curve as each curve may consist of contributions from different local anisotropies including isotropic dynamic features.

Nevertheless, the goal of the double scattering experiments is to separate the contribution of powder averaged local anisotropy from real size or diffusion coefficient distribution within the sample. The comparison of the two scattering curves of parallel and perpendicular scattering vectors creates a contrast of correlations of same direction and perpendicular directions. The difference in this comparison, which started in the q^4 term as $(d_4 - c_4)$, is a clear indicator of the contribution of eccentricity in the sample.

3.6 Summary

In an NMR scattering experiment, the long lifetime of the spin magnetization coherence (several seconds) and the easy control over the scattering vectors allow multiple dimensional multiple scattering experiments to be performed. The microscopic correlations of scattering along different directions is a unique feature of NMR and has not been accomplished by other scattering methods.

By NMR multiple scattering, local anisotropic features within a glassy sample can be identified from size distributions by the separation of the two double scattering curves, E_{xx} and E_{xy} , at high q region. This information can not be obtained by the one dimensional scattering methods without proper models based on prior knowledge of the system.

Chapter 4

Calculation and Simulation

The theory of how NMR double scattering signal depends on the geometrical features, as described in the previous chapter, can be explicitly expressed, in real space,

$$E_{||}(\eta) = \frac{1}{4\pi} \int [\rho_x(\eta) \odot \rho_x(\eta)] \otimes [\rho_x(\eta) \odot \rho_x(\eta)] d\Omega \quad (4.1)$$

$$E_{\perp}(\eta) = \frac{1}{4\pi} \int [\rho_x(\eta) \odot \rho_x(\eta)] \otimes [\rho_y(\eta) \odot \rho_y(\eta)] d\Omega, \quad (4.2)$$

and in \mathbf{q} space,

$$\tilde{E}_{||}(q) = \int |S(\mathbf{q})|^4 d\Omega \quad (4.3)$$

$$\tilde{E}_{\perp}(q) = \int |S(\mathbf{q})|^2 |S(\mathbf{q}_{\perp})|^2 d\Omega, \quad (4.4)$$

where,

$$S(\mathbf{q}) = \int \rho(\mathbf{r}) e^{-i\mathbf{q} \cdot \mathbf{r}} d^3 \mathbf{r} \quad (4.5)$$

is the Fourier transform of the spin density function $\rho(\mathbf{r})$. These equations are the bases of the calculation and simulation.

4.1 Calculate by Convolution in Real Space

The shape of the pores were approximated by prolate and oblate ellipsoids with uniform spin density. Considering the symmetry, the ellipsoid is anchored with the rotating axis b along z , the advantage is that two angles suffice to describe the orientation of the pore,

$$\rho(x, y, z) = \begin{cases} \frac{1}{V} & \text{if } \frac{x^2}{a^2} + \frac{y^2}{a^2} + \frac{z^2}{b^2} \leq 1 \\ 0 & \text{otherwise} \end{cases} \quad (4.6)$$

where $V = \frac{4}{3}\pi a^2 b$ is the volume.

The cross section across the center of the above ellipsoid normal to y -axis is an ellipse,

$$\frac{x^2}{a^2} + \frac{z^2}{b^2} = 1 \quad (4.7)$$

The eccentricity, e , of an ellipse is defined as the ratio between focal length and the long semi-major axis,

$$e = \begin{cases} \frac{c}{b} & \text{prolate} \\ \frac{c}{a} & \text{oblate,} \end{cases} \quad (4.8)$$

where c is the focal distance which is the distance between the focal points and the center of the ellipse. If the shape is prolate then b is the long semi-major axis on which two focal points are at $c = \sqrt{b^2 - a^2}$ on either side of the origin on z axis. If the shape is oblate then a is the long semi-major axis. The two focal points are at $c = \sqrt{a^2 - b^2}$ on either side of the origin on x axis.

For rotating ellipse, only two Euler angles need to be considered. The new rotating coordinate system can be obtained by multiplying the original coordinate vector by two rotation matrices,

$$\begin{pmatrix} x' \\ y' \\ z' \end{pmatrix} = \begin{pmatrix} 1 & 0 & 0 \\ 0 & \cos \theta & \sin \theta \\ 0 & -\sin \theta & \cos \theta \end{pmatrix} \begin{pmatrix} \cos \psi & \sin \psi & 0 \\ -\sin \psi & \cos \psi & 0 \\ 0 & 0 & 1 \end{pmatrix} \begin{pmatrix} x \\ y \\ z \end{pmatrix} \quad (4.9)$$

The shape functions along x and y axes are obtained by the integration of the

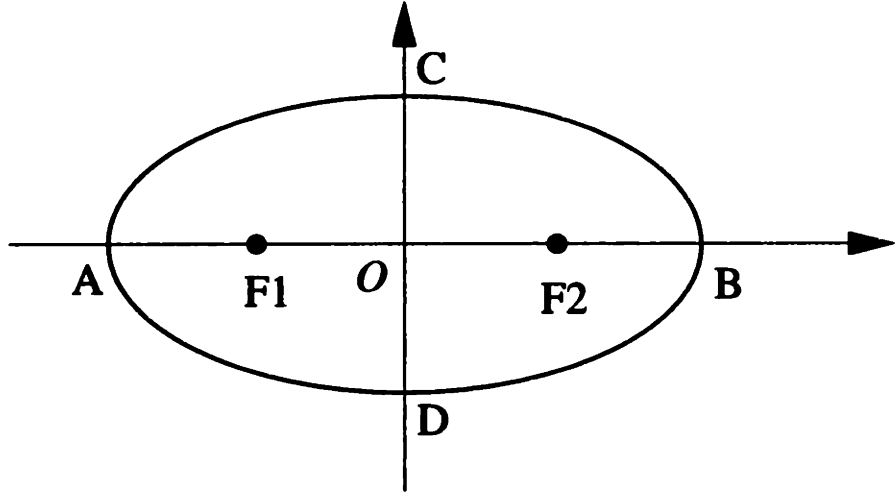


Figure 4-1: Ellipse with long axis $\overline{OA} = \overline{OB} = b$ and short axis $\overline{OC} = \overline{OD} = a$, focus F_1 and F_2 , the eccentricity $e = \sqrt{1 - \frac{a^2}{b^2}}$.

other two orthogonal coordinates,

$$\rho(x) = \int \rho(x, y, z) dy dz \quad (4.10)$$

$$\rho(y) = \int \rho(x, y, z) dx dz \quad (4.11)$$

The spin density $\rho(x, y, z)$ is assumed to be uniform inside the ellipsoid and zero elsewhere. Therefore the projection of the spin density function onto the $x - y$ plane is proportional to the difference of the two roots of second order equation of z ,

$$\rho(x, y) \propto |z_1 - z_2| = \frac{\sqrt{b^2 - 4ac}}{a}, \quad (4.12)$$

where,

$$\left\{ \begin{array}{l} a = \frac{\sin^2 \theta}{a^2} + \frac{\cos^2 \theta}{b^2} \\ b = 2 \left(\frac{1}{a^2} - \frac{1}{b^2} \right) \sin \theta \cos \theta (y \cos \psi - x \sin \psi) \\ c = \frac{x^2 + y^2}{a^2} - \left(\frac{1}{a^2} - \frac{1}{b^2} \right) \sin^2 \theta (y \cos \psi - x \sin \psi)^2 - 1 \end{array} \right. . \quad (4.13)$$

The projection of spin density onto \hat{x} and \hat{y} are obtained by integrating $\rho(x, y)$ over y

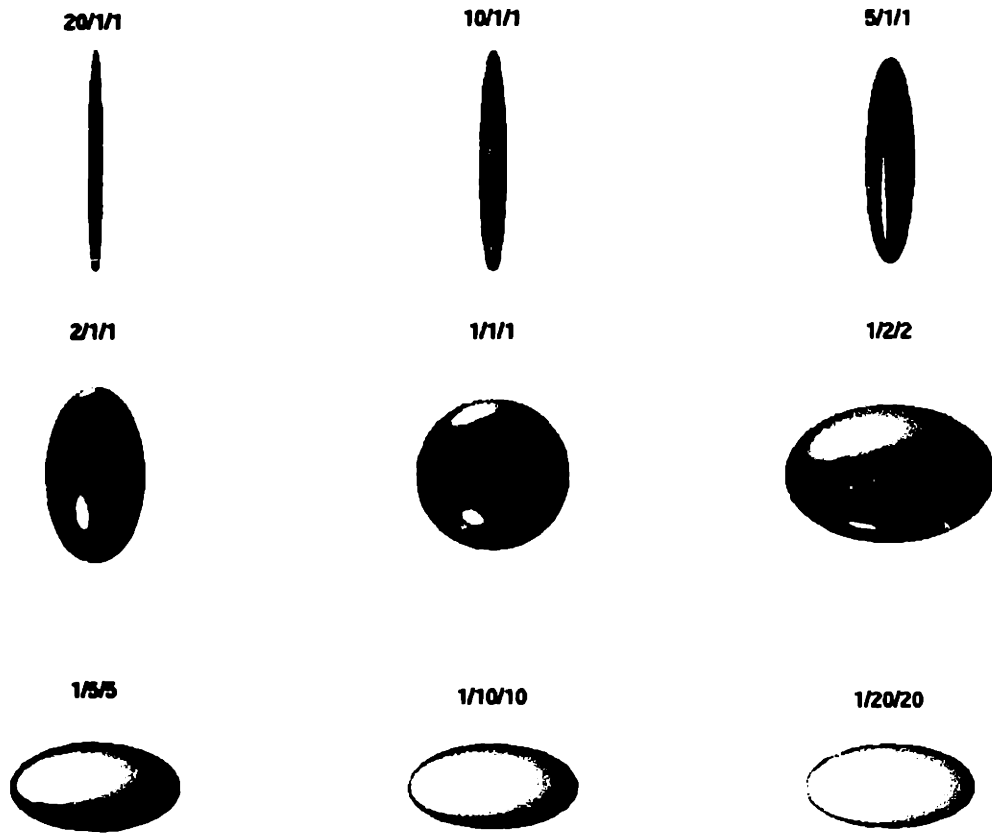


Figure 4-2: Figure shows ellipsoids with varies eccentricities. From prolate, upperleft, to oblate, lower right.

and x , respectively. The calculations are done on a *Silicon Graphics O₂* workstation with 180 MHz *MPS* processor. The Matlab code can be found in Appendix B.

$\rho(x, y)$'s were created as 401×401 matrices with each element calculated as in Equation(4.12) and summed over all θ 's and ψ 's from 0 to $\frac{\pi}{2}$ with 0.5 degree steps. The angular resolution and range is sufficient to cover all possible spin density projections considered the symmetry. Figure(4-2) shows pore shapes used in the calculation and simulation. The eccentricities range from 20/1 prolate to 20/1 oblate. For each shape, the volume are kept the same. The desired a and b are determined from the compress ratio.

Figure(4-3) is the plots of the simulation in real space. The signal in q space can be obtained by the Fourier transformation.

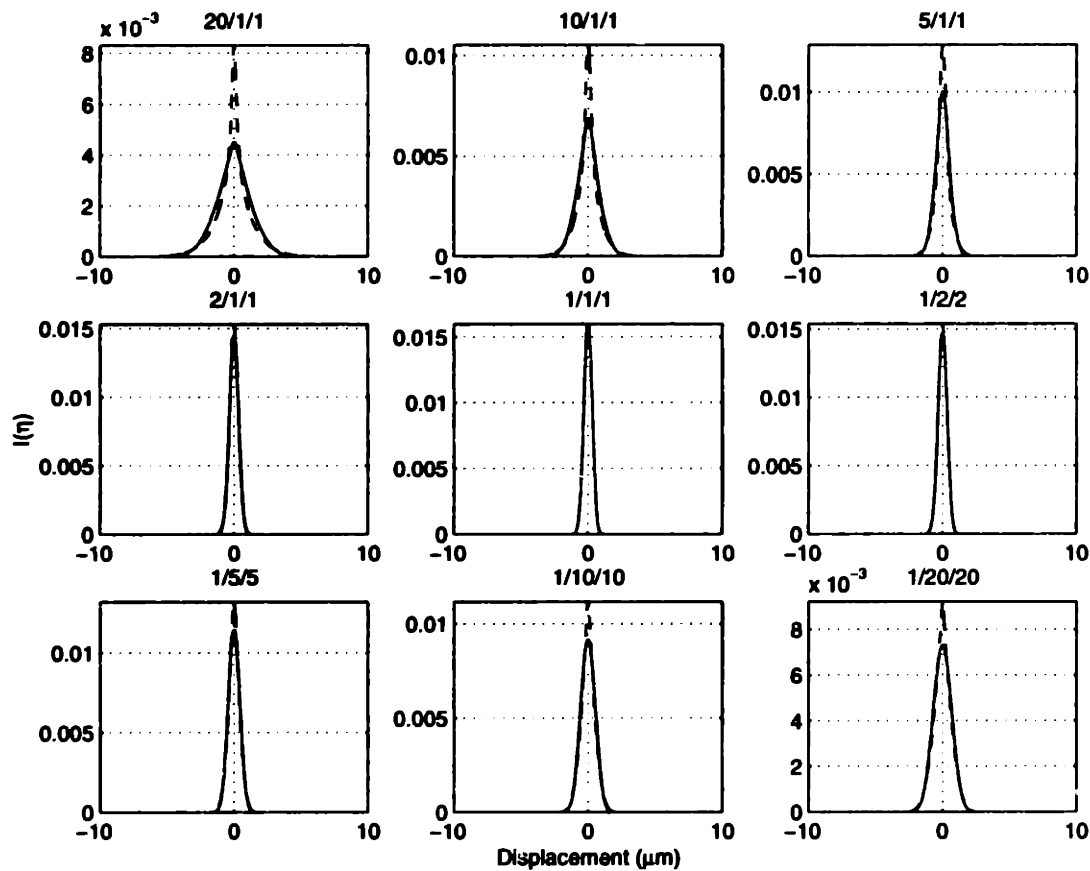


Figure 4-3: Simulation curves for different eccentricities obtained by correlation/convolution method. The volume of the ellipsoids are the same $V = 8\mu\text{m}^3$. The solid lines are results of $2D_{xy}$ and the dashed lines are results of $2D_{xx}$. The full widths are very difficult to see in the plots.

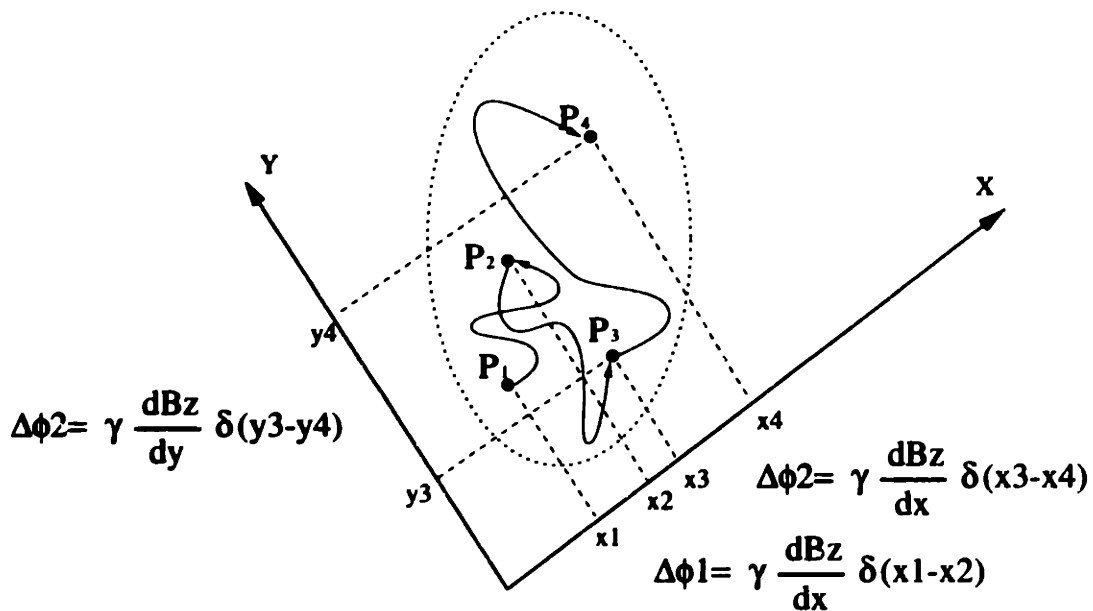


Figure 4-4: Figure shows phase differences of a spin due to displacement between four points, measured by double scattering experiments with parallel or perpendicular scattering vectors.

4.2 Simulation by Monte-Carlo in Q Space

The Monte-Carlo simulation for the multiple scattering experiments assume the long diffusion time limit, i.e., the average r.m.s. of the molecular displacement is greater than the length scale between the restrictive boundaries.

For double scattering, the calculated quantity is the phase changes under magnetic field gradient pulses at four random points within one pore that corresponded to the positions of the molecule at the moments when the gradient pulses are applied. The molecule carrying spin magnetization travels between these points as shown in Figure(4-4).

The phase differences were obtained by first calculating the lengths and directions of the vector that connects the first two points and then the vector that connects the last two points, followed by projecting these two vectors onto a randomly chosen gradient direction to simulate a $2D_{\parallel}$ experiment (or a pair of randomly chosen perpendicular gradient directions to simulate a $2D_{\perp}$ experiment). See Figure(4-4).

For each scattering event, the four positions of the spin are determined by 12

numbers. The gradient directions are determined by two or three numbers. All the numbers can be generated by a random number generator. If the numbers have the accuracy of $\frac{1}{100}$, in order to cover all the possible combinations of the points and directions, one must sample a minimum of 10^{16} scattering events. Additional difficulties are seen at high q values which is the most important region. The signal is low and more accurate calculations are needed.

A direct simulation of the experiment was carried out via Monte-Carlo methods. However, there are difficulties concerning the accuracy when dealing with calculation of the signal at high q values while keeping a reasonable calculation time. The Monte-Carlo code for 2D simulation in C++ is listed in Appendix B.

4.3 Analytical Calculation in Q Space

The three dimensional Fourier transformation of a sphere with radius a , normalized uniform density inside and zero outside is,

$$S(q) = \frac{3}{a^3 q^3} [\sin aq - aq \cos aq]. \quad (4.14)$$

The Fourier transformation of a rotating ellipse along b axis and $b > a$ can be obtained by reconfiguring aq in Equation(4.14),

$$S(\mathbf{q}) = \frac{3V}{q^3 t^3} [\sin qt - qt \cos qt] \quad (4.15)$$

For a perpendicular orientation,

$$S(\mathbf{q}_\perp) = \frac{3V}{q^3 t_1^3} [\sin qt_1 - qt_1 \cos qt_1], \quad (4.16)$$

where,

$$t = \sqrt{a^2 \sin^2 \theta + b^2 \cos^2 \theta} \quad (4.17)$$

$$t_1 = \sqrt{a^2 \cos^2 \theta + b^2 \sin^2 \theta \cos^2 \psi}. \quad (4.18)$$

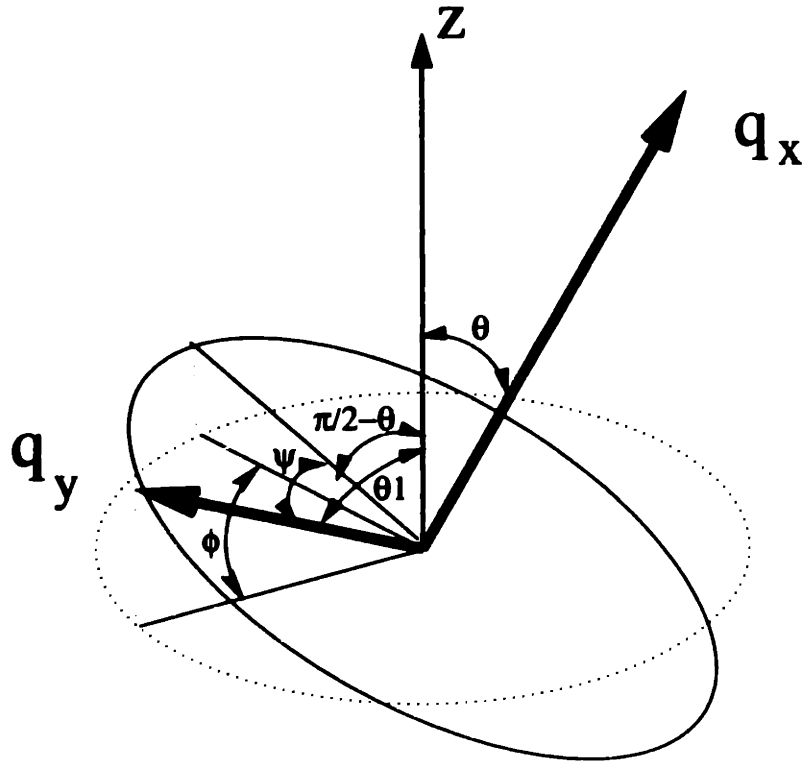


Figure 4-5: The geometric drawing on how to obtain a vector q_y perpendicular to vector q_x . Due to symmetry, only the angle θ_1 , which is the angle between q_y and z , is needed. The relations can be denoted by equation $\cos \theta_1 = \sin \theta \cos \psi$.

The relations between θ , ϕ and ψ are indicated in Figure(4-5). For this particular orientation, the double scattering experiments measure,

$$E(\mathbf{q}) = |S(\mathbf{q})|^4 \quad (4.19)$$

$$E(\mathbf{q}, \mathbf{q}_\perp) = |S(\mathbf{q})|^2 |S(\mathbf{q}_\perp)|^2 \quad (4.20)$$

If the pores are oriented randomly, it is the same as taking different center rays in q space. Averaging over all the possible angles of \mathbf{q} vector,

$$\tilde{E}_{||}(q) = \frac{1}{2} \int |S(\mathbf{q})|^4 \sin \theta d\theta, \quad (4.21)$$

$$\tilde{E}_\perp(q) = \frac{1}{4\pi} \int |S(\mathbf{q})|^2 |S(\mathbf{q}_\perp)|^2 \sin \theta d\theta d\psi. \quad (4.22)$$

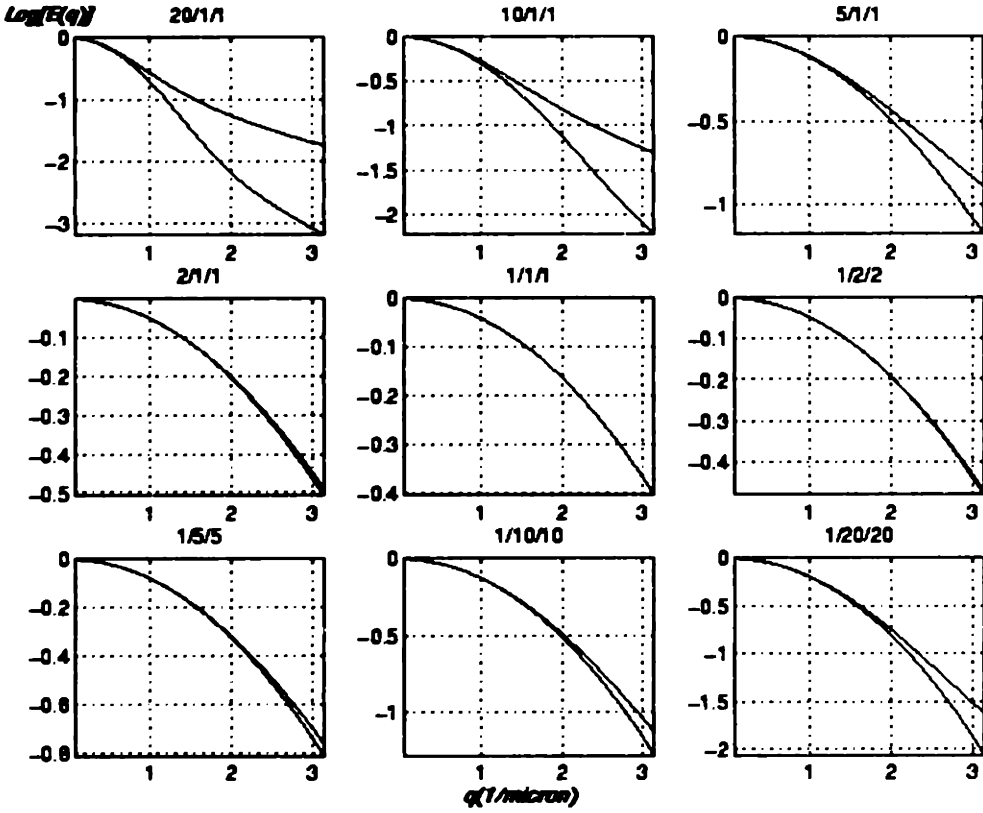


Figure 4-6: Double scattering curves calculated for different eccentricities. Upper curves: $\tilde{E}_{\parallel}(q)$; Lower curves: $\tilde{E}_{\perp}(q)$

The calculated results are shown in Figure(4-6) for different eccentricities of pores. The average was made numerically. The Matlab code is listed in Appendix B.

It can be seen in Figure(4-6) that the separation of the two curves $\tilde{E}_{\parallel}(q)$ and $\tilde{E}_{\perp}(q)$ is a clear indication of ellipsoids' eccentricities.

For small qt and qt_1 , Equation(4.20) can be expanded in a power series,

$$\begin{aligned} \tilde{E}(\mathbf{q}) &= S(0)^4 + 2S(0)^3 S''(0)(qt)^2 \\ &\quad + \frac{1}{6} [9S(0)S''(0)^2 + S(0)^3 S'''''] (qt)^4 + \dots \end{aligned} \quad (4.23)$$

$$\begin{aligned} \tilde{E}(\mathbf{q}, \mathbf{q}_\perp) &= S(0)^4 + 2S(0)^3 S''(0)(qt_1)^2 \\ &\quad + \frac{1}{6} [9S(0)S''(0)^2 + S(0)^3 S'''''] (qt_1)^4 + \dots \end{aligned} \quad (4.24)$$

where the coefficients $S(0)$, $S''(0)$ etc. are,

$$\begin{aligned} S(0) &= 1, \\ S''(0) &= -\frac{1}{5}, \\ S'''(0) &= \frac{3}{35}. \end{aligned}$$

Yielding an analytic expression for the attenuation functions,

$$\tilde{E}(\mathbf{q}) = 1 - \frac{2}{5}(qt)^2 + \frac{13}{175}(qt)^4 + O((qt)^6) \quad (4.25)$$

$$\tilde{E}(\mathbf{q}_\perp) = 1 - \frac{1}{5}[(qt)^2 + (qt_1)^2] + \frac{3}{175}[(qt)^4 + (qt_1)^4] + \frac{1}{25}t^2 t_1^2 q^4 + \dots \quad (4.26)$$

This can be averaged over all angles term by term,

$$\begin{aligned} \overline{t^2} &= \frac{2}{3}a^2 + \frac{1}{3}b^2, \\ \overline{t_1^2} &= \frac{2}{3}a^2 + \frac{1}{3}b^2, \\ \overline{t^4} &= \frac{8}{15}a^4 + \frac{4}{15}a^2 b^2 + \frac{1}{5}b^4, \\ \overline{t_1^4} &= \frac{8}{15}a^4 + \frac{4}{15}a^2 b^2 + \frac{1}{5}b^4, \\ \overline{t^2 t_1^2} &= \frac{2}{5}a^4 + \frac{8}{15}a^2 b^2 + \frac{1}{15}b^4, \end{aligned}$$

so that finally, the expansions of double scattering curves for a normalized pore are,

$$E(q\hat{x}, q\hat{x}) = 1 + c_2 q^2 + c_4 q^4 + \dots \quad (4.27)$$

$$E(q\hat{x}, q\hat{y}) = 1 + d_2 q^2 + d_4 q^4 + \dots \quad (4.28)$$

where,

$$c_2 = d_2 = -\frac{2}{5} \left(\frac{2}{3}a^2 + \frac{1}{3}b^2 \right), \quad (4.29)$$

$$c_4 = \frac{13}{175} \left(\frac{8}{15}a^4 + \frac{4}{15}a^2 b^2 + \frac{1}{5}b^4 \right), \quad (4.30)$$

$$\begin{aligned} d_4 &= \frac{6}{175} \left(\frac{8}{15}a^4 + \frac{4}{15}a^2b^2 + \frac{1}{5}b^4 \right) \\ &\quad + \frac{1}{25} \left(\frac{2}{5}a^4 + \frac{8}{15}a^2b^2 + \frac{1}{15}b^4 \right). \end{aligned} \quad (4.31)$$

The two equations differ from each other only at the quadrupolar term. The difference of the q^4 terms of the two curves is,

$$c_4 - d_4 = \frac{2}{375}(a^2 - b^2)^2. \quad (4.32)$$

From Equation(4.32) and the c_2 and d_2 formula in Equation(4.31), a and b can be solved uniquely.

4.4 Discussion

Although the real space and the reciprocal q space description contain the same information, one picture is usually easier to interpret than the other. For the double scattering case, the parts that contains the most informations are in the low signal regions for both real space and reciprocal space. In real space, the full widths of the profiles are the quantities to measure; in reciprocal q space, it is the degree of separation of the two scattering curves. It is also necessary to separate the contribution of signal of the free water in between the pores. This signal from free water shows up in the scattering curve as a rapid decay in q space. Since the information of the eccentricity are contained in the high q region where the contribution from free water is almost zero, the q space picture is easy to use to separate contributions from water outside and the fluid inside the pores.

However, because the Fourier transform of a sharp peak in q space yields a wide spread of signal in real space, the contribution from the water outside of the pore is difficult to be separated from the signal from the pores. In addition, to determine the cut off of signal in real space requires collecting signals at very high q values. This demands gradient coils that can generate much higher gradient fields.

In the q space, the separation of the scattering curves is seen at modest q levels.

By using the power expansion method described in the previous chapter, the major and minor axes can be calculated by fitting the high q portion of the scattering curve and extrapolating it to arrive at the coefficients of the power series. It should be noted, however, the idea of the double scattering is not to accurately determine the geometry of the pores from the scattering curve. The power of the double scattering is the capability to directly measure the microscopic anisotropic behavior in a glassy sample without any prior knowledge of the sample.

Chapter 5

Experiments

5.1 Instrumentation

The experiments are performed on an Magnex 14 Tesla standard bore super-conducting magnet with Bruker AMXII-600 spectrometer. The probe is home made with a gradient set that can create a field gradient of 1, 250 Gauss/cm(12.5T/m). This gradient set was used to measure the one dimensional scattering curves for the round yeast cells. Unfortunately, due to over enthusiasm, the gradient set was fried. The replacement is less powerful; but nevertheless can give gradient of 1000 Gauss/cm and 600 Gauss/cm in $y - z$ plane at high uniformity. See Figure(5-1).

The high gradient set is compromised by the 600 Gauss/cm set when performing two dimension experiments as the gradient field must be kept the same along two directions.

The linearity of the gradient was tested via diffusion measurements on free water. As can be seen in Figure(5-2), the system shows good dynamic range and linearity.

5.2 Sample Preparation

The best system for testing the new scattering methods are sizable ($4 - 10\mu m$ in diameters), isolated cells or pores filled with water, with easily discernible eccentricities. Yeast cells have been the subject of research in genetics and oncology for many

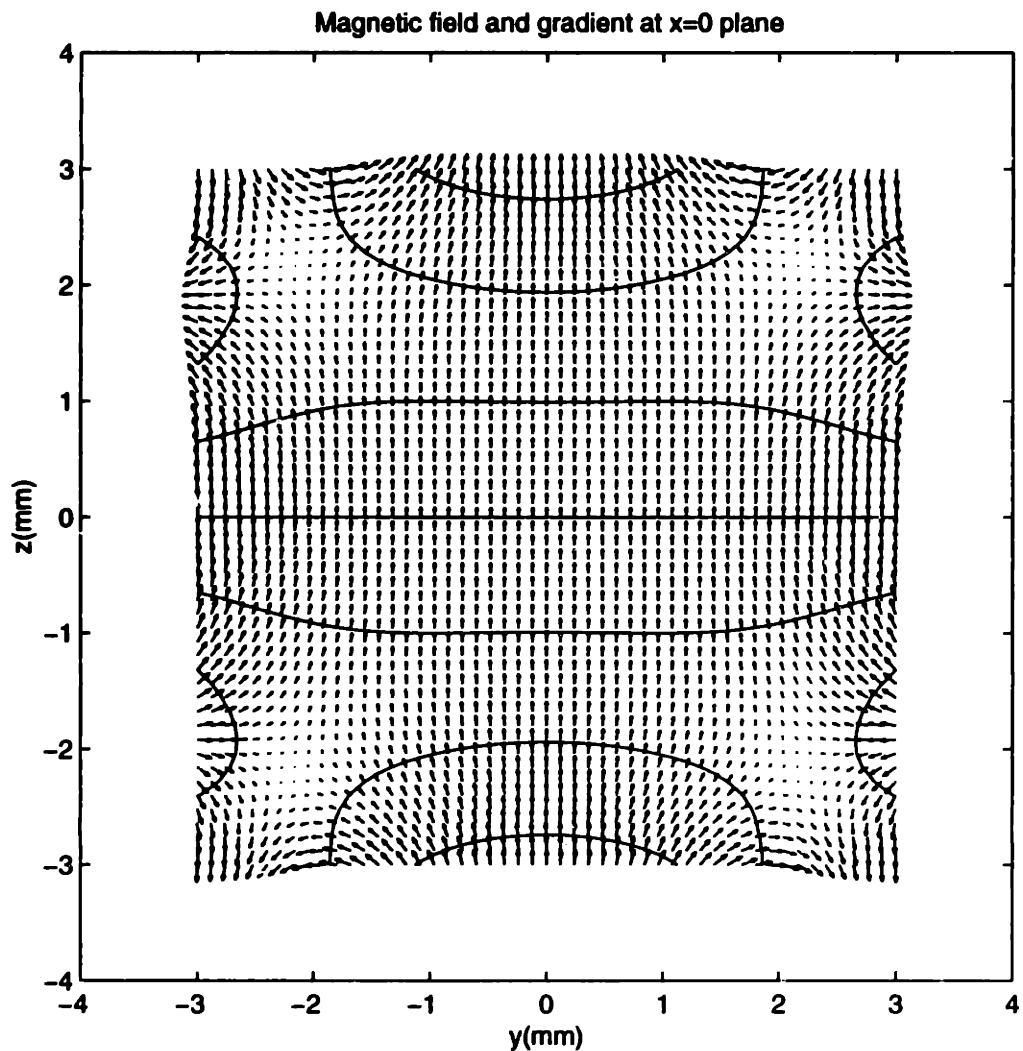


Figure 5-1: Quiver plot of calculate of the $x = 0$ plane of the magnetic field gradient inside the gradient set. High unifomed gradient can be seen within 2 millimeters from the center.

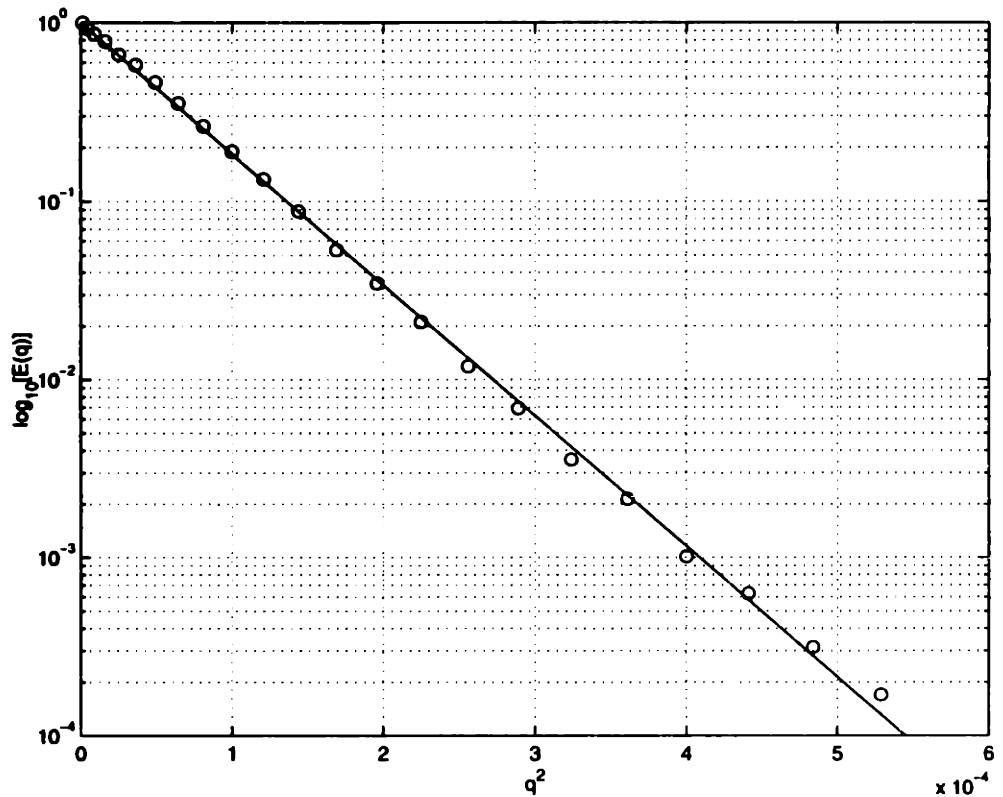


Figure 5-2: semi-logarithm verses second power of gradient pulse amplitudes of diffusion measurement on free water. The straight line extended to very high gradient strength indicates high uniformity of gradient field and high linearity of the system.

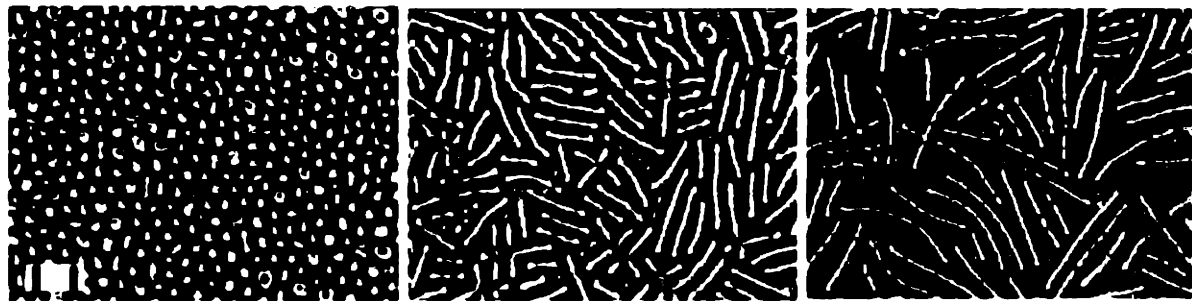


Figure 5-3: Transmitted microscopic pictures of regular(left), medium long(middle) and extra long yeast cells. All three pictures are taken under same amplification. In the lower-left corner, the two tick marks are image of a standard microscopic scale taken under the same condition. The distance between the two ticks is 0.01 mm . From the picture, the average diameter of the normal yeast cells is around $4\mu\text{m}$, the average short semi-major diameters of the two groups of long yeast cells are $4\mu\text{m}$, the average long diameters are $15\mu\text{m}$ and over $20\mu\text{m}$.

years since they are easy to culture and handle. Two types of yeast cells were used in this study, normal yeast cells (which are round and have diameters of about 5 microns), and abnormally long yeast cells provided by the Genetics Lab at Harvard Medical School. After normal yeast cells are treated with mutagenic radiation or chemicals, the DNA inside the nuclei loses its ability to duplicate. As a result, the cells keep growing and never receive signals from the nuclei to divide thus becoming long yeast cells. The length of the cell depends upon the time the treated cells are under culturing condition. The medium long yeast cells are taken out of the media, centrifuged and froze for 5 hours after treatment. The extra long yeast cells are taken out of the media after 12 hours. Figure(5-3) is the images of the three types of yeast cells on slides taken by light microscope. The yeast cells can be kept frozen condition for more than a month without losing their structures.

At the time of the experiment, the yeast cells were thawed and injected into a one-millimeter-diameter capillary. One end of the capillary was melted and sealed prior to introducing the cells. After centrifuging under 2000 RPM for 1 minutes and extra water extracted, the other end of the capillary was sealed by silicone gel to prevent water loss. The sample left was put back into the freezer for later usage.

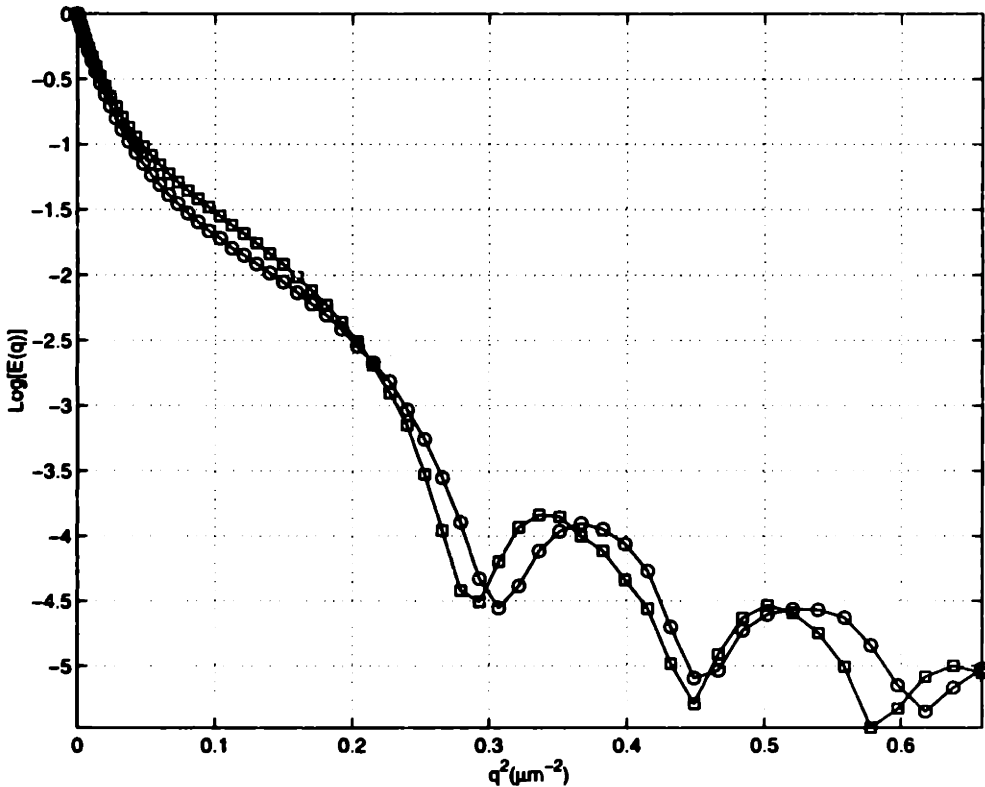


Figure 5-4: One dimensional scattering curves of regular round yeast cells. Both curves taken by pulsed gradient stimulated echo. The maximum gradient strength is 1271 Gauss/cm. Gradient pulse time is 1.5 ms. For open circles, mixing time $\Delta = 27\text{ms}$, for squares, mixing time $\Delta = 17\text{ms}$. The strong oscillation feature of the curves indicates that the cells are round and with narrow size distribution.

5.3 Results and Discussion

One dimensional diffusive scattering experiments were carried out on the normal yeast cells by the pulsed gradient stimulated echo pulse sequence. Phase cycling was used to get rid of the contribution due to the second and third RF pulses and the DC bias of the receiver. 64 gradient steps were used to ramp the gradient pulses from zero to the maximum strength, and 64 averages acquired for each gradient step. The diffusion times Δ are chosen as 17ms and 27ms . The total experiment time for each curve is about 3.4 hours with a duty cycle time (T_r) of 3 seconds.

The results are shown as two curves in Figure(5-4). The average size of the pore can be calculated from the position of the first Fourier peak. The values calculated are

$4.0\mu m$ for $\Delta = 17ms$ and $3.8\mu m$ for $\Delta = 27ms$. The variation of sizes are believed to be caused by dehydration of the yeast cells during the experiments. The experiment for $\Delta = 27ms$ is performed 3.4 hours after the first experiment.

On the medium long yeast cells, two dimensional diffusive scattering experiments were carried out for scattering along same direction and scattering along two perpendicular directions. The pulse sequences for these two experiments were shown in Figure(3-3) and Figure(3-4). Phase cycling discussed in Appendix A was used to filter out the single scattering events and FID's induced by the RF pulses and the DC bias of the receiver. The same number of gradient steps(64) was used to ramp the gradient pulses from zero to the maximum strength. The number of acquisitions was increased to 128 since the signals from double scattering are weaker than that of the single scattering. The diffusion times Δ were chosen as $27ms$. The time delay between the scattering events was $40ms$. The total experiment time for each curve is about 7 hours with a duty cycle time (T_r) of 3 seconds. The double scattering experiments $2D_{||}$ were performed on both directions to avoid mismatches between x and y gradient coil sets.

The double scattering were also performed on the extra long yeast cells under the same conditions and parameters as the experiments on the medium long yeast cells.

The experimental data for the medium long and extra long yeast cells are shown in Figure(5-5) and Figure(5-6), respectively. In both figures, a common part at low q value shows a rapid decrease of signal. This is from diffusion of the free water outside of the yeast cells and contains no other useful information. The curves for $2D_{||}$ and $2D_{\perp}$ experiments overlap at low q region, the separation of the two curves starts at high q . The curves from the scattering of the extra long yeast cells show further separations than the ones for the medium long yeast cells, indicating larger eccentricity in cell shape.

The eccentricities can be directly calculated by solving the equations of the power expansion coefficients. The coefficients were obtained by interpolating the fitted curves of the experimental data, seen as solid lines in the figures.

For the medium and long yeast cells, c_2 are -5.95 and -12.2 , respectively, $c_4 - d_4$

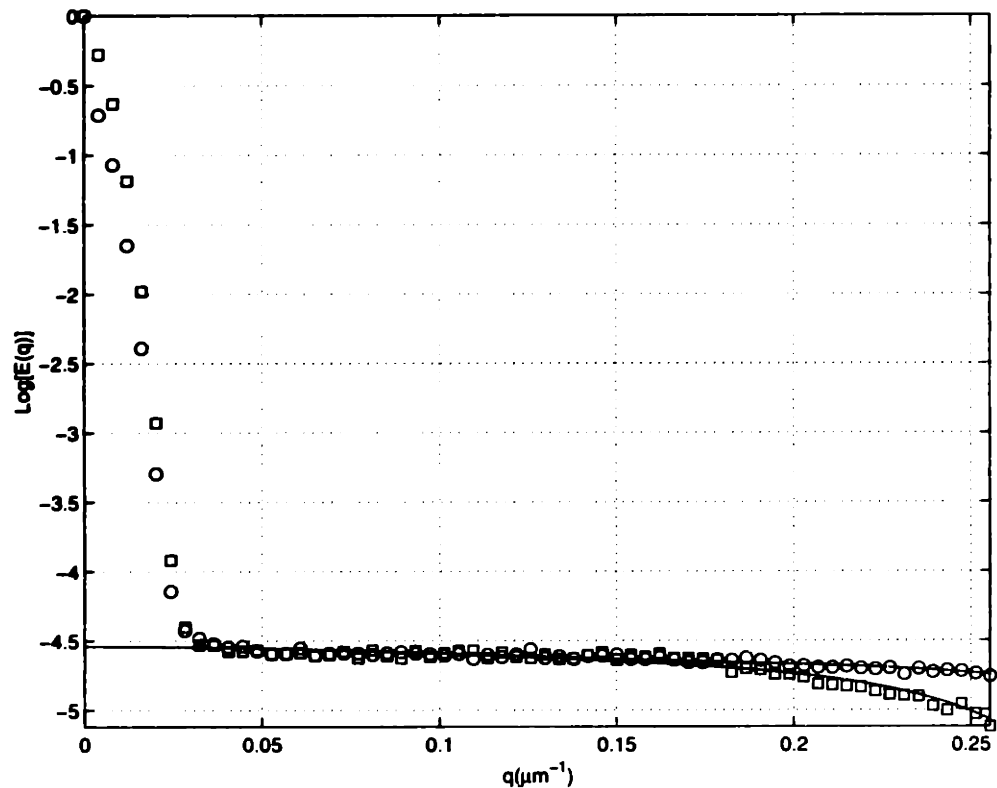


Figure 5-5: 2-D scattering curves from medium long yeast cells. The open circles and squares correspond to scattering of parallel and perpendicular scattering vectors. The solid lines are fitted curves by power expansion up to 6th power. For both data sets: maximum gradient strength is 600 Gauss/cm, gradient pulse length is 1.0 ms. Mixing times are 27 ms. The time interval between two scattering events is 40 ms.

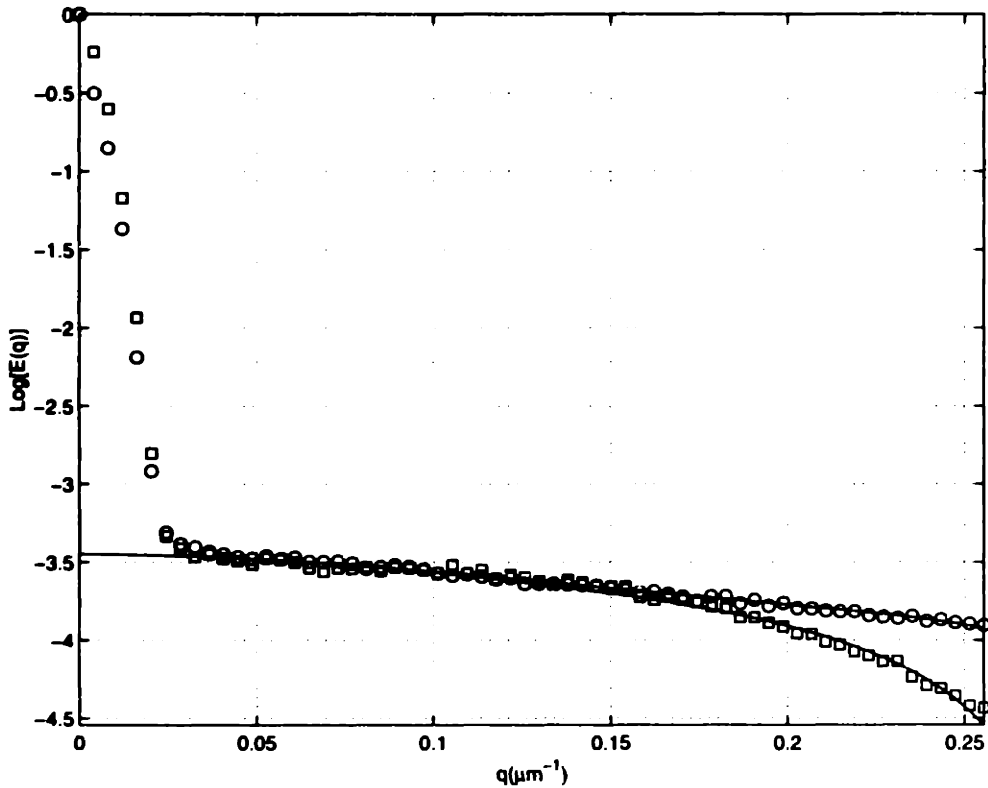


Figure 5-6: 2-D scattering curves from extra long yeast cells. The open circles and squares correspond to scattering of parallel and perpendicular scattering vectors. The solid lines are fitted curves by power expansion up to 6th power. For both data sets: maximum gradient strength is 600 Gauss/cm, gradient pulse length is 1.0 ms. Mixing times are 27 ms. The time interval between two scattering events is 40 ms.

are 9 and 41.3, respectively. The calculated average end-to-end sizes for the two prolate yeast cells are $2.18/2.18/13.0(\mu\text{m})$ and $2.16/2.16/18.88(\mu\text{m})$. The measured sizes are smaller than the actual measurement by the optical microscope. This is partially are result of the diffusion during gradient pulses[47].

The shape of prolate or oblate can be determined by the proper signing of $\sqrt{c_4 - d_4}$ which decide whether a or b is the long semi-major radius. Since the axis system is always chosen to be around b , a smaller b compared to a corresponds to oblate shapes.

The microscopic correlation of scattering directions is a unique feature of NMR scattering and can not be accomplished by other scattering methods such as light, X-ray or neutron scattering. The spatial and temporal region of the NMR scattering is determined by the diffusion coefficients and longitudinal relaxation time. NMR scattering extends these two regions to seconds and the spatial scale to around $100\mu\text{m}$.

Chapter 6

Diffusion in NMR Microscopy

Molecular diffusion in nuclear magnetic resonance imaging can be used as a contrast mechanism. However, in the experiments in search of high spatial resolution, diffusion is arguably the most limiting factor of the ultimate resolution. This is due to the large attenuation of high k components which determine the spatial resolution that can be achieved. It has been stated in the previous chapters that molecular diffusion smears out the magnetization grating which is crucial to an imaging experiment. The finer the magnetization grating is, the more vulnerable it is to the molecular diffusion. The traditional way to treat the diffusion broadening of spectral line in MRI is as a solution of Bloch equations with added diffusion terms[5]. Due to complexities of the boundaries, the problem is usually simplified to the free diffusion case. In large scale($l^2 \gg \Delta x^2$) MRI's where diffusion is regarded as slow motion. This is a good approximation. However, in a scale that boundary effects can not be ignored, it is no longer valid to treat the diffusion as slow motion.

In this chapter, the discussion of diffusion effects in NMR microscopy is focused on the evolution of the magnetization gratings. This approach presents a simple physical picture of the influence of molecular motions and provides a detailed description of the role of molecular diffusion in complex geometry. We intend to show that for a constant time imaging experiment, the signal loss, or equivalently the point spread function, is significantly less than that predicted by the familiar Bloch-Torrey equation-a perfect analysis in many cases[52] but not a suitable model for microscopic imaging. We

will then use this to argue that the limitation of spatial resolution in high field, high gradient NMR microscopy is neither the molecular diffusion nor the low gradient field but primarily the low sensitivity of the measurement.

6.1 Background

The goal of magnetic resonance imaging is to map out the spin density in space. In MRI the image is taken by collecting components in the reciprocal k -space and reconstructed by Fourier transformation. However, at any given moment, NMR can only measure one component of the k -space (at $\mathbf{k} = 0$), of the measured object because in NMR the signal is integrated over the whole sample. In order to measure the $\mathbf{k} \neq 0$ components, the whole k -space must be shifted by applying magnetic field gradients and magnetization gratings are created across the sample. By superimposing a magnetization grating, the measured signal becomes vulnerable to any molecular motions.

The influence of molecular motions on any magnetization grating can be directly described by introducing the conditional probability density of spin or molecular displacement, $P(\mathbf{r}|\mathbf{r}', t)$, the probability density that a spin initial at \mathbf{r} will be at \mathbf{r}' at a time t . We will use this probability density function and the development of magnetization gratings in the sample to describe the influence of molecular diffusion in imaging.

Since the probability density of molecular displacement is not necessarily isoplanar, we can not describe the changes of the grating by a simple convolution approach, a.k.a. the point-spread-function theory, instead, a general integral form of equation must be used.

The instantaneous variation of the grating that is accompanied by the molecular motion is most easily expressed as an integral of the grating's phase that is accumulated at a point by the motions of the molecules.

$$\text{grating} = \rho_s \int P_s(z'|z, dt) \exp(-ik_i z') dz' \quad (6.1)$$

6.2 Molecular diffusion in a sample of finite extent

The well-known attenuation behavior of molecular diffusion in a grating is associated with a uniform sample of infinite extent. The normalized probability of molecular displacement is Gaussian,

$$P_d(z|z', t) = \frac{1}{\sqrt{2\pi}\sigma} \exp\left[-\frac{(x' - x)^2}{2\sigma^2}\right] \quad (6.2)$$

with a standard deviation of

$$\sigma = \sqrt{2Dt} \quad (6.3)$$

where D is the molecular diffusion constant. The value of the standard deviation depends on the dimensions over which diffusion is monitored. Even though the sample is three-dimensional, the grating will break the symmetry and only motions along the grating will lead to observable changes. Therefore, the 1-D standard deviation is appropriate in this analysis.

Notice that P_d is described as being spatially invariant so that this description of the problem is only consistent with a sample of infinite spatial extent in which only one \mathbf{k} component exists and therefore the attenuation occurs only when you shift the $\mathbf{k} = 0$ component to a higher value and back like in an gradient echo experiment. For any object with finite spatial extent, the attenuation of each \mathbf{k} component is dependent of it's k -space trajectory. We can not evaluate the attenuation the same way as the free diffusion case because in free diffusion case there is no $\mathbf{k} \neq 0$ component exist.

6.3 Calculations

The calculation is based on the impulse propagator method developed by Caprihan, Wang and Fukushima[53]. The gradient is divided into N narrow impulses and a narrow pulse approximation is assumed for each pulse. It is easily seen that after one

gradient pulse and a time of delay, the spin system will be,

$$\rho_s(\mathbf{r}, n + 1) = \int d^3\mathbf{r}' P_s(\mathbf{r}'|\mathbf{r}, \delta) \rho_s(\mathbf{r}', n) \exp(-i\mathbf{k} \cdot \mathbf{r}'), \quad (6.4)$$

where $\mathbf{k} = \gamma\mathbf{g}\delta$, and δ is length of each gradient impulse and the time interval between the starting point of consequent impulses. Knowing that,

$$\rho_s(\mathbf{r}, 0) = \rho(\mathbf{r}), \quad (6.5)$$

the signal after each impulse can be calculated as,

$$S(n) = \int d^3\mathbf{r} \rho_s(\mathbf{r}, n). \quad (6.6)$$

For simple geometries, such as parallel-planes, cylinders and spheres, $P_s(\mathbf{r}|\mathbf{r}', \delta)$ are known:

(1) For parallel planes separated by $2a$,

$$\begin{aligned} P(z|z', \delta) &= \frac{1}{a} \sum_{n=0}^{\infty} \exp\left[-\frac{n^2\pi^2 D\delta}{a^2}\right] \cos \frac{n\pi z}{a} \cos \frac{n\pi z'}{a} + \\ &\quad \frac{1}{a} \sum_{n=0}^{\infty} \exp\left[-\frac{(n+\frac{1}{2})^2\pi^2 D\delta}{a^2}\right] \sin \frac{(n+\frac{1}{2})\pi z}{a} \sin \frac{(n+\frac{1}{2})\pi z'}{a}. \end{aligned} \quad (6.7)$$

(2) For cylinders with radius a ,

$$P(\mathbf{r}|\mathbf{r}', \delta) = \sum_{nk}^{\infty} \exp\left[-\frac{\beta_{nk}^2 D\delta}{a^2}\right] J_n\left(\frac{\beta_{nk} r}{a}\right) J_n\left(\frac{\beta_{nk} r'}{a}\right) A_{nk}^2 \cos(n\theta) \cos(n\theta') \quad (6.8)$$

where

$$A_{nk}^2 = \begin{cases} \frac{1}{\pi a^2 J_n^2(\beta_{nk})} & \text{if } n = 0 \\ \frac{2\beta_{nk}^2}{\pi a^2 J_n^2(\beta_{nk})(\beta_{nk}^2 - n^2)} & \text{if } n \neq 0. \end{cases} \quad (6.9)$$

The J_n are cylindrical Bessel functions and β_{nk} are determined by,

$$\beta_{nk} \frac{J'_n(\beta_{nk})}{J_n(\beta_{nk})} = 0 \quad (6.10)$$

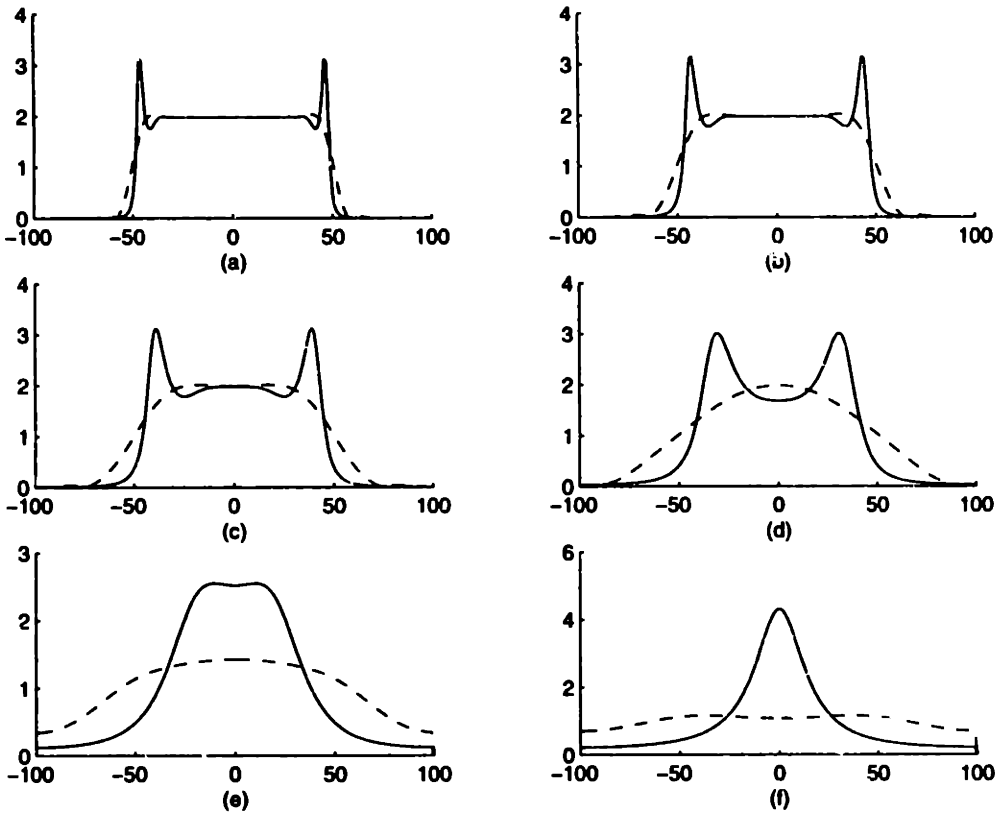


Figure 6-1: Comparison of two simulation methods. Dashed lines represent free diffusion approach using Bloch-Torry equations. Solid lines represent calculation using conditional probability density function. (a) $\delta = 1ms$, (b) $\delta = 5ms$, (c) $\delta = 20ms$, (d) $\delta = 100ms$, (e) $\delta = 500ms$, (f) $\delta = 2000ms$

6.4 Experiments and Discussion

The experiments were carried out on a Bruker AMX 600 spectrometer with home build probe for micro imaging. The probe has a high efficiency three dimensional gradient coil that generates gradients up to 1000 Gauss/cm in-plane. The rf coil size can accommodate 1mm capillary tube cut to about 1.5 cm long.

The sample is a Teflon capillary tubes with inner diameter of 100 microns and outer diameter of 200 microns. The tube was filled with water by a syringe and then cut in to a 1 centimeter long section and inserted and sealed into a 1 mm sample tube.

Two one dimensional constant time imaging experiments were performed with

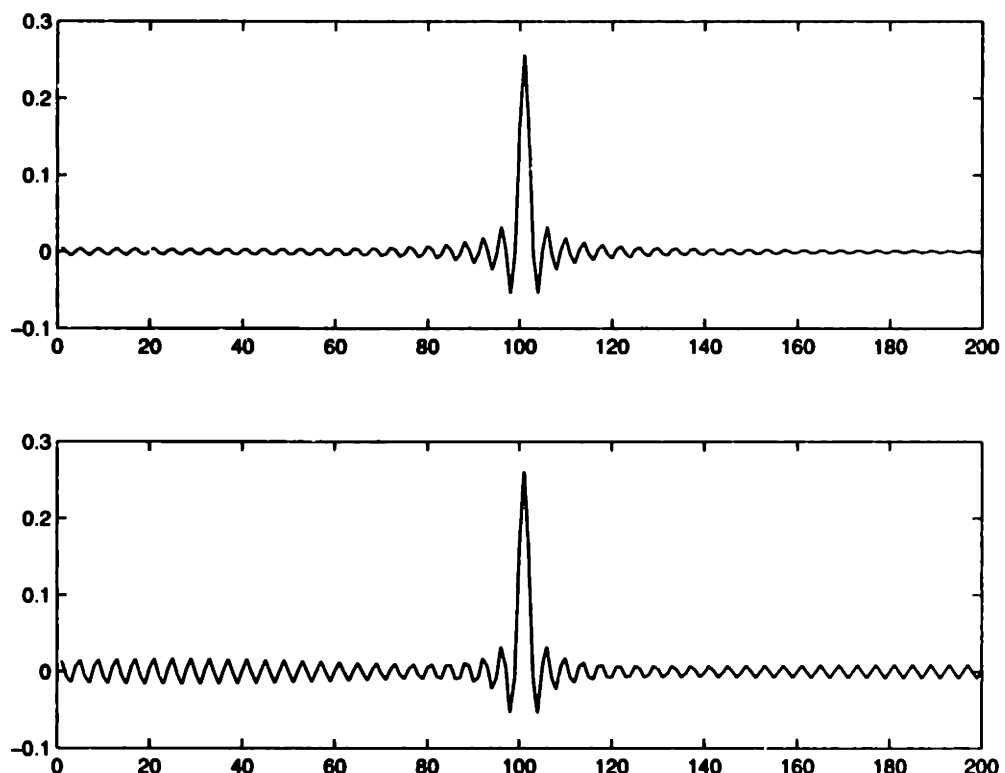


Figure 6-2: A gradient echo of a sample of a top-hat cell calculated using free diffusion approximation (top) and conditional probability density function. $\delta = 0.02\text{ms}$

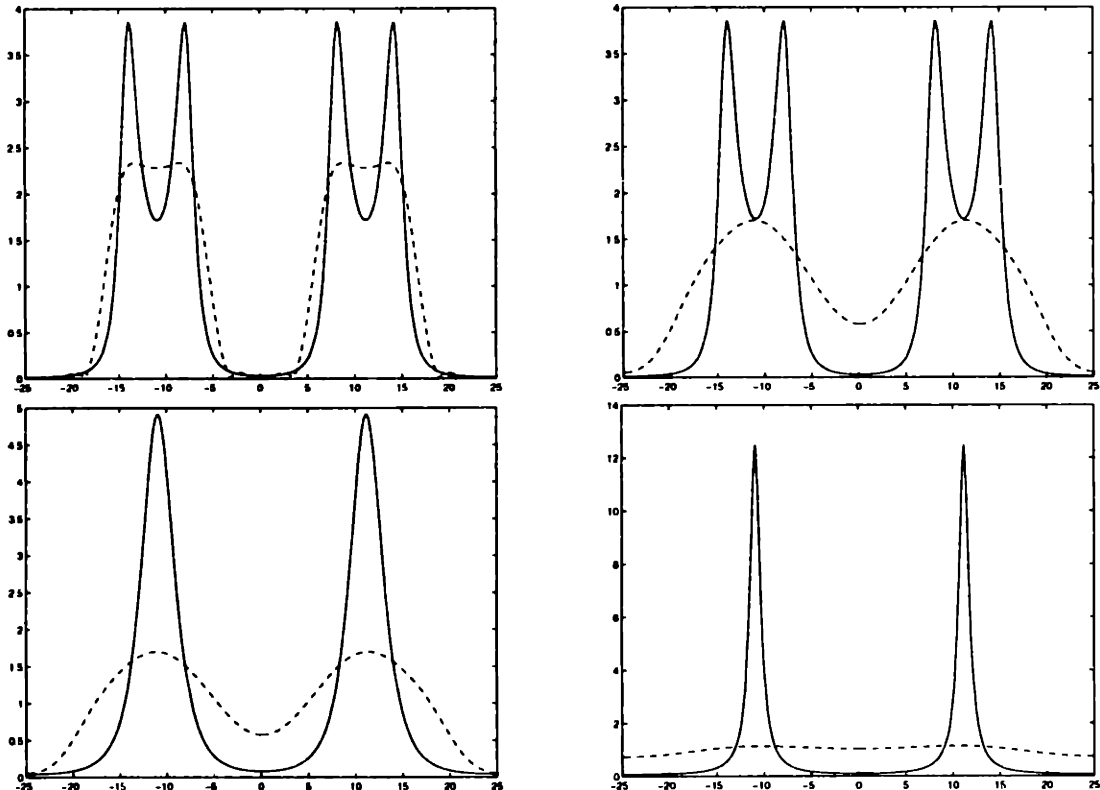


Figure 6-3: The 1-D images of double top-hat cells calculated assuming free diffusion(dashed lines) and using conditional probability density function. Upper left: $\delta = 0.1ms$; Upper right: $\delta = 1ms$; Lower left: $\delta = 4ms$; Lower right: $\delta = 108ms$;

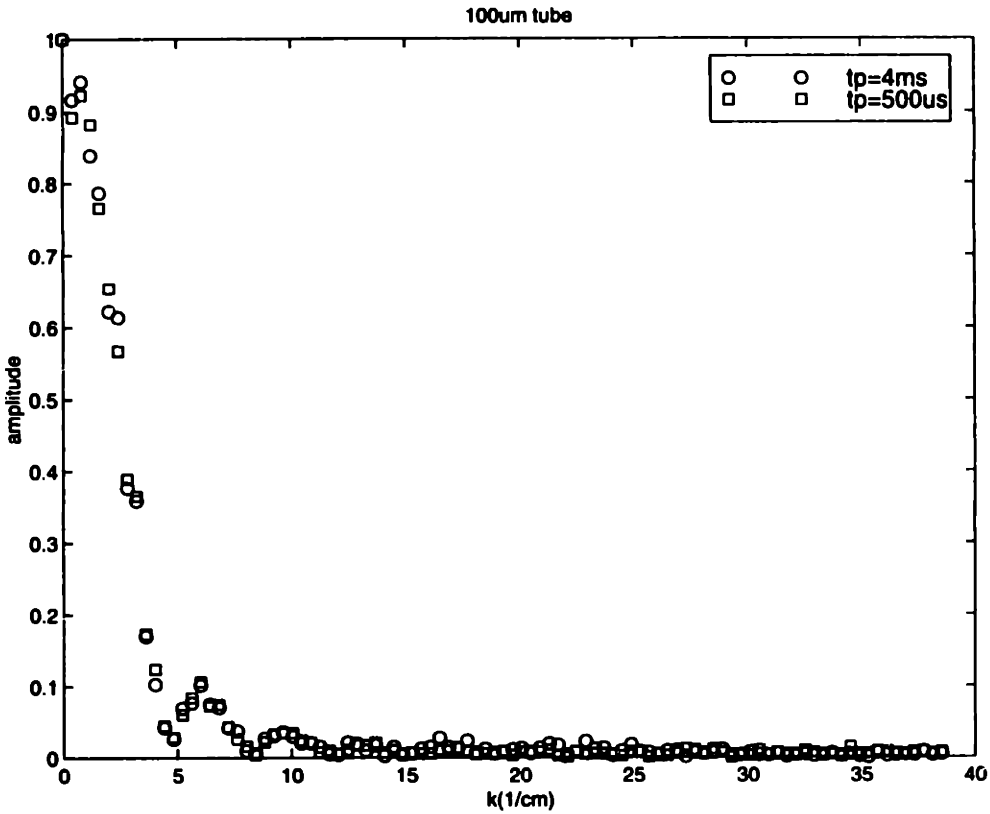


Figure 6-4: Amplitude of CTI signal of a 100 micron I.D. capillary tube. The amplitudes of the open circles($tp=4\text{ms}$) didn't fall below the squares($tm=0.5\text{ms}$), even at the fourth and the fifth lobes, indicating no significant diffusion loss.

the same field of view $FOV = 1.65\text{mm}$ and resolution $16.5\mu\text{m}$. The gradient pulse lengths were 500 microseconds and 4000 microseconds in length.

Figure(6-4) shows the results of the amplitude of the CTI experiments. It can be seen that for a gradient strength 8 times lower, there is no signs of severe diffusion attenuation in the signal compare with the signal with 8 times stronger but 8 times narrower gradient pulses. The ultimate spatial resolution for CTI or back-projection experiments can be much higher than predicted by the Bloch-Torry equation. The dominant factor in microscopic imaging for fine structures is the sensitivity of the instrumentation and experimental schemes.

Appendix A

Choosing Only the Desired Signal for 2-D Scattering Experiments

There are totally seven $\frac{\pi}{2}$ RF pulses in the two dimensional scattering experiment pulse sequence. Each one of there will tip some “new” magnetization in to the transverse plane and will affect the final signal in the forms of free induction decay(FID), spin echoes or stimulated echoes. Crusher gradient pulses are used to dephase all transverse magnetization during the mixing or diffusion time intervals(delay time between 2nd and 3rd, 4th and 5th, 6th and 7th RF pulses). This leaves only the stimulated echoes to be concerned about.

A.1 Filtering of Single Scattering Events

Other than the stimulated echo initialed by the very first RF pulse, stimulated echoes, at the same time point, can be caused from the tip-downed new magnetization by the third and the fifth RF pulses. The phase cycling listed in Table(A.1) helps to remove these stimulated echoes and all the FID's by the sixth and the seventh RF pulses. This leaves only the signal from the multiple scattering events.

RF	RF1	RF2	RF3	RF4	RF5	RF6	RF7	ACQ
Tip Angle	$\frac{\pi}{2}$	NA						
1	0	0	2	2	0	2	2	0
2	2	0	2	0	0	0	0	0
3	0	2	0	2	2	2	2	2
4	2	2	0	0	2	0	0	2
5	2	0	2	2	0	2	2	2
6	0	0	2	0	0	0	0	2
7	2	2	0	2	2	2	2	0
8	0	2	0	0	2	0	0	0
9	2	0	0	2	0	2	2	0
10	0	0	0	0	0	0	0	0
11	2	2	2	2	2	2	2	2
12	0	2	2	0	2	0	0	2
13	0	0	0	2	0	2	2	2
14	2	0	0	0	0	0	0	2
15	0	2	2	2	2	2	2	0
16	2	2	2	0	2	0	0	0

Table A.1: Phase Cycle for 2-D Scattering. All signals from single scattering events are filtered out. For $2D_{xx}$ and $2D_{yy}$ experiments, three k pathway is allowed. CY-CLOP can be implemented on top of this phase cycling.

A.2 Selection of k Pathways

During the middle mixing time, k should be zero so that the first and the second scattering events can be treated independent. The unwanted paths are the path A and path C shown in Figure(A-1). To kill these two paths, consider the phase cycle listed in Table(A.2).

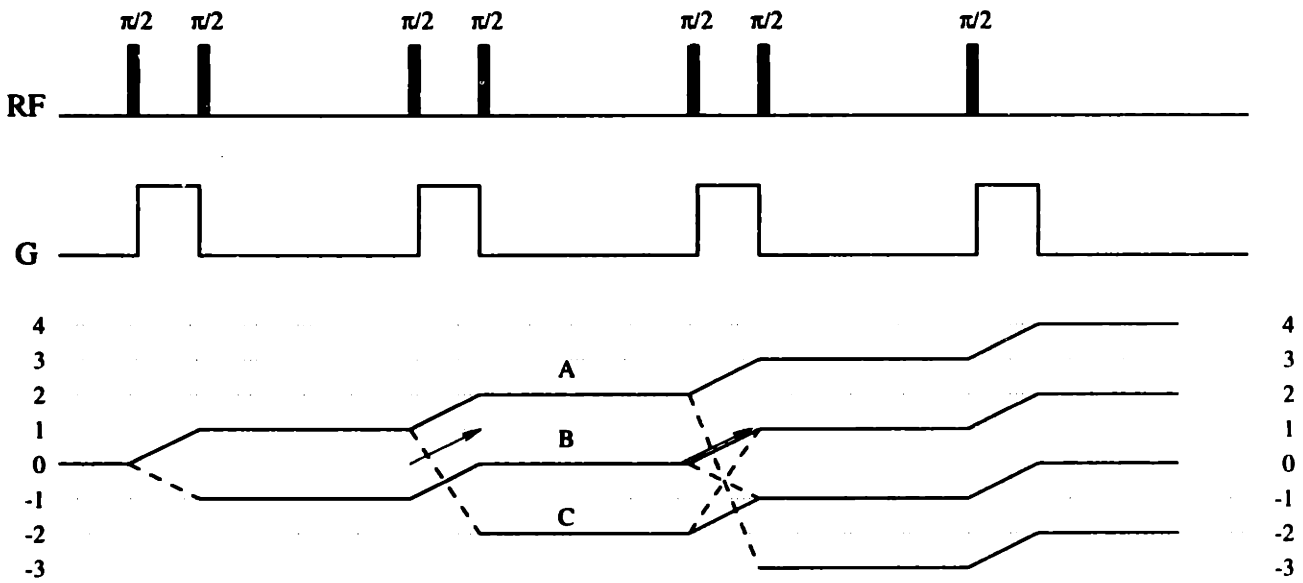


Figure A-1: Because a $\frac{\pi}{2}$ RF pulse will cause the mixing of $+k$ and $-k$ paths, there are additional pathways that can contribute to the final stimulated echo.

The signal from each scan in the phase cycle are summarized as following: 1. ADC phase +:

$$\begin{aligned}
 I_z &\xrightarrow{x} +I_y \\
 &\rightarrow +I_y \cos kx + I_x \sin kx \\
 &\xrightarrow{x} -I_z \cos kx + I_x \sin kx \\
 \xrightarrow{\text{Crush}} &-I_z \cos kx \\
 \xrightarrow{x} &-I_y \cos kx \\
 &\rightarrow -I_y \cos kx \cos kx' - I_x \cos kx \sin kx' \\
 \xrightarrow{x} &+I_z \cos kx \cos kx' - I_x \cos kx \sin kx'
 \end{aligned}$$

RF	RF1	RF2	RF3	RF4	RF5	RF6	RF7	ACQ
Tip Angle	$\frac{\pi}{2}$	NA						
1	0	0	0	0	0	0	0	0
2	0	1	1	0	0	0	0	2
3	0	2	0	0	0	0	0	2
4	0	3	1	0	0	0	0	0
5	0	0	0	0	0	1	1	2
6	0	1	1	0	0	1	1	0
7	0	.2	0	0	0	1	1	0
8	0	3	1	0	0	1	1	2
9	0	0	0	1	0	0	1	0
10	0	1	1	1	0	0	1	2
11	0	2	0	1	0	0	1	2
12	0	3	1	1	0	0	1	0
13	0	0	0	1	0	1	0	0
14	0	1	1	1	0	1	0	2
15	0	2	0	1	0	1	0	2
16	0	3	1	1	0	1	0	0

Table A.2: Improved phase Cycle for 2-D Scattering. For all experiments, $2D_{xy}$, $2D_{xx}$ and $2D_{yy}$, only one k pathway is selected. CYCLOP can be implemented on top of this phase cycling.

$$\begin{aligned}
& \xrightarrow{\text{Crush}} +I_z \cos kx \cos kx' \\
& \xrightarrow{x} +I_y \cos kx \cos kx' \\
& \longrightarrow +I_y \cos kx \cos kx' \cos kx'' + I_x \cos kx \cos kx' \sin kx'' \\
& \xrightarrow{x} -I_z \cos kx \cos kx' \cos kx'' + I_x \cos kx \cos kx' \sin kx'' \\
& \xrightarrow{\text{Crush}} -I_z \cos kx \cos kx' \cos kx'' \\
& \xrightarrow{x} -I_y \cos kx \cos kx' \cos kx'' \\
& \longrightarrow -I_y \cos kx \cos kx' \cos kx'' \cos kx''' - I_x \cos kx \cos kx' \cos kx'' \sin kx'''
\end{aligned}$$

2. ADC phase :-

$$\begin{aligned}
I_z & \xrightarrow{x} +I_y \\
& \longrightarrow +I_y \cos kx + I_x \sin kx \\
& \xrightarrow{y} +I_y \cos kx + I_z \sin kx \\
& \xrightarrow{\text{Crush}} +I_z \sin kx \\
& \xrightarrow{y} -I_x \sin kx \\
& \longrightarrow -I_x \sin kx \cos kx' + I_y \sin kx \sin kx' \\
& \xrightarrow{x} -I_x \sin kx \cos kx' - I_z \sin kx \sin kx' \\
& \xrightarrow{\text{Crush}} -I_z \sin kx \sin kx' \\
& \xrightarrow{x} -I_y \sin kx \sin kx' \\
& \longrightarrow -I_y \sin kx \sin kx' \cos kx'' - I_x \sin kx \sin kx' \sin kx'' \\
& \xrightarrow{-x} +I_z \sin kx \sin kx' \cos kx'' - I_x \sin kx \sin kx' \sin kx'' \\
& \xrightarrow{\text{Crush}} +I_z \sin kx \sin kx' \cos kx'' \\
& \xrightarrow{x} +I_y \sin kx \sin kx' \cos kx'' \\
& \longrightarrow +I_y \sin kx \sin kx' \cos kx'' \cos kx''' + I_x \sin kx \sin kx' \cos kx'' \sin kx'''
\end{aligned}$$

3. ADC phase :-

$$I_z \xrightarrow{x} +I_y$$

$$\begin{aligned}
&\rightarrow +I_y \cos kx + I_x \sin kx \\
&\stackrel{-x}{\rightarrow} +I_z \cos kx + I_x \sin kx \\
&\stackrel{\text{Crush}}{\rightarrow} +I_z \cos kx \\
&\stackrel{x}{\rightarrow} +I_y \cos kx \\
&\rightarrow +I_y \cos kx \cos kx' + I_x \cos kx \sin kx' \\
&\stackrel{x}{\rightarrow} -I_z \cos kx \cos kx' + I_x \cos kx \sin kx' \\
&\stackrel{\text{Crush}}{\rightarrow} -I_z \cos kx \cos kx' \\
&\stackrel{x}{\rightarrow} -I_y \cos kx \cos kx' \\
&\rightarrow -I_y \cos kx \cos kx' \cos kx'' - I_x \cos kx \cos kx' \sin kx'' \\
&\stackrel{x}{\rightarrow} +I_z \cos kx \cos kx' \cos kx'' - I_x \cos kx \cos kx' \sin kx'' \\
&\stackrel{\text{Crush}}{\rightarrow} +I_z \cos kx \cos kx' \cos kx'' \\
&\stackrel{x}{\rightarrow} +I_y \cos kx \cos kx' \cos kx'' \\
&\rightarrow +I_y \cos kx \cos kx' \cos kx'' \cos kx''' + I_x \cos kx \cos kx' \cos kx'' \sin kx'''
\end{aligned}$$

4. ADC phase +:

$$\begin{aligned}
I_z &\stackrel{x}{\rightarrow} +I_y \\
&\rightarrow +I_y \cos kx + I_x \sin kx \\
&\stackrel{-y}{\rightarrow} +I_y \cos kx - I_z \sin kx \\
&\stackrel{\text{Crush}}{\rightarrow} -I_z \sin kx \\
&\stackrel{y}{\rightarrow} +I_x \sin kx \\
&\rightarrow +I_x \sin kx \cos kx' - I_y \sin kx \sin kx' \\
&\stackrel{x}{\rightarrow} +I_x \sin kx \cos kx' + I_z \sin kx \sin kx' \\
&\stackrel{\text{Crush}}{\rightarrow} +I_z \sin kx \sin kx' \\
&\stackrel{x}{\rightarrow} +I_y \sin kx \sin kx' \\
&\rightarrow +I_y \sin kx \sin kx' \cos kx'' + I_x \sin kx \sin kx' \sin kx'' \\
&\stackrel{x}{\rightarrow} -I_z \sin kx \sin kx' \cos kx'' + I_x \sin kx \sin kx' \sin kx''
\end{aligned}$$

$$\begin{aligned}
& \xrightarrow{\text{Crush}} -I_z \sin kx \sin kx' \cos kx'' \\
& \xrightarrow{x} -I_y \sin kx \sin kx' \cos kx'' \\
& \rightarrow -I_y \sin kx \sin kx' \cos kx'' \cos kx''' - I_x \sin kx \sin kx' \cos kx'' \sin kx'''
\end{aligned}$$

5. ADC phase :-

$$\begin{aligned}
I_z & \xrightarrow{x} +I_y \\
& \rightarrow +I_y \cos kx + I_x \sin kx \\
& \xrightarrow{x} -I_z \cos kx + I_x \sin kx \\
& \xrightarrow{\text{Crush}} -I_z \cos kx \\
& \xrightarrow{x} -I_y \cos kx \\
& \rightarrow -I_y \cos kx \cos kx' - I_x \cos kx \sin kx' \\
& \xrightarrow{x} +I_z \cos kx \cos kx' - I_x \cos kx \sin kx' \\
& \xrightarrow{\text{Crush}} +I_z \cos kx \cos kx' \\
& \xrightarrow{x} +I_y \cos kx \cos kx' \\
& \rightarrow +I_y \cos kx \cos kx' \cos kx'' + I_x \cos kx \cos kx' \sin kx'' \\
& \xrightarrow{y} +I_y \cos kx \cos kx' \cos kx'' + I_z \cos kx \cos kx' \sin kx'' \\
& \xrightarrow{\text{Crush}} +I_z \cos kx \cos kx' \sin kx'' \\
& \xrightarrow{y} -I_x \cos kx \cos kx' \sin kx'' \\
& \rightarrow -I_x \cos kx \cos kx' \sin kx'' \cos kx''' + I_y \cos kx \cos kx' \sin kx'' \sin kx'''
\end{aligned}$$

6. ADC phase +:

$$\begin{aligned}
I_z & \xrightarrow{x} +I_y \\
& \rightarrow +I_y \cos kx + I_x \sin kx \\
& \xrightarrow{y} +I_y \cos kx + I_z \sin kx \\
& \xrightarrow{\text{Crush}} +I_z \sin kx \\
& \xrightarrow{y} -I_x \sin kx
\end{aligned}$$

$$\begin{aligned}
&\rightarrow -I_x \sin kx \cos kx' + I_y \sin kx \sin kx' \\
&\stackrel{x}{\rightarrow} -I_x \sin kx \cos kx' - I_y \sin kx \sin kx' \\
&\stackrel{\text{Crush}}{\rightarrow} -I_z \sin kx \sin kx' \\
&\stackrel{x}{\rightarrow} -I_y \sin kx \sin kx' \\
&\rightarrow -I_y \sin kx \sin kx' \cos kx'' - I_x \sin kx \sin kx' \sin kx'' \\
&\stackrel{y}{\rightarrow} -I_y \sin kx \sin kx' \cos kx'' - I_z \sin kx \sin kx' \sin kx'' \\
&\stackrel{\text{Crush}}{\rightarrow} -I_z \sin kx \sin kx' \sin kx'' \\
&\stackrel{y}{\rightarrow} +I_x \sin kx \sin kx' \sin kx'' \\
&\rightarrow +I_x \sin kx \sin kx' \sin kx'' \cos kx''' - I_y \sin kx \sin kx' \sin kx'' \sin kx'''
\end{aligned}$$

7. ADC phase +:

$$\begin{aligned}
I_z &\stackrel{x}{\rightarrow} +I_y \\
&\rightarrow +I_y \cos kx + I_x \sin kx \\
&\stackrel{-x}{\rightarrow} +I_z \cos kx + I_x \sin kx \\
&\stackrel{\text{Crush}}{\rightarrow} +I_z \cos kx \\
&\stackrel{x}{\rightarrow} +I_y \cos kx \\
&\rightarrow +I_y \cos kx \cos kx' + I_x \cos kx \sin kx' \\
&\stackrel{x}{\rightarrow} -I_z \cos kx \cos kx' + I_x \cos kx \sin kx' \\
&\stackrel{\text{Crush}}{\rightarrow} -I_z \cos kx \cos kx' \\
&\stackrel{x}{\rightarrow} -I_y \cos kx \cos kx' \\
&\rightarrow -I_y \cos kx \cos kx' \cos kx'' - I_x \cos kx \cos kx' \sin kx'' \\
&\stackrel{y}{\rightarrow} -I_y \cos kx \cos kx' \cos kx'' - I_z \cos kx \cos kx' \sin kx'' \\
&\stackrel{\text{Crush}}{\rightarrow} -I_z \cos kx \cos kx' \sin kx'' \\
&\stackrel{y}{\rightarrow} +I_x \cos kx \cos kx' \sin kx'' \\
&\rightarrow +I_x \cos kx \cos kx' \sin kx'' \cos kx''' - I_y \cos kx \cos kx' \sin kx'' \sin kx'''
\end{aligned}$$

8. ADC phase -:

$$\begin{aligned}
 I_z &\xrightarrow{x} +I_y \\
 &\longrightarrow +I_y \cos kx + I_x \sin kx \\
 &\xrightarrow{-y} +I_y \cos kx - I_z \sin kx \\
 &\xrightarrow{\text{Crush}} -I_z \sin kx \\
 &\xrightarrow{y} +I_x \sin kx \\
 &\longrightarrow +I_x \sin kx \cos kx' - I_y \sin kx \sin kx' \\
 &\xrightarrow{x} +I_x \sin kx \cos kx' + I_z \sin kx \sin kx' \\
 &\xrightarrow{\text{Crush}} +I_z \sin kx \sin kx' \\
 &\xrightarrow{x} +I_y \sin kx \sin kx' \\
 &\longrightarrow +I_y \sin kx \sin kx' \cos kx'' + I_x \sin kx \sin kx' \sin kx'' \\
 &\xrightarrow{y} +I_y \sin kx \sin kx' \cos kx'' + I_z \sin kx \sin kx' \sin kx'' \\
 &\xrightarrow{\text{Crush}} +I_z \sin kx \sin kx' \sin kx'' \\
 &\xrightarrow{y} -I_x \sin kx \sin kx' \sin kx'' \\
 &\longrightarrow -I_x \sin kx \sin kx' \sin kx'' \cos kx''' + I_y \sin kx \sin kx' \sin kx'' \sin kx'''
 \end{aligned}$$

9. ADC phase +:

$$\begin{aligned}
 I_z &\xrightarrow{x} +I_y \\
 &\longrightarrow +I_y \cos kx + I_x \sin kx \\
 &\xrightarrow{-x} -I_z \cos kx + I_x \sin kx \\
 &\xrightarrow{\text{Crush}} -I_z \cos kx \\
 &\xrightarrow{-x} -I_y \cos kx \\
 &\longrightarrow -I_y \cos kx \cos kx' - I_x \cos kx \sin kx' \\
 &\xrightarrow{-y} -I_y \cos kx \cos kx' - I_x \cos kx \sin kx' \\
 &\xrightarrow{\text{Crush}} -I_z \cos kx \sin kx'
 \end{aligned}$$

$$\begin{aligned}
& \xrightarrow{x} -I_y \cos kx \sin kx' \\
& \rightarrow -I_y \cos kx \sin kx' \cos kx'' - I_x \cos kx \sin kx' \sin kx'' \\
& \xrightarrow{x} +I_z \cos kx \sin kx' \cos kx'' - I_x \cos kx \sin kx' \sin kx'' \\
& \xrightarrow{\text{Crush}} +I_z \cos kx \sin kx' \cos kx'' \\
& \xrightarrow{y} -I_x \cos kx \sin kx' \cos kx'' \\
& \rightarrow -I_x \cos kx \sin kx' \cos kx'' \cos kx''' + I_y \cos kx \sin kx' \cos kx'' \sin kx'''
\end{aligned}$$

10. ADC phase :-

$$\begin{aligned}
I_z & \xrightarrow{x} +I_y \\
& \rightarrow +I_y \cos kx + I_x \sin kx \\
& \xrightarrow{y} +I_y \cos kx + I_z \sin kx \\
& \xrightarrow{\text{Crush}} +I_z \sin kx \\
& \xrightarrow{y} -I_x \sin kx \\
& \rightarrow -I_x \sin kx \cos kx' + I_y \sin kx \sin kx' \\
& \xrightarrow{y} -I_z \sin kx \cos kx' + I_y \sin kx \sin kx' \\
& \xrightarrow{\text{Crush}} -I_z \sin kx \cos kx' \\
& \xrightarrow{x} -I_y \sin kx \cos kx' \\
& \rightarrow -I_y \sin kx \cos kx' \cos kx'' - I_x \sin kx \cos kx' \sin kx'' \\
& \xrightarrow{x} +I_z \sin kx \cos kx' \cos kx'' - I_x \sin kx \cos kx' \sin kx'' \\
& \xrightarrow{\text{Crush}} +I_z \sin kx \cos kx' \cos kx'' \\
& \xrightarrow{y} -I_x \sin kx \cos kx' \cos kx'' \\
& \rightarrow -I_x \sin kx \cos kx' \cos kx'' \cos kx''' + I_y \sin kx \cos kx' \cos kx'' \sin kx'''
\end{aligned}$$

11. ADC phase :-

$$\begin{aligned}
I_z & \xrightarrow{x} +I_y \\
& \rightarrow +I_y \cos kx + I_x \sin kx
\end{aligned}$$

$$\begin{aligned}
& \xrightarrow{-z} +I_z \cos kx + I_x \sin kx \\
& \xrightarrow{\text{Crush}} +I_z \cos kx \\
& \xrightarrow{z} +I_y \cos kx \\
& \longrightarrow +I_y \cos kx \cos kx' + I_x \cos kx \sin kx' \\
& \xrightarrow{y} +I_y \cos kx \cos kx' + I_z \cos kx \sin kx' \\
& \xrightarrow{\text{Crush}} +I_z \cos kx \sin kx' \\
& \xrightarrow{z} +I_y \cos kx \sin kx' \\
& \longrightarrow +I_y \cos kx \sin kx' \cos kx'' + I_x \cos kx \sin kx' \sin kx'' \\
& \xrightarrow{z} -I_z \cos kx \sin kx' \cos kx'' + I_x \cos kx \sin kx' \sin kx'' \\
& \xrightarrow{\text{Crush}} -I_z \cos kx \sin kx' \cos kx'' \\
& \xrightarrow{y} +I_x \cos kx \sin kx' \cos kx'' \\
& \longrightarrow +I_x \cos kx \sin kx' \cos kx'' \cos kx''' - I_y \cos kx \sin kx' \cos kx'' \sin kx'''
\end{aligned}$$

12. ADC phase +:

$$\begin{aligned}
I_z & \xrightarrow{z} +I_y \\
& \longrightarrow +I_y \cos kx + I_x \sin kx \\
& \xrightarrow{-y} +I_y \cos kx - I_z \sin kx \\
& \xrightarrow{\text{Crush}} -I_z \sin kx \\
& \xrightarrow{y} +I_x \sin kx \\
& \longrightarrow +I_x \sin kx \cos kx' - I_y \sin kx \sin kx' \\
& \xrightarrow{y} +I_z \sin kx \cos kx' - I_x \sin kx \sin kx' \\
& \xrightarrow{\text{Crush}} +I_z \sin kx \cos kx' \\
& \xrightarrow{z} +I_y \sin kx \cos kx' \\
& \longrightarrow +I_y \sin kx \cos kx' \cos kx'' + I_x \sin kx \cos kx' \sin kx'' \\
& \xrightarrow{z} -I_z \sin kx \cos kx' \cos kx'' + I_x \sin kx \cos kx' \sin kx'' \\
& \xrightarrow{\text{Crush}} -I_z \sin kx \cos kx' \cos kx''
\end{aligned}$$

$$\begin{aligned}
 \xrightarrow{y} & +I_x \sin kx \cos kx' \cos kx'' \\
 \longrightarrow & +I_x \sin kx \cos kx' \cos kx'' \cos kx''' - I_y \sin kx \cos kx' \cos kx'' \sin kx'''
 \end{aligned}$$

13. ADC phase +:

$$\begin{aligned}
 I_z & \xrightarrow{x} +I_y \\
 & \longrightarrow +I_y \cos kx + I_x \sin kx \\
 & \xrightarrow{x} -I_z \cos kx + I_x \sin kx \\
 \xrightarrow{\text{Crush}} & -I_z \cos kx \\
 \xrightarrow{x} & -I_y \cos kx \\
 & \longrightarrow -I_y \cos kx \cos kx' - I_x \cos kx \sin kx' \\
 \xrightarrow{y} & -I_y \cos kx \cos kx' - I_x \cos kx \sin kx' \\
 \xrightarrow{\text{Crush}} & -I_z \cos kx \sin kx' \\
 \xrightarrow{x} & -I_y \cos kx \sin kx' \\
 & \longrightarrow -I_y \cos kx \sin kx' \cos kx'' - I_x \cos kx \sin kx' \sin kx'' \\
 \xrightarrow{y} & -I_y \cos kx \sin kx' \cos kx'' - I_z \cos kx \sin kx' \sin kx'' \\
 \xrightarrow{\text{Crush}} & -I_z \cos kx \sin kx' \sin kx'' \\
 \xrightarrow{x} & -I_y \cos kx \sin kx' \sin kx'' \\
 & \longrightarrow -I_y \cos kx \sin kx' \sin kx'' \cos kx''' - I_x \cos kx \sin kx' \sin kx'' \sin kx'''
 \end{aligned}$$

14. ADC phase -:

$$\begin{aligned}
 I_z & \xrightarrow{x} +I_y \\
 & \longrightarrow +I_y \cos kx + I_x \sin kx \\
 \xrightarrow{y} & +I_y \cos kx + I_z \sin kx \\
 \xrightarrow{\text{Crush}} & +I_z \sin kx \\
 \xrightarrow{y} & -I_x \sin kx \\
 & \longrightarrow -I_x \sin kx \cos kx' + I_y \sin kx \sin kx'
 \end{aligned}$$

$$\begin{aligned}
& \xrightarrow{y} -I_z \sin kx \cos kx' + I_y \sin kx \sin kx' \\
& \xrightarrow{\text{Crush}} -I_z \sin kx \cos kx' \\
& \xrightarrow{x} -I_y \sin kx \cos kx' \\
& \longrightarrow -I_y \sin kx \cos kx' \cos kx'' - I_x \sin kx \cos kx' \sin kx'' \\
& \xrightarrow{y} -I_y \sin kx \cos kx' \cos kx'' - I_z \sin kx \cos kx' \sin kx'' \\
& \xrightarrow{\text{Crush}} -I_z \sin kx \cos kx' \sin kx'' \\
& \xrightarrow{x} -I_y \sin kx \cos kx' \sin kx'' \\
& \longrightarrow -I_y \sin kx \cos kx' \sin kx'' \cos kx''' - I_x \sin kx \cos kx' \sin kx'' \sin kx'''
\end{aligned}$$

15. ADC phase :-

$$\begin{aligned}
I_z & \xrightarrow{x} +I_y \\
& \longrightarrow +I_y \cos kx + I_x \sin kx \\
& \xrightarrow{-x} +I_z \cos kx + I_x \sin kx \\
& \xrightarrow{\text{Crush}} +I_z \cos kx \\
& \xrightarrow{x} +I_y \cos kx \\
& \longrightarrow +I_y \cos kx \cos kx' + I_x \cos kx \sin kx' \\
& \xrightarrow{y} +I_y \cos kx \cos kx' + I_z \cos kx \sin kx' \\
& \xrightarrow{\text{Crush}} +I_z \cos kx \sin kx' \\
& \xrightarrow{x} +I_y \cos kx \sin kx' \\
& \longrightarrow +I_y \cos kx \sin kx' \cos kx'' + I_x \cos kx \sin kx' \sin kx'' \\
& \xrightarrow{y} +I_y \cos kx \sin kx' \cos kx'' + I_z \cos kx \sin kx' \sin kx'' \\
& \xrightarrow{\text{Crush}} +I_z \cos kx \sin kx' \sin kx'' \\
& \xrightarrow{x} +I_y \cos kx \sin kx' \sin kx'' \\
& \longrightarrow +I_y \cos kx \sin kx' \sin kx'' \cos kx''' + I_x \cos kx \sin kx' \sin kx'' \sin kx'''
\end{aligned}$$

16. ADC phase +:

$$\begin{aligned}
 I_z &\xrightarrow{x} +I_y \\
 &\rightarrow +I_y \cos kx + I_x \sin kx \\
 &\xrightarrow{-y} +I_y \cos kx - I_z \sin kx \\
 &\xrightarrow{\text{Crush}} -I_z \sin kx \\
 &\xrightarrow{y} +I_x \sin kx \\
 &\rightarrow +I_x \sin kx \cos kx' - I_y \sin kx \sin kx' \\
 &\xrightarrow{v} +I_z \sin kx \cos kx' - I_x \sin kx \sin kx' \\
 &\xrightarrow{\text{Crush}} +I_z \sin kx \cos kx' \\
 &\xrightarrow{x} +I_y \sin kx \cos kx' \\
 &\rightarrow +I_y \sin kx \cos kx' \cos kx'' + I_x \sin kx \cos kx' \sin kx'' \\
 &\xrightarrow{y} +I_y \sin kx \cos kx' \cos kx'' + I_z \sin kx \cos kx' \sin kx'' \\
 &\xrightarrow{\text{Crush}} +I_z \sin kx \cos kx' \sin kx'' \\
 &\xrightarrow{x} +I_y \sin kx \cos kx' \sin kx'' \\
 &\rightarrow +I_y \sin kx \cos kx' \sin kx'' \cos kx''' + I_x \sin kx \cos kx' \sin kx'' \sin kx'''
 \end{aligned}$$

The total sum of the signal from all 16 scans is,

$$\begin{aligned}
 E = & -I_y \cos kx \cos kx' \cos kx'' \cos kx''' - I_x \cos kx \cos kx' \cos kx'' \sin kx''' \\
 & -I_y \sin kx \sin kx' \cos kx'' \cos kx''' - I_x \sin kx \sin kx' \cos kx'' \sin kx''' \\
 & -I_y \cos kx \cos kx' \cos kx'' \cos kx''' - I_x \cos kx \cos kx' \cos kx'' \sin kx''' \\
 & -I_y \sin kx \sin kx' \cos kx'' \cos kx''' - I_x \sin kx \sin kx' \cos kx'' \sin kx''' \\
 & +I_x \cos kx \cos kx' \sin kx'' \cos kx''' - I_y \cos kx \cos kx' \sin kx'' \sin kx''' \\
 & +I_x \sin kx \sin kx' \sin kx'' \cos kx''' - I_y \sin kx \sin kx' \sin kx'' \sin kx''' \\
 & +I_x \cos kx \cos kx' \sin kx'' \cos kx''' - I_y \cos kx \cos kx' \sin kx'' \sin kx''' \\
 & +I_x \sin kx \sin kx' \sin kx'' \cos kx''' - I_y \sin kx \sin kx' \sin kx'' \sin kx'''
 \end{aligned}$$

$$\begin{aligned}
& -I_x \cos kx \sin kx' \cos kx'' \cos kx''' + I_y \cos kx \sin kx' \cos kx'' \sin kx''' \\
& + I_x \sin kx \cos kx' \cos kx'' \cos kx''' - I_y \sin kx \cos kx' \cos kx'' \sin kx''' \\
& - I_x \cos kx \sin kx' \cos kx'' \cos kx''' + I_y \cos kx \sin kx' \cos kx'' \sin kx''' \\
& + I_x \sin kx \cos kx' \cos kx'' \cos kx''' - I_y \sin kx \cos kx' \cos kx'' \sin kx''' \\
& - I_y \cos kx \sin kx' \sin kx'' \cos kx''' - I_x \cos kx \sin kx' \sin kx'' \sin kx''' \\
& + I_y \sin kx \cos kx' \sin kx'' \cos kx''' + I_x \sin kx \cos kx' \sin kx'' \sin kx''' \\
& - I_y \cos kx \sin kx' \sin kx'' \cos kx''' - I_x \cos kx \sin kx' \sin kx'' \sin kx''' \\
& + I_y \sin kx \cos kx' \sin kx'' \cos kx''' + I_x \sin kx \cos kx' \sin kx'' \sin kx''' \\
= & -2I_y \cos k(x - x') \cos k(x'' - x''') + 2I_x \cos k(x - x') \sin k(x'' - x''') \\
& + 2I_y \sin k(x - x') \sin k(x'' - x''') + 2I_x \sin k(x - x') \cos k(x'' - x''') \\
= & -2I_y \cos [k(x - x' + x'' - x''')] \\
& + 2I_x \sin [k(x - x' + x'' - x''')] \\
= & -2e^{-ik(x-x'+x''-x'''})
\end{aligned}$$

It can be seen that only one k path is selected.

The middle period no zero k path can also be erased by setting the second pair of gradient pulses opposite to the first pair. With this scheme, the middle path is killed by the background gradient. See Figure(A-2).

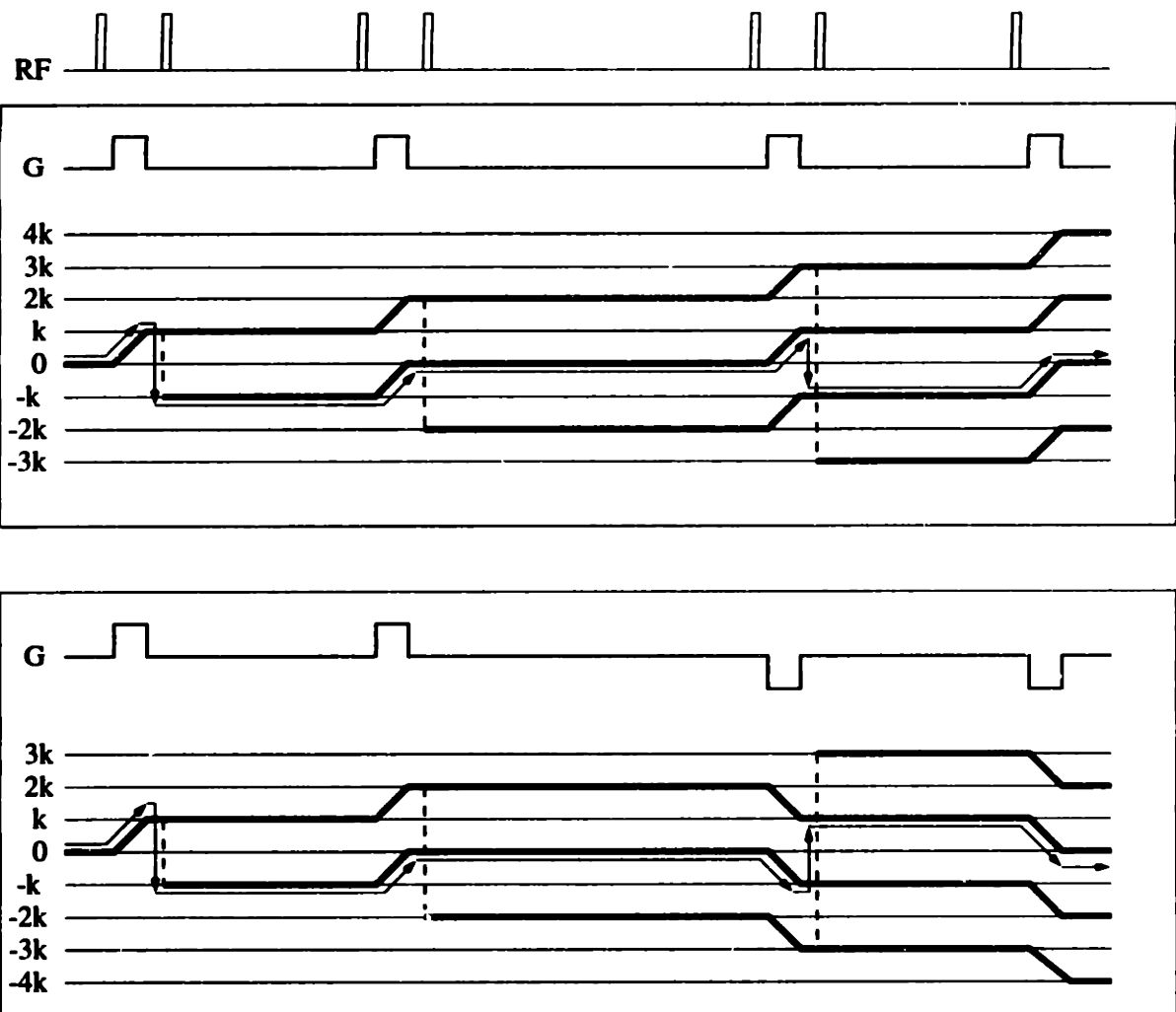


Figure A-2: The middle non-zero k path can be killed by setting the two pairs of the gradient pulses opposite to each other. The unwanted path is erased by the mismatch of the first and the second pair of gradient pulses due to background gradient.

Appendix B

Computer Program Codes

B.1 C++ Code for Monte-Carlo Simulation for 2-D Scattering

```
#include <stdio.h>
#include <iostream.h>
#include <string.h>
#include <math.h>
#include <stdlib.h>
#include <time.h>
#include <complex.h>

int i, j, k, l, m, n;
FILE *fid;
char outfile[128];
double_complex sxx[65], sxy[65];
double r1, theta1, sint1, cost1, phi1, sinp1, cosp1;
double r2, theta2, sint2, cost2, phi2, sinp2, cosp2;
double r3, theta3, sint3, cost3, phi3, sinp3, cosp3;
```

10

```

double r4, theta4, sint4, cost4, phi4, sinp4, cosp4;
double theta5, sint5, cost5, phi5, sinp5, cosp5;
double theta6, sint6, cost6, phi6, sinp6, cosp6;
double ctant6, test;
double ratio, qmax, d_q;
double x1, x2, x3, x4, x5, x6; 20
double yy1, y2, y3, y4, y5, y6;;
double z1, z2, z3, z4, z5, z6;
double dx1, dx2, dx3, dx4, dy3, dy4;
double_complex phase1, phase2, phase3;
double PI=3.14159265;
double_complex I(0,1);
main()
{
    time_t t; 30
    srand((unsigned) time(&t));
    cout << "Monte-Carlo simulation of 2Dxx and 2Dxy Experiment.\n";
    cout << "Radius of rotating ellipes is set to 1 micron.\n";
    cout << "Input the other radius of the ellipes: ";
    cin >> ratio;
    cout << "Input the value of the highest q: ";
    cin >> qmax;
    cout << "Name of the file to be saved: ";
    cin >> outfile;
    cout << "Number of 1000 cycles: "; 40
    cin >> n;

    d_q=qmax/63.0;
    for(k=1; k<=n; k++){
        cout << k << "\n";

```

```

for(j=1; j<=1000; j++){

    r1=(rand() % 100)/100.0;
    r2=(rand() % 100)/100.0;
    r3=(rand() % 100)/100.0;
    r4=(rand() % 100)/100.0; 50

    r1=pow(r1,1./3.);
    r2=pow(r2,1./3.);
    r3=pow(r3,1./3.);
    r4=pow(r4,1./3.);

    theta1=(rand() % 100)/100.0 * PI;
    theta2=(rand() % 100)/100.0 * PI;
    theta3=(rand() % 100)/100.0 * PI;
    theta4=(rand() % 100)/100.0 * PI;
    theta5=(rand() % 100)/100.0 * PI; 60

    phi1=(rand() % 100)/100.0 * 2 * PI;
    phi2=(rand() % 100)/100.0 * 2 * PI;
    phi3=(rand() % 100)/100.0 * 2 * PI;
    phi4=(rand() % 100)/100.0 * 2 * PI;
    phi5=(rand() % 100)/100.0 * 2 * PI;

    r1=pow(r1,1./3.); 70
    r2=pow(r2,1./3.);
    r3=pow(r3,1./3.);
    r4=pow(r4,1./3.);

    sint1=sin(theta1);

```

```
sint2=sin(theta2);
sint3=sin(theta3);
sint4=sin(theta4);
sint5=sin(theta5);
```

80

```
cost1=cos(theta1);
cost2=cos(theta2);
cost3=cos(theta3);
cost4=cos(theta4);
cost5=cos(theta5);
```

```
sinp1=sin(phi1);
sinp2=sin(phi2);
sinp3=sin(phi3);
sinp4=sin(phi4);
sinp5=sin(phi5);
```

90

```
cosp1=cos(phi1);
cosp2=cos(phi2);
cosp3=cos(phi3);
cosp4=cos(phi4);
cosp5=cos(phi5);
```

```
if(cost5==0){
    test=((rand() % 2)-0.5)*2;
    sinp6=test*cosp5;
    cosp6=-test*sinp5;
    sint6=(rand() % 100)/100.0;
    cost6=((rand() % 2)-0.5)*2*sqrt(1.0-sint6*sint6);
}
```

100

```

else {
    phi6=(rand() % 100)/100.0 * 2 * PI;
    sinp6=sin(phi6);
    cosp6=cos(phi6);
    if(abs(cost5)==1){110
        sint6=1;
        cost6=0;
    }
    else {
        ctant6=-sint5/cost5*cos(phi5-phi6);
        sint6=1.0/sqrt(ctant6*ctant6+1.0);
        cost6=ctant6*sint6;
    }
}

120
z1=ratio*r1*cost1;
z2=ratio*r2*cost2;
z3=ratio*r3*cost3;
z4=ratio*r4*cost4;
z5=cost5;
z6=cost6;

x1=r1*sint1*cosp1;
x2=r2*sint2*cosp2;
x3=r3*sint3*cosp3;130
x4=r4*sint4*cosp4;
x5=sint5*cosp5;
x6=sint6*cosp6;

yy1=r1*sint1*sinp1;

```

```
y2=r2*sint2*sinp2;  
y3=r3*sint3*sinp3;  
y4=r4*sint4*sinp4;  
y5=sint5*sinp5;  
y6=sint6*sinp6;
```

140

```
dx1=x1*x5+yy1*y5+z1*z5;  
dx2=x2*x5+y2*y5+z2*z5;
```

```
dx3=x3*x5+y3*y5+z3*z5;  
dx4=x4*x5+y4*y5+z4*z5;
```

```
dy3=x3*x6+y3*y6+z3*z6;  
dy4=x4*x6+y4*y6+z4*z6;
```

150

```
for(i=1; i<=64; i++){
```

```
phase1=exp(I*2*PI*d_q*(i-1)*(dx1-dx2));  
phase2=exp(I*2*PI*d_q*(i-1)*(dx3-dx4));  
phase3=exp(I*2*PI*d_q*(i-1)*(dy3-dy4));
```

```
sxx[i]=sxx[i]+sint1*sint2*sint3*sint4*sint5*phase1*phase2;
```

```
sxy[i]=sxy[i]+sint1*sint2*sint3*sint4*sint5*phase1*phase3;
```

```
}
```

```
}
```

```
}
```

```
fid=fopen(outfile,"w");
```

```
for(i=1; i <= 64; i++)
```

```
{
```

```
fprintf(fid, "%f\t%f\t%f\n", (i-1)*d_q, abs(sxx[i]), abs(sxy[i]));
```

160

```
    }  
fclose(fid);  
}
```

B.2 MATLAB Code for Convolution Calculation for 2-D Scattering

```
x=-20:0.1:20;  
y=x;  
a=(20/bdiva)^(1/3)  
b=bdiva*a  
SS=zeros(1,401);  
SS=conv(SS,SS);  
SS1=SS;  
SS=conv(SS,SS);  
SS2=SS;  
[X Y]=meshgrid(x,y);  
for theta=0:pi/90:pi/2,  
    theta  
    ct=cos(theta);  
    st=sin(theta);  
    for phi=0:pi/90:pi/4,  
        cp=cos(phi);  
        sp=sin(phi);  
        b2=4*st^2*ct^2*(1/a^2-1/b^2)^2*(cp*Y-sp*X).^2;  
        aa=(st^2/a^2+ct^2/b^2);  
        SS=conv(SS,(aa/b2)*b2*(ct*cp*Y-st*sp*X));  
    end  
end  
SS=SS./((pi/2)^2);  
surf(X,Y,SS);  
title('2-D Convolution Scattering');
```

10

```

cx2=((cp^2+ct^2*sp^2)/a^2 +st^2*sp^2/b^2)*X.^2;
cy2=((sp^2+ct^2*cp^2)/a^2 +st^2*cp^2/b^2)*Y.^2;
xy=2*st^2*sp*cp*(1/a^2-1/b^2)*X.*Y;
ac4=4*aa*(cx2+cy2+xy-1);
Z=real(sqrt(b2-ac4))/aa;
Z1=Z';
x1=sum(Z);
y1=sum(Z1);
SS=SS+st*conv(conv(x1,x1),conv( Vy1,y1));
SS1=SS1+st*(conv(x1,x1)+conv(y1, y1));
SS2=SS2+st*conv(conv(x1,x1),conv (x1,x1));
SS2=SS2+st*conv(conv(y1,y1),conv(y1,y1) );
end
end
SS=SS/sum(SS);
SS2=SS2/sum(SS2);
SS1=conv(SS1,SS1);
SS1=SS1/sum(SS1);

```

20

30

B.3 Matlab Code for Calculation Analytically

B.3.1 2-D Scattering with Parallel Scattering Vectors

```

NN=50;
qmax=0.5;

```

```

q=qmax/NN;qmax/NN;qmax;
Sxx=zeros(1,NN);
for j=1:100,
    theta=pi/100*j;
    c=sqrt(a^2*(sin(theta))^2+b^2*(cos(theta))^2);
    Sxx=Sxx+(sin(c*q)-c*q.*cos(c*q)).^4./(c*q).^12*sin(theta);
end

```

B.3.2 2-D Scattering with Perpendicular Scattering Vectors

```

NN=50;
qmax=0.5;
q=qmax/NN;qmax/NN;qmax;
Sxy=zeros(1,NN);
for j=1:100,
    theta=pi/100*j;
    c1=sqrt(a^2*(sin(theta))^2+b^2*(cos(theta))^2);
    for k=1:200,
        phi=pi/100*k;
        c2=sqrt(a^2+(b^2-a^2)*(sin theta))^2*(cos(phi)^2));
        sx=(sin(c1*q)-c1*q.*cos(c1*q).^2./(c1*q).^6;
        sy=(sin(c2*q)-c2*q.*cos(c2*q).^2./(c2*q).^6;
        Sxy=Sxy+sx.*sy*sin(theta);
    end
end

```

Bibliography

- [1] E. M. Purcell, H. C. Torrey, and R. V. Pound. Resonance absorption by nuclear magnetic moments in a solid. *Physical Review*, 69:37, 1946.
- [2] Bloembergen, Purcell, and Pound. Relaxation effects in nuclear magnetic resonance absorption. *Physical Review*, 1948.
- [3] E. L. Hahn. Spin echoes. *Physical Review*, 80:580–594, 1950.
- [4] H. Y. Carr and E. M. Purcell. Effects of diffusion on free precession in nuclear magnetic resonance experiments. *Physical Review*, 94:630–638, 1954.
- [5] H. C. Torrey. Bloch equations with diffusion terms. *Physical Review*, 104(3):563–565, 1956.
- [6] E. O. Stejskal and J. E. Tanner. Spin diffusion measurements: Spin echoes in the presence of a time-dependent field gradient. *Journal of Chemical Physics*, 42(1):288–292, 1965.
- [7] E. O. Stejskal. Use of spin echoes in a pulsed magnetic-field gradient to study anisotropic, restricted diffusion and flow. *Journal of Chemical Physics*, 43(10):3597–3603, 1965.
- [8] J. E. Tanner. Use of the stimulated echo in NMR diffusion studies. *Journal of Chemical Physics*, 52(5), 1970.
- [9] P. Mansfield and P. K. Grannell. NMR ‘diffraction’ in solids? *Journal of Physics C: Solid State Physics*, 6:L422–L426, 1973.

- [10] P. Mansfield and P. K. Grannell. "Diffraction" and microscopy in solids and liquids by NMR. *Physical Review B*, 12(9):3618–3634, 1975.
- [11] D. G. Cory and A. N. Garroway. Measurement of translational displacement probabilities by NMR: An indicator of compartmentation. *Magnetic Resonance in Medicine*, 14:435–444, 1990.
- [12] N. F. Fatkullin. Theory of stimulated spin echo in polymer systems. "Soviet Physics JETP", 72(3):563–569, 1991.
- [13] P. T. Callaghan, A. Coy, D. MacGowan, K. J. Packer, and F. O. Zelaya. Diffraction-like effects in NMR diffusion studies of fluids in porous solids. *Nature*, 351(6):467–469, June 1991.
- [14] Paul T. Callaghan. *Principles of Nuclear Magnetic Resonance Microscopy*. Clarendon Press, 1991.
- [15] Gerald Fleischer and Franz Fujara. NMR as a generalized icoherent scattering experiment. *NMR Basic Principles and Progress*, 30:159–207, 1994.
- [16] P. T. Callaghan, K. W. Jolley, and J. Lelievre. *Biophysics Journal*, 28:133, 1979.
- [17] P. T. Callaghan and O. Soderman. *Journal of Physics C: Solid State Physics*, 87:1737, 1983.
- [18] A. Abragam. *Principles of Nuclear Magnetism*. Oxford Science Publications, 1989.
- [19] C. P. Slichter. *Principles of Magnetic Resonance*. Springer-Verlag, 1992.
- [20] F. Bloch. Nuclear induction. *Physical Review*, 70:460–474, 1946.
- [21] L. Van Hove. Correlations in space and time and born approximation scattering in systems of interacting particles. *Physical Review*, 95:245–262, 1954.
- [22] Paul T. Callaghan, Lucy C. Forde, and Craig J. Rose. Correlated susceptibility and diffusion effects in NMR microscopy using both phase-frequency encoding

and phase-phase encoding. *Journal of Magnetic Resonance, Series B*, 104:34–53, 1994.

- [23] Paul T. Callaghan and Andrew Coy. Evidence for reptational motion and the entanglement tube in semidilute polymer solutions. *Physical Review Letters*, 68(21):3176–3179, 1992.
- [24] R. M. Cotts, N. J. R. Hoch, T. Sun, and J. t. Markert. Pulsed field gradient stimulated echo methods for improved NMR diffusion measurements in heterogeneous systems. *Journal of Magnetic Resonance*, 83:252–266, 1989.
- [25] J. D. Trudeau, W. Thomas Dixon, and J. Hawkins. The effect of inhomogeneous sample susceptibility on measured diffusion anisotropy using nmr imaging. *Journal of Magnetic Resonance, Series B*, 108:22–30, 1995.
- [26] Pierre Le Doussal and Pabitra N. Sen. Decay of nuclear magnetization by diffusion in a parabolic magnetic field: An exactly solvable model. *Physical Review B*, 46(6):3465–3485, August 1992.
- [27] Lawrence L. Latour, Limin Li, and Christopher H. Sotak. Improved PFG stimulated-echo method for the measurement of diffusion in inhomogeneous fields. *Journal of Magnetic Resonance, Series B*, 101:72–77, 1993.
- [28] Lee Griffiths and Rob Horton. NMR diffusion measurements using refocused three-pulse stimulated echoes. *Journal of Magnetic Resonance*, 90:254–263, 1990.
- [29] D. Canet, B. Diter, A. Belmajdoub, and J. Brondeau. Self-diffusion measurements using a radiofrequency field gradient. *Journal of Magnetic Resonance*, 81:1–12, 1989.
- [30] George H. Vineyard. Scattering of slow neutrons by a liquid. *Physical Review*, 110(5):999–1010, June 1958.
- [31] A. D. Sodickson. PhD thesis, Massachusetts Institute of Technology, 1997.

- [32] A. L. Patterson. A fourier series method for the determination of the components of interatomic distances in crystals. *Physical Review*, 46:372–376, 1934.
- [33] Philip W. Kuchel, Andrew Coy, and Peter Stilbs. NMR “diffusion-diffraction” of water revealing alignment of erythrocytes in a magnetic field and their dimensions and membrane transport characteristics. *Magnetic Resonance in Medicine*, 37:637–643, 1997.
- [34] P. T. Callaghan. PGSE-MASSEY, a sequence for overcoming phase instability in very-high-gradient spin-echo NMR. *Journal of Magnetic Resonance*, 88:493–500, 1990.
- [35] P. T. Callaghan. Pulsed-gradient spin-echo NMR for planar, cylindrical, and spherical pores under conditions of wall relaxation. *Journal of Magnetic Resonance, Series A*, 113:53–59, 1995.
- [36] I. Chang, F. Fujara, B. Geil, G. Heuberger, T. Mangel, and H. Sillescu. Translational and rotational molecular motion in supercooled liquids studied by NMR and forced Rayleigh scattering. *"Journal of Non-Crystalline Solids"*, 172-174:248–255, 1994.
- [37] P. P. Mitra. Diffusion in porous materials as probed by pulsed gradient NMR measurements. *"Physica A"*, 241:122–127, 1997.
- [38] P. P. Mitra, L. L. Latour, R. L. Kleinberg, and C. H. Sotak. Pulsed-field-gradient NMR measurements of restricted diffusion and the return-to-the-origin probability. *Journal of Magnetic Resonance, Series A*, 114:47–58, 1995.
- [39] Limin Li and Christopher H. Sotak. Diffusion measurements by pulsed field-gradient multiple spin echoes. *Journal of Magnetic Resonance*, 92:411–420, 1991.
- [40] J. E. M. Snaar and H. Van As. NMR self-diffusion measurement in a bounded system with loss of magnetization at the walls. *Journal of Magnetic Resonance, Series A*, 102:318–326, 1993.

- [41] M. D. Hürlimann, K. G. Helmer, T. M. de Swiet, P. N. Sen, and C. S. Sotak. Spin echoes in a constant gradient and in the presence of simple restriction. Technical Report ISD-006-94-58, Schlumberger-Doll Research, Ridgefield, CT 06877-4108, October 1994.
- [42] Karl G. Helmer, Martin D. Hürlimann, Thomas M. de Swiet, Pabitra N. Sen, and C. H. Sotak. Determination of surface-area to volume ratio from restricted diffusion in a constant field gradient. Technical Report ISD-006-94-63, Schlumberger-Doll Research, Ridgefield, CT 06877-4108, October 1994.
- [43] Limin Li and Christopher H. Sotak. Self-diffusion measurements by pulsed-gradient multiple- spin-echo imaging. *Journal of Magnetic Resonance, Series B*, 101:8–16, 1993.
- [44] Partha P. Mitra and Pabitra N. Sen. Effects of microgeometry and surface relaxation on NMR pulsed-field-gradient experiments: Simple pore geometries. *Physical Review B*, 45(1):143–156, 1992.
- [45] Partha P. Mitra and Pabitra N. Sen. Effects of surface relaxation on nmr pulsed field gradient experiments in porous media. *Physica A*, 186:109–114, 1992.
- [46] Partha P. Mitra. Multiple wavevector extensions of the pulsed field gradient spin echo measurement. personal communication, July 1994.
- [47] P. P. Mitra and B. I. Halperin. Effects of finite gradient-pulse widths in pulsed-field-gradient diffusion measurements. *Journal of Magnetic Resonance, Series A*, 113:94–101, 1995.
- [48] R. Michael Boener and W. Stephen Woodward. A computer-controlled bipolar magnetic-field gradient driver for NMR electrophoretic and self-diffusion measurements. *Journal of Magnetic Resonance, Series A*, 106:195–202, 1994.
- [49] Mirko I. Hrovat and Charles G. Wade. NMR pulsed-gradient diffusion measurements. i. spin-echo stability and gradient calibration. *Journal of Magnetic Resonance*, 44:62–75, 1981.

- [50] Mirko I. Hrovat and Charles G. Wade. NMR pulsed-gradient diffusion measurements. II. residual gradients and lineshape distortions. *Journal of Magnetic Resonance*, 45:67–80, 1981.
- [51] Partha P. Mitra, Pabitra N. Sen, Lawrence M. Schwartz, and Pierre Le Doussal. Diffusion propagator as a probe of the structure of porous media. *Physical Review Letters*, 68(24):3555–3558, 1992.
- [52] W. Brian Hyslop and Paul C. Lauterbur. Effects of restricted diffusion on microscopic NMR imaging. *Journal of Magnetic Resonance*, 94:501–510, 1991.
- [53] A. Caprihan, L. Z. Wang, and E. A. Fukushima. A multiple-narrow-pulse approximation for restricted diffusion in a time-varying field gradient. *Journal of Magnetic Resonance, Series A*, 118:94–102, 1996.
- [54] Paul T. Callaghan, Andrew Coy, Lucy C. Forde, and Craig J. Rofe. Diffusive relaxation and edge enhancement in NMR microscopy. *Journal of Magnetic Resonance, Series A*, 101:347–350, 1993.
- [55] P. T. Callaghan and Sarah L. Codd. Generalized calculation of nmr imaging edge effects arising from restricted diffusion in porous media. *Draft*, 1998.
- [56] P. T. Callaghan. A simple matrix formalism for spin echo analysis of restricted diffusion under generalised gradient waveforms. *Journal of Magnetic Resonance*, 129:74–84, 1997.